JOHANNES KEPLER
UNIVERSITY LINZ

Author
Markus Ebner, BSc

Submission
Institute of Physical Chemistry and Linz Institute of Organic Solar Cells

Thesis Supervisor
a. Univ. Prof. Dr. Markus Scharber

Co-Supervisor
DI[in] Katarina Gugujonović

July 2024

DEVELOPMENT AND INTEGRATION OF INTERCONNECTING LAYERS IN PEROVSKITE ORGANIC TANDEM SOLAR CELLS

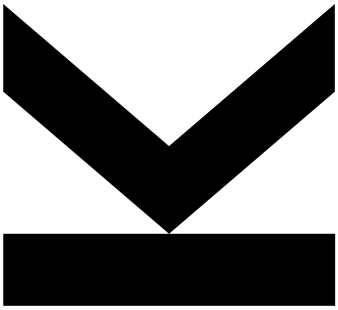

Master's Thesis

to confer the academic degree of

Diplom-Ingenieur

in the Master's Program

Chemistry and Chemical Technology

JOHANNES KEPLER UNIVERSITY LINZ
Altenberger Straße 69
4040 Linz, Austria
jku.at

SWORN DECLARATION

I hereby declare that the thesis submitted is my own unaided work, that I have not used other than the sources indicated, and that all direct and indirect sources are acknowledged as references.

Linz, 05.07.2024

Acknowledgment

First and foremost, I would like to express my deepest appreciation to a. Univ. Prof. DI Dr. Markus Scharber for his guidance during this master's thesis. I appreciate you sharing your extensive knowledge and experience with me, and for consistently providing constructive feedback. This work would not have been possible without my co-supervisor and mentor, DI^{in} Katarina Gugujonović. Thank you for your unwavering support, your guidance, and your invaluable feedback. I would also like to thank o. Univ.-Prof. Mag. Dr. DDr. h.c. Niyazi for giving me the opportunity to write my master's thesis at his institute.

Special thanks go to Christoph Putz, who instructed me how to work with different techniques and instruments and always provided valuable tips. I am also grateful to Rene Zahrhuber for conducting PL-measurements with me and allowing me to use his setup. Additionally, I had great pleasure of working with MSc Stefano Favero Costa, whose numerous discussions and enjoyable conversations made my time in the lab truly memorable. I extent my thanks to DI Elisabeth Leeb and DI Felix Mayr for their support during experiments and for sharing their expertise with me.

Thank you to my colleagues in the large office. The well-stocked candy drawer and enjoyable conversations made the time truly unforgettable. I also want to extend my appreciation to the entire LIOS team, who created an excellent working environment characterized by support and open ears. It was a pleasure to be a part of your team.

A heartfelt thank you goes to my girlfriend, who consistently encouraged and motivated me, and provided a shoulder to lean on.

Finally, I would like to thank my family and friends, who have always motivated me and accepted me as I am.

Without all of you, I would not be where I am today.

Abstract

Perovskite organic tandem solar cells can offer significant advancements compared to traditional solar cells, combining lightweight and flexible properties with high efficiency and cost-effective roll-to-roll production. Nevertheless, the technology is still in the research phase, and several issues must be resolved to harness its full potential. In this thesis, a wide band gap (E_g = 1.85 eV) perovskite solar cell with a mixed halide content is combined with a narrow band gap (E_g = 1.36 eV) organic solar cell using the donor-acceptor system PTB7-Th:IEICO-4F. A low open circuit voltage deficit (0.62 V) is achieved in the perovskite subcell by the addition of methylammonium chloride and a post-treatment with phenethylammonium iodide. Time-dependent photoluminescence and open circuit voltage measurements provided insights into light-induced phase segregation commonly observed in this type of perovskite. Additionally, the temperature and solvent stability of the perovskite cells was tested to determine the limits of the coating process for the organic subcell. For the organic subcell the water-free PEDOT variant, Solar 3, was tested as an alternative to Al4083. A post-treatment of Solar 3 with the surfactant TritonX-100 in isopropanol thereby enhanced the efficiency of the PTB7-Th:IEICO-4F organic sub cell. Both subcells were individually characterized by atomic force microscopy, UV-Vis, and photoluminescence spectroscopy as well as external quantum efficiency measurements. Different configurations of the interconnecting layer of the tandem devices were investigated and integrated into complete devices. This included variations in the thickness of a silver recombination layer and the incorporation of a MoO_x hole transport layer. The best-performing devices, utilizing the interconnecting layer PCBM/BCP/Ag/MoO_x, achieved a high open circuit voltage of up to 1.86 V, with a very low loss of 0.06 V compared to the sum of the single devices.

Kurzfassung

Perowskit organische Tandem-Solarzellen können bedeutende Vorteile im Vergleich zu herkömmlichen Solarzellen bieten, indem sie leichte und flexible Eigenschaften mit hoher Effizienz und kostengünstiger Roll-to-Roll-Produktion kombinieren. Dennoch befindet sich die Technologie noch in der Forschungsphase, und mehrere Probleme müssen gelöst werden, um ihr volles Potenzial ausschöpfen zu können. In dieser Arbeit wird eine Perowskit-Solarzelle mit großer Bandlücke (E_g = 1,85 eV) mit einer organischen Solarzelle mit geringer Bandlücke (E_g = 1,36 eV) unter Verwendung des Donor-Akzeptor-Systems PTB7-Th:IEICO-4F kombiniert. Ein geringes Defizit der Leerlaufspannung (0,62 V) wird in der Perowskit-Subzelle durch die Zugabe von Methylammoniumchlorid und eine Nachbehandlung mit Phenethylammoniumiodid erreicht. Zeitabhängige Photolumineszenz- und Leerlaufspannungsmessungen lieferten Erkenntnisse über die licht-induzierte Phasensegregation, die häufig bei dieser Art von Perowskit beobachtet wird. Zusätzlich wurde die Temperatur- und Lösungsmittelstabilität der Perowskit-Zellen getestet, um die Grenzen des Beschichtungsprozesses der organischen Subzelle zu bestimmen. Für die organische Subzelle wurde die wasserfreie PEDOT-Variante, Solar 3 als alternative zu Al4083 getestet. Eine Nachbehandlung von Solar 3 mit dem Tensid TritonX-100 in Isopropanol verbesserte dabei die Effizienz der organischen PTB7-Th:IEICO-4F Solarzellen. Beide Subzellen wurden mittels Rasterkraftmikroskopie, UV-Vis- und Photolumineszenz-Spektroskopie sowie Quanteneffizienzmessungen charakterisiert. Verschiedene Konfigurationen der Zwischenschicht der einzelnen Subzellen wurden untersucht und in vollständige Zellen integriert. Dabei wurde auch die Dicke einer Silber Rekombinationsschicht variiert und eine MoO_x-Lochtransportschicht eingesetzt. Die besten Zellen, mit der verbindenden Schicht PCBM/BCP/Ag/MoOx, erzielten eine hohe Leerlaufspannung von bis zu 1,86 V, mit einem minimalen Verlust von 0.06 V im Vergleich zur Summe der Einzelzellen.

Contents

1. Introduction

Currently, over 95 % of global annual photovoltaic production consists of crystalline silicon solar cells with an average efficiency of 20.9 %[1]. With laboratory records achieving a remarkable 27.6 %[2] efficiency, the theoretical threshold of around 29.4 %[3] nears realization. However, the production of high-purity silicon proves to be both energy-intensive and complex[4]. Despite a notable reduction in silicon consumption from 16 g W_p^{-1} to 2 g W_p^{-1} between 2004 to 2021, reducing the silicon layer further encounters limitations[1,5]. Consequently, considerable efforts have been directed toward the development of novel technologies aimed at enhancing cell efficiencies, simplifying fabrication processes, and reducing energy demands. Solution-processed thin film solar cells present a promising way, offering cost-effective production and scalability compared to their traditional silicon counterparts[6–9]. Two rapidly evolving fields, organic solar cells (OSC) and perovskite solar cells (PSC), exhibit solution processability, band gap tunability, and flexibility[10,11]. The integration of both technologies in a tandem solar cell (TSC) not only harnesses the individual benefits of each, but also holds the potential to surpass the efficiencies achievable by silicon solar cells.

1.1. Efficiency limit of tandem solar cells

The general working principle of solar cells is as follows: A photon is absorbed by a semiconductor and elevates an electron from the valence band to the conduction band[12]. This process creates an electron-hole pair, which is separated and directed to different electrodes by a built-in electric field generated by an electron transport layer (ETL) and a hole transport layer (HTL)[12]. The resulting charge separation produces an electrical potential proportional to the energy difference between the valence and the conduction band (called band gap E_g)[12].

But solar cells, like all energy-converting technologies, face limitations in efficiency. In solar cells with a specific band gap, intrinsic losses occur (Figure 1a), such as photons with energy below E_g not being absorbed. Only photons exceeding E_g can elevate electrons from the valence to the conduction band. Yet the surplus energy remains unutilized and is lost through thermalization via electron-phonon coupling, generating heat. Additional losses stem from thermodynamic processes such as the Boltzmann and Carnot loss. Moreover, some of the generated excited charge carriers recombine radiatively, reemitting photons[13,14].

For a silicon solar cell with a band gap of 1.1 eV, losses due to sub-band gap photons, thermalization, thermodynamics, and radiative recombination are 16.5, 37.9, 13.4, and 1.0 %, respectively[13]. Implementing multiple absorbers in multijunction solar cells minimizes thermalization and sub-band gap photon losses but necessitates precise band gap matching to avoid spectral absorption mismatches[13]. In TSCs, two junctions are stacked, raising the theoretical maximum efficiency limit to 43 % (with band gaps of 0.98 eV and 1.87 eV)[13].

Semiempirical models are used to optimize band gap matching in perovskite organic TSCs. The models illustrate the efficiency as a function of the band gaps of the organic and perovskite subcell (Figure 1b)[15]. In addition to intrinsic losses, this approach accounts for a 0.4 V loss in open circuit voltage (V_{OC}) and a fill factor (FF) of 85 %. Efficient organic solar cells can currently achieve a band gap down to 1.1 - 1.3 eV, which requires a perovskite subcell with a band gap of 1.70 - 1.85 to reach an efficiency of approximately 30 %[15,16].

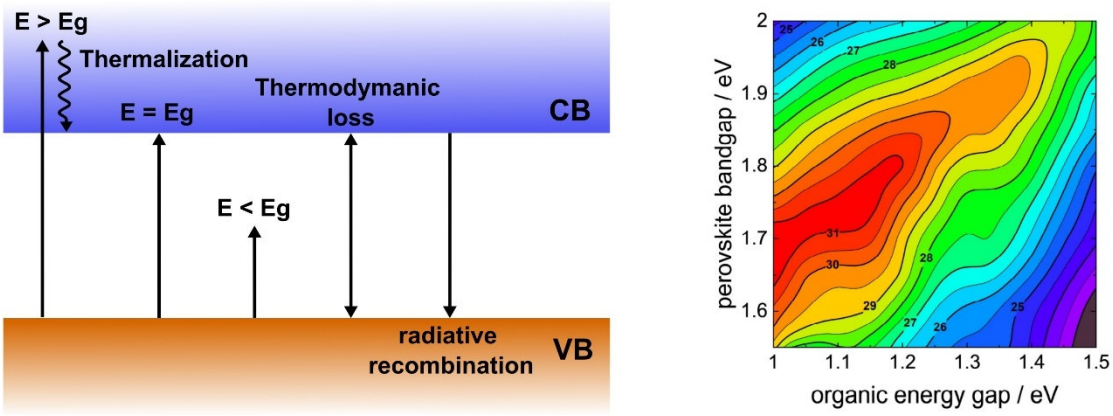

Figure 1. a) Schematic representation of the intrinsic losses in solar cells with one absorber. Pictured in an energy band diagram with conduction band (CB) and valance band (VB). Intrinsic losses include: Thermalization loss of excess energy of photons with an energy higher than the band gap (E_g), photons with lower energy than the band gap not being absorbed, thermodynamic loss and radiative recombination of electrons and holes. **b)** Semi-empirical model of perovskite organic tandem cell efficiency vs. band gap of the organic and perovskite sub-cell considering a scenario with 0.4 V loss in V_{OC} compared to E_g/q in each cell and an overall FF of 85 %. Reproduced from K. O. Brinkmann et al.[15] with permission from Springer Nature.

1.2. Wide band gap perovskite solar cell

PSCs have evolved significantly since the first demonstration in 2009, progressing from an initial efficiency of 3.8 %[17] to an impressive 26.1 %[2] today. Characterized by an ABX_3 crystal lattice structure (Figure 2a), perovskites consist of a monovalent cation A, such as methylammonium (MA), ethylammonium (EA), formamidinium (FA) or cesium (Cs^+), alongside a divalent cation B, typically lead (Pb), and a halogen anion X, encompassing chlorine (Cl), bromine (Br) or iodine (I)[18]. While record efficiencies are achieved with $MAPbI_3$ its band gap of approximately 1.5 - 1.6 eV is suboptimal for organic perovskite TSCs[19]. To achieve optimal band gap matching, an efficient OSC with a band gap below 1 eV would be necessary, however, such cells have not yet been developed[15]. Perovskites offer a tunable band gap, enabling customization to match the bandgap of the OSC[18]. Cells with a band gap exceeding 1.65 eV are classified as wide band gap perovskite solar cells (WBG PSC)[18]. Mixed halide perovskites facilitate band gap modulation by adjusting the iodine and bromine content[18]. Nevertheless, methylammonium mixed halide perovskites demonstrate thermal instability beyond 85°C, constraining their practical utility[20]. Formamidinium, characterized by enhanced thermal stability and a lower dipole moment (0.21 D) compared to MA (2.29 D), additionally increases the stability against moisture and polar

solvents[21]. However, $FAPb(I_{1-x}Br_x)_3$ compositions tend to exhibit no-stable perovskite phases within the $0.3 < x < 0.6$ range[22]. Partially, incorporating cesium as A site cation stabilizes the phase across the entire x range[22].

1.2.1. Open circuit voltage deficit

One significant challenge faced by WBG PSC is the occurrence of substantial V_{OC} deficits[23,24]. V_{OC} deficit can be quantified as $E_g/q - V_{OC}$, where E_g represents the band gap and q denotes the elementary charge. While a $MAPbI_3$ PSC with a band gap of 1.6 eV may have a V_{OC} deficit as low as 0.34 V[23], a WBG PSC based on the composition $Cs_{0.2}FA_{0.8}Pb(I_{0.5}Br_{0.5})_3$ with a band gap of 1.86 eV experiences a V_{OC} deficit of 0.69 V[24]. The underlying reasons for this phenomenon can be attributed to three primary factors: defect-assisted non-radiative recombination[25,26], interface-induced recombination[27–29], and phase segregation[30–32].

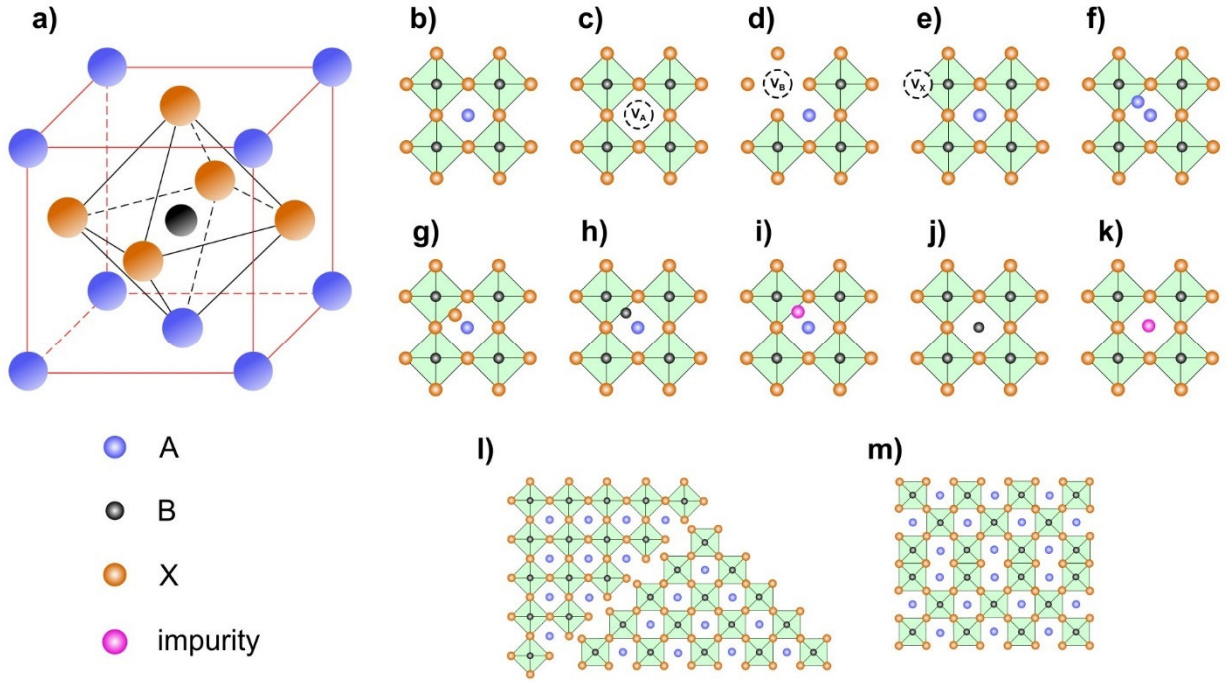

Figure 2. a) Crystall lattice of an ABX_3 perovskite. With A-site typically being a formamidinium, methylammonium, or cesium cation, B-site being mostly Pb^{2+} and X-site being a halogen anion. Figures on the right hand side showing defects in the perovskite crystal lattice with **b)** ideal perovskite lattice, **c)** vacancy of cation A, **d)** vacancy of cation B, **e)** vacancy of anion X, **f)** interstitial with cation A, **g)** interstitial with anion X, **h)** interstitial with cation B, **i)** interstitial with impurity, **j)** antisite of cation A, **k)** antisite with impurity, **l)** grain boundaries, **m)** lattice dislocation.

One source of V_{OC} deficit stems from non-radiative recombination assisted through defects and their underlying trap states. Point defects such as vacancies (Figure 2c - e), interstitials (Figure 2f - h), antisites (Figure 2j), and impurities in the crystal lattice (Figure 2i - k) generate trap states within the band gap[33,34]. The contribution of these trap states to non-radiative recombination depends on whether they are shallow (near the CB or VB) or deep (proximate to the mid-band gap)[25]. Shallow trap states, such as vacancies, have a low energy of formation and are thus frequent, but they have a limited impact on non-radiative recombination[25]. Conversely,

deep-level defects, such as antisites or interstitials, have a significant impact on non-radiative recombination[26]. However, due to their high energy of formation, these deep defects are less frequent[26]. This rarity of deep-level defects contributes to the long electron-hole diffusion length and high V_{OC} observed in PSCs[35]. Other centers for non-radiative recombination are structural defects of perovskite crystals like grain boundaries, (Figure 2l) and crystallization shifts (Figure 2m)[36,37]. It is important to be aware that the perovskite layer consists of various crystal grains with different sizes. At the grain boundaries defects, unsaturated bonds (dangling bonds), and impurities are concentrated which serve as non-radiative recombination centers[36,37].

Another source of V_{OC} deficit can be attributed to interface-induced recombination[27,28]. The factors influencing this recombination encompass energy level alignment, interface morphology, and charge carrier mobility[27]. Energy level mismatch between transport layers and the perovskite can directly prompt interface recombination. Researchers have demonstrated that an energy level misalignment between the perovskite and the HTL can induce band bending of the HTL energy level near the contact, resulting in a pronounced exponential rise in recombination[27].

Light-induced phase segregation is another contributor to the V_{OC} deficit observed in WBG PSCs. Phase segregation was first reported by Hoke et al. in a $MAPb(Br_xI_{1-x})_3$ perovskite[32]. They observed a second red-shifted peak in photoluminescence (PL) spectra under 100 mW cm^{-2} illumination in less than a minute. X-ray diffraction measurements indicated that illumination induced a segregation of halides into bromide and iodide-rich crystal phases, resulting in an increase in the band gap of the bromine-rich phase and a decrease in the band gap in the iodine-rich phase[32]. Estimations propose that the fraction of segregated perovskite is minimal, approximately 1 %, yet charge carriers can be trapped and channeled to the lower band gap iodine-rich perovskite phase, serving as recombination centers responsible for the disproportionately heightened second redshifted PL emission[30,32,38]. This phase segregation is not only caused by illumination, but also through charge-carrier injection, as proved by electroluminescence measurements[29]. Moreover, phase segregation has been demonstrated to be reversible, with the initial characteristics of the PL spectra being restored after a period of storage in darkness[31,32].

1.2.2. Minimizing open circuit voltage deficits

To tackle the V_{OC} deficit of WBG PSCs, various options are explored by the scientific community such as additive engineering[39–41], surface passivation[42,43], and film quality optimization[44]. Reducing one source of V_{OC} loss often minimizes other sources as well. For example, defects in the perovskite layers also enhance phase segregation[15]. Therefore, optimizing the film quality reduces both defected assisted non-radiative recombination and phase segregation.

MACl is widely used as an additive to facilitate preferential orientation and increase carrier mobility inside the perovskite[39,41,45]. With a MACl additive, crystals tend to form vertical columns, therefore increasing crystal grain size and minimizing grain boundaries[45]. Studies suggest that the preferential orientation is induced through the start of the growth at the liquid-air interface rather than randomly at both the substrate liquid interface and bulk [45,46]. MACl, however, is thought to escape the perovskite film since only trace amounts of Cl can be found in the perovskite[47].

Thiourea is another additive that increases the performance of PSCs. It has been shown that crystal grain size is increased by the addition of thiourea, resulting in faster charge transport and reduced trap states[48]. The formation of a $PbI_2 \cdot$thiourea intermediate phase has been shown to benefit crystallization dynamics towards larger grain size[40]. Furthermore, thiourea can fill halide vacancies coordinating with the lone pair to Pb^{2+} effectively reducing trap states[15,48]

Surface passivation with PEAI has also been shown to be highly effective. A post-treatment of PEAI on the perovskite film helps to passivate the surface of perovskite grain boundaries, reducing trap-induce recombination and therefore increasing the V_{OC} [42,43].

Another advancement in film formation control was brought by the antisolvent technique. For this, the perovskite film is spin-coated, and after a specific spinning time, a solvent, unable to dissolve the perovskite (hence antisolvent), is dynamically applied. This greatly enhances the film morphology yielding larger grains and a more uniform film[44].

Interface engineering is an effective method for minimizing the V_{OC} deficit caused by interface-induced recombination, and it can also reduce phase segregation. Interestingly, a material called MeO-2PACz can have benefits both to enhance selective hole extraction and also to limit photoinduced phase segregation[41,49]. With a MeO-2PACz self-assembled monolayer no halide segregation was observable for up to 30 minutes upon illumination[15].

1.3. Organic solar cells

The foundation of OSCs lies in the semiconducting properties found in organic molecules with a conjugated π-electron system, which generates a conduction and a valence band similar to those found in classical inorganic semiconductors[50]. Subsequently, the potential of this material class for the conversion of light into electricity was realized and rapidly evolved[51]. The discovery of semiconducting polymers thereby marked a significant milestone in the evolution of OSCs[52]. The next breakthrough was the recognition of the necessity for an interpenetrating network comprising two semiconductive organic materials to achieve functionality[53]. This system, known as bulk heterojunction, involves the formation of a three-dimensional interpenetrating network of a donor (D) and an acceptor (A) with a high interfacial area. The charge generation and separation mechanisms in a bulk heterojunction solar cell are illustrated in Figure 3a. Upon photon absorption

in the donor material, an exciton, consisting of an electron-hole pair, is generated[54]. Unlike conventional Si or perovskite-based solar cells, the exciton cannot spontaneously dissociate due to its significantly higher binding energy in the range of 0.2 - 0.5 eV[54]. Consequently, the exciton must migrate to the acceptor moiety, where the excited electron is transferred to the acceptor material with a slightly lower LUMO level, facilitating exciton dissociation[54]. Following this separation, the electron and hole traverse through the material driven by the built-in potential, ultimately reaching different electrodes to yield a potential difference, hence generating electricity[54].

For a long period, OSCs employing the polymer donor poly(3-hexylthiophene-2,5-diyl) (P3HT) and the fullerene acceptor phenyl-C61-butyric acid methyl ester (PCBM) were leading the development of OSC[55]. Devices achieving a power conversion efficiency (PCE) of nearly 5 % (V_{OC} = 0.63, J_{SC} = 9.5 mA cm^{-2}, FF = 68 %) were fabricated 2005[56]. Subsequently, the repertoire of donor and acceptor molecules expanded significantly. Notably, the incorporation of non-fullerene acceptors enhanced the efficiency of OSCs[57,58]. Non-fullerene acceptors offer various advantages such as a broader absorption spectrum[59], tunable energy levels[59], reduced voltage losses[60] and enhanced stability[61]. A key benefit of non-fullerene acceptors for tandem applications is the ability to absorb light in the near-infrared (NIR) with a band gap below 1.5 eV[62-64]. The OSC investigated in this study employs the donor PTB7-Th (Figure 3b) with a band gap of 1.61 eV (HOMO = -5.20 eV, LUMO = -3.59 eV)[65] and the non-fullerene acceptor IEICO-4F (Figure 3c) with a band gap of 1.25 eV (HOMO = -5.44 eV, LUMO = -4.19 eV)[60].

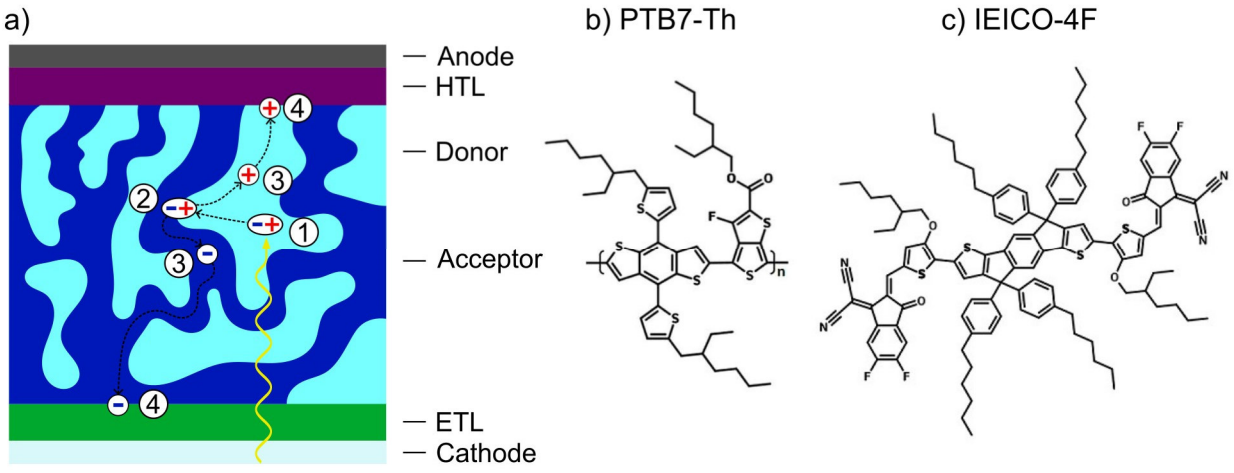

Figure 3. **a)** Schematic illustration of the working principle of a BHJ OSC: 1) light absorption and exciton generation, 2) diffusion towards D/A interface, 3) charge transfer with exciton splitting, 4) collection of charges at the electrodes. **b)** molecular structure of IEICO-4F **c)** molecular structure of PTB7-Th.

1.4. Perovskite organic tandem solar cells

In a two-terminal monolithic TSC, the top cell and the bottom cell are connected in series through an interconnecting layer (ICL), comprising an ETL, a recombination layer (RL), and an HTL (Figure 4a). TSCs can be fabricated in standard structure (n-i-p) or inverted-structure (p-i-n). In a series connection of two electronic components (top and bottom cell) the voltages add up while the current is determined by the lowest of the two[66]. Therefore, the currents of both cells must be carefully matched[66]. Figure 4b provides an energetic overview of the processes occurring in a TSC in p-i-n configuration. In both the front and rear subcells electrons and holes are generated by light absorption[12]. Within the ICL, electrons from the front subcell recombine with holes from the rear subcell[12]. The remaining charge carriers - now in separate subcells - eventually reach their respective electrodes, which leads to an addition of the voltages of the subcells[12].

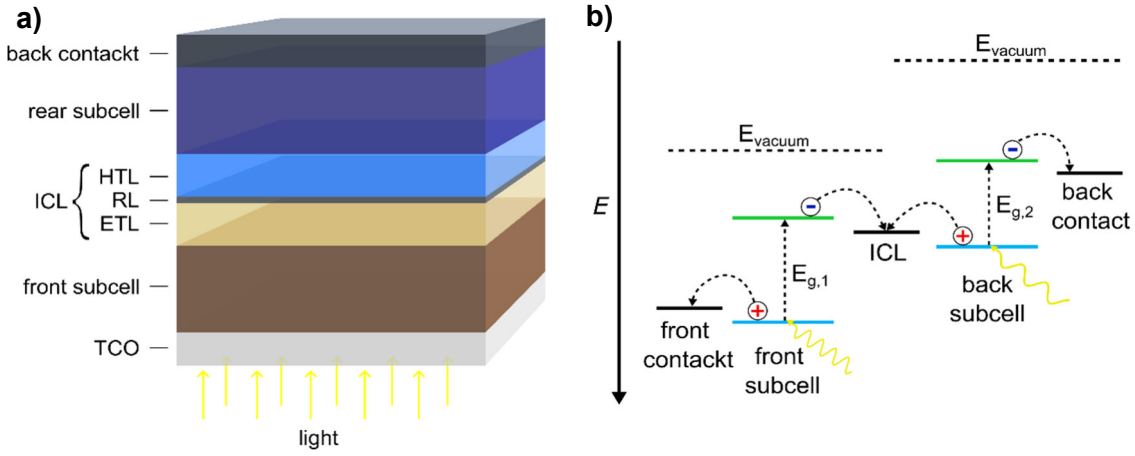

Figure 4. a) Schematic structure of a tandem solar cell with the interconnecting layer (ICL) consisting of an electron transport layer (ETL), recombination layer (RL) and a hole transport layer (HTL). **b)** Energetic scheme of the processes in a tandem solar cell with light absorption in both subcells followed by recombination of electrons and holes in the ICL and collection of carriers at different electrodes.

1.4.1. The interconnecting layer

The ICL is the heart of a tandem device. Several properties have to be fulfilled in order to have an efficient ICL. It has to facilitate efficient recombination of holes from the rear subcell with electrons from the front cell, while being highly transparent, having a selectivity towards the respective charge carriers, and it has to protect the front subcell from damaging solvents/deposition methods[15,66–76].

To achieve efficient recombination of charge carriers an RL with a high conductivity is usually introduced between the HTL and ETL, whereby the metals Ag[70,71,74,75,77] and Au[67] are frequently employed. The drawback of using even very thin layers of metals (<5nm) is that the parasitic absorption increases dramatically[15]. The absorption of light in the ICL reduces the current in the rear subcell limiting the overall efficiency of the TSC[15]. Transparent conductive oxides (TCO) such as aluminum-doped zinc oxide (AZO), indium zinc oxide (IZO) or indium tin oxide (ITO) are

an alternative since they possess high conductivity, high transparency and offer protection against solvents [73,78]. The drawback is that these TCOs are usually deposited by sputtering which poses a high risk of damaging the front subcell[15].

Another possibility to connect two subcells in a TCS is to create a tunneling-junction[79]. This is achieved by direct contact of a heavily doped HTL and ETL[79]. The high abundance of opposite free charge carriers in the ETL and HTL leads to the formation of a potential barrier with small width and height[79]. This allows opposite charge carriers to quantum mechanically tunnel through the barrier and form an ohmic contact between the subcells[79].

For the HTL and the ETL in the ICL the same materials as for single solar cells are used, but the energy levels have to be aligned accordingly[15,70]. Several HTLs, ETL, as well as RLs and their energy levels/ work functions are depicted in Figure 5. Misaligned energy levels can lead to a Schottky barrier (potential energy barrier) between the metal and the semiconductor resulting in a junction that exhibits rectifying behavior (allowing current to flow more easily in one direction than the other)[80]. The presence of a Schottky barrier in the ICL of a TSC is detrimental to all key performance metrics (V_{OC}, J_{SC}, FF, PCE) and is one reason for an S-shape in current density voltage curves[80].

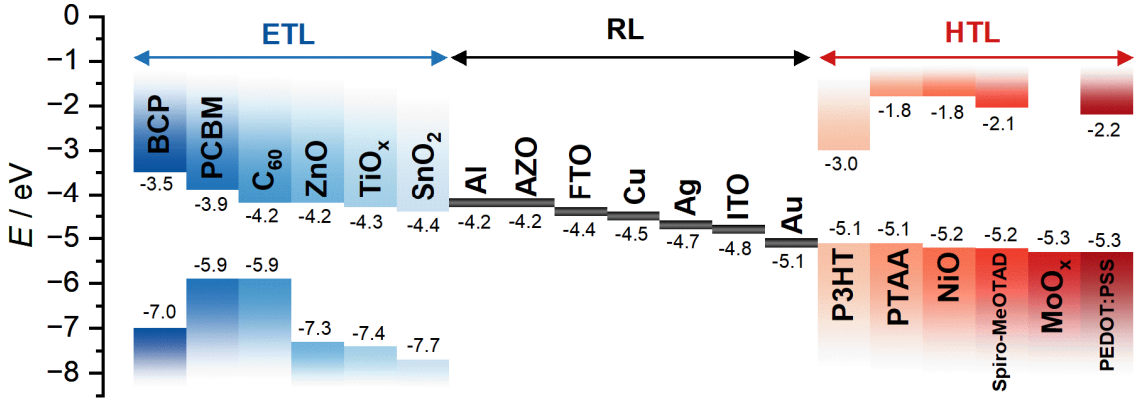

Figure 5. Energy levels of various electron transport layers (ETLs), recombination layers (RLs), and hole transport layers (HTLs) with values from references[81–85].

1.4.2. Current examples of perovskite organic tandem solar cells

There are several recent reports of successfully fabricated perovskite organic TSCs. Wang and coworkers designed an ICL with a configuration of C60/BCP/Au/MoO_x[77]. They realized a high V_{OC} of 1.35 V of their front WBG PSC ($FA_{0.8}Cs_{0.2}Pb(I_{0.5}Br_{0.5})_3$) through a mixed cation passivation strategy based on 4-trifluoro phenethyl ammonium and ethylenediammonium. The organic rear subcell consists of the quaternary mixture PM6, PM7, Y6, and PCBM, with an EQE of over 80 % in the near-infrared region. This device resulted in a PCE of 24.5 % (V_{OC} = 2.14 V,J_{SC} = 14.2 mA cm^{-2}, FF = 81 %).

Brinkmann et al. employed an ICL based on PCBM/AZO NP/SnO_x/ InO_x/MoO_x[15]. They deposited tin oxide (SnO_x) by atomic layer deposition to generate a permeation barrier for subsequent treatments. A thin InO_x layer (~1.5 nm) prevents the formation of a Schottky barrier between SnO_x and MoO_x, ensuring efficient transport of electrons across the ICL. Together with a WBG PSC front subcell based on $FA_{0.8}Cs_{0.2}Pb(I_{0.5}Br_{0.5})_3$ with a high V_{OC} of 1.34 V and a narrow-gap organic subcell with the ternary photoactive layer PM6:Y6:PCBM. The finished tandem device yielded an astonishing PCE of 24.0 % (V_{OC} =2.15V, J_{SC} = 14.0 mA cm^{-2}, FF = 80 %).

2. Experimental

All solution preparation and spin-coating steps were performed in a nitrogen-filled glove box (O_2 <20 ppm, H_2O <0.1 ppm) at 22 °C. All thermal evaporations were performed using the UNIVEX 350 evaporation system from Leybold at a pressure below 4 x 10^{-6} mbar unless stated otherwise.

2.1. Materials

Table 1. Used material, supplier, purity and abbreviation.

Material	Supplier	Purity / %	Abbreviation
Acetone	VWR Chemicals	technical	-
1-Butanol	Sigma-Aldrich	99.8	BuOH
1-Butyl-1-methylpyrrolidinium bis(fluorosulfonyl)imide	Proionic	-	BMPyrr-FSI
Bathocuproine	Sensient Imaging	-	BCP
Caesium bromide	Thermo Fischer Scientific	99.999	CsBr
Chlorobenzene	Alfa Aesar	99.8	CB
Chloroform	Sigma-Aldrich	99	CF
(2-(3,6-Dimethoxy-9H-carbazol-9-yl)ethyl)phosphonic acid	TCI Chemicals	>98.0	MeO-2PACz
Dimethylsulfoxide	Sigma-Aldrich	99.9	DMSO
1-Ethyl-3-methylimidazolium bis(fluorosulfonyl)imide	Proionic	-	EMIM-FSI
1-Ethyl-3-methylimidazolium tetrafluoroborate	Proionic	-	EMIM-BF_4
Ethanol, absolut	VWR Chemicals	99.8	EtOH
Formamidinium bromide	synthesized	-	FABr
Hydrochloric acid	VWR Chemicals	37	HCl
IEICO-4F	1-Material	-	IEICO-4F
Indium doped tin oxide on glass	Xinayan Hongkong	-	ITO
Lead (II) bromide	Sigma-Aldrich	99.999	PbBr2
Lead (II) iodide	Thermo Fischer Scientific	99.9985	PBI2
Methanol	VWR Chemicals	99.8	MeOH
Methylammonium chloride	Greatcellsolar	99.99	MACl
Molybdenium oxide	Kurt J. Lesker	0.9995	MoO_x
N,N'-Bis[3-(dimethylamino)propyl]perylene-3,4,9,10-tetracarboxylic diimide	1-Material	-	PDIN
N,N-Dimethylformamide	Sigma-Aldrich	99.8	DMF
N-Methyl-2-pyrrolidine	Alfa Aesar	99.5	NMP
2-Propanol	VWR Chemicals	100	IPA
Phenethylammonium iodide	Sigma-Aldrich	98	PEAI
Phenyl-C61-butyricacidmethylester	Solenne	99	PCBM

Table 2. Used material, supplier, purity and abbreviation.

Material	Supplier	Purity / %	Abbreviation
Poly(3,4-ethylenedioxythiophene):complex (Clevious HTL Solar 3)	Heraeus	-	Solar 3
Poly(3,4-ethylenedioxythiophene):poly(styrenesulfonate) (Clevios Al4083)	Heraeus	-	Al4083
Poly(3-hexylthiophen-2,5-diyl)	Rieke	-	P3HT
Polymethylmethacrylat (M_w = 350 000)	Sigma-Aldrich	-	PMMA
PTB7-Th	1-Material	-	PTB7-Th
Silicon monoxide	Kurt J. Lesker	99,99	SiO_x
Silver shoot	Sigma-Aldrich	99.9999	Ag
Tetrahydrofuran	VWR Chemicals	99	THF
Thiourea	Sigma Aldrich	99	-
Titanium oxide	synthesized	-	TiO_x
Toluene	VWR Chemicals	99.0	Tol
Triton X-100	Sigma-Aldrich	-	Triton
Zonyl FS-300	abcr	-	Zonyl

2.2. Substrate cleaning

Substrates with different sizes were prepared for the different solar cell types. The single absorber substrates with a size of 2.54 x 2.54 cm were used for single WBG PSCs and PTB7-Th:IEICO-4F OSCs, while small substrates (1.5 x 1.5 cm) were used for P3HT:PCBM cells. Tandem substrates had a size of 2.6 x 2.6 cm and were used for perovskite organic TSCs.

To prepare single absorber substrates, a 2.54 cm strip of ITO-coated glass was cut and a 1.5 cm section at the center was protected using a PVC tape. Subsequently, the prepared glass/ITO slide underwent a 15-minute submersion in concentrated hydrochloric acid to selectively etch away the ITO from the unprotected areas. This step was crucial to prevent electrical shortcuts during the characterization of the finalized cell. Following etching, the glass/ITO slide was thoroughly rinsed with water, and any residual PVC tape adhesive was removed using toluene. The slide was then sectioned into 2.54 x 2.54 cm squares, which were subjected to further cleaning in a 2 vol% Hellmanex III solution in water at 80 °C for 30 min in an ultrasonic bath. Subsequently, the substrates underwent three cycles of cleaning in deionized water for 5 min each. Finally, the substrates were cleaned sequentially in acetone and IPA for 30 minutes each before being stored in IPA until required. Before use all substrates were treated with an O_2 plasma in a Plasma Etch PE-25 plasma cleaner at 100 W for 10 min.

For the small substrates used in P3HT:PCBM cells a 1.5 cm strip of ITO-coated glass was cut out and 1 cm of the edge was protected with PVC-tape following etching for 15 min in conc. HCl. The rest of the cleaning procedure was identical to that of the single absorber substrates.

For the tandem substrates a 2.6 x 2.6 cm square of ITO on glass was prepared. A specific pattern (Figure 6a) of the ITO was produced using a Speedy 300 laser cutter (Trotec) equipped with a fiber laser with a maximum power of 30 W and a maximum speed of 3.55 m s^{-1}. To test the residual conductivity of the patterned ITO, an ITO/glass sample (Figure 6b) was patterned at different laser speeds/laser powers and measured using a multimeter (Table 13, appendix). Furthermore, microscope pictures were taken of different laser speeds, laser power (Figure 37, appendix) and laser pattern directions as well as with an offset of 50 µm (Figure 38, appendix). Good results were achieved with a laser power of 20 % and a laser speed of 20 %, which was selected to be used for the substrate of the TSC. With these parameters the same area of the substrate was patterned three times: 1. landscape, 2. portrait, 3. landscape with 50 µm offset vertically. Starting with the ultra-sonification in a 2 vol% Hellmanex solution, the cleaning protocol for the tandem substrates followed the same procedure as for the single absorber substrates.

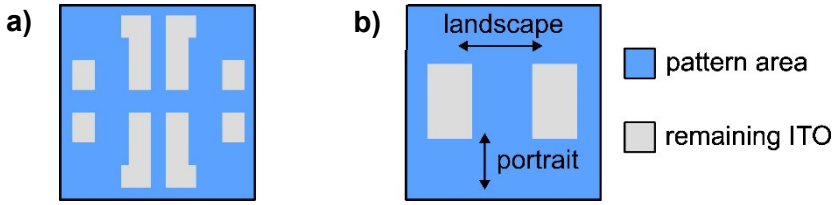

Figure 6. Representation of the laser patterned areas of ITO of the ITO/glass slides with **a)** used in the tandem solar cell **b)** used to test the residual conductivity between two ITO patches.

2.3. Device overview and spin-coating programs

Figure 7a - c provides an overview of the device architectures of the single PSC, single OSC and the completed TSC. Additionally, Table 3 details the respective spin-coating programs used for each layer and the resulting layer thicknesses.

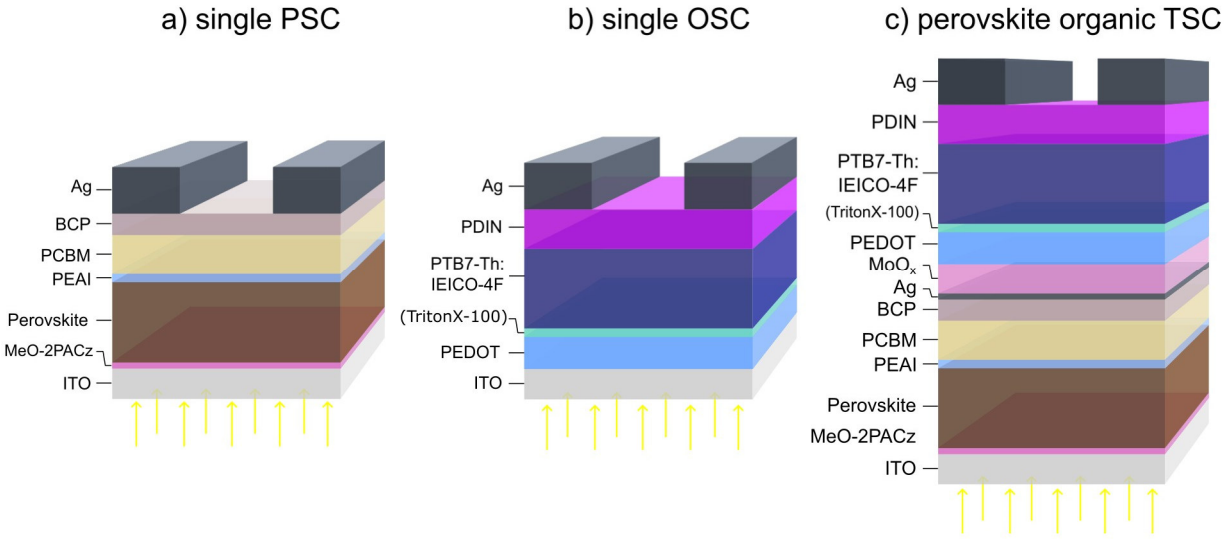

Figure 7. Overview of all the layers of the devices fabricated in this thesis. Glass substrate below the ITO is not pictured. Yellow arrows indicate direction in which light passes into the cell. With **a)** single mixed halide wide band gap perovskite solar cell (PSC), **b)** single organic solar cell with the donor acceptor PTB7-Th:IEICO-4F, **c)** combined perovskite organic tandem solar cell (TSC).

Table 3. Overview of the spin-coating programs for processing layers of the single perovskite, single PTB7-Th:IEICO-4F organic solar cell, P3HT:PCBM organic solar cell and perovskite organic tandem solar cell including the resulting film thicknesses.

Layer	rpm / min^{-1}	ramp / rpm s^{-1}	*t* / s	Thickness / nm
MeO-2PACz	3000	1500	30	-
Perovskite	480	480	1	250
	4000	2000	50	
PEAI	480	480	1	-
	4000	2000	50	
PCBM	1300	650	16	100
	2000	1000	15	
BCP	4000	2000	30	15
Al4083	3000	1500	45	42
Solar 3	5000	2500	30	45
Solar 3 – film treatment	1500	750	2	-
	4000	2000	20	
P3HT:PCBM	1500	750	2	100
	4000	2000	20	
PTB7-Th:IEICO-4F	1500	750	2	82
	4000	2000	20	
PDIN	5000	2500	30	15
TiO_x	5000	2500	30	-

2.4. Wide band gap perovskite solar cells

2.4.1. Wide band gap perovskite solar cell processing

The perovskite used in this study was a wide band gap mixed halide perovskite with a composition of $FA_{0.8}Cs_{0.2}Pb(I_{0.5}Br_{0.5})_3$. For 1 mL of perovskite precursor solution, 345.76 mg PbI_2, 91.75 mg $PbBr_2$, 42.56 mg CsBr, and 99.98 mg FABr were weighed and dissolved in 200 µL NMP as well as 800 µL DMF. This resulted in a solution with a Pb concentration of ~1 mol L^{-1}. For the testing of the effect of the MACl additive, 2 or 3 mg mL^{-1} was added. Additionally, solutions of 0.5 mg mL^{-1} BCP in EtOH, 0.3 mg mL^{-1} MeO-2PACz in EtOH, 0.25 mg mL^{-1} PEAI in IPA, and 20 mg mL^{-1} PCBM in CF:CB = 3:1 were prepared. The perovskite precursor solution was filtered through a 0.2 µm PTFE syringe filter (fisher scientific) and 10 µL of a thiourea solution in DMF (100 mg mL^{-1}) was added to 1 mL solution after the filtration.

Immediately after plasma treatment of the pre-cleaned single absorber substrate, 180 µL of the MeO-2PACz solution was spin-coated and annealed at 100 °C for 10 min. The programs for this and all other layers are detailed in Table 3. Subsequently, the perovskite layer was spin-coated, preceded by a wetting step with 200 µL of MeOH conducted with an antisolvent pump 20 seconds

before the end of the perovskite spin-coat program (200 µL s^{-1}). The syringe of the antisolvent pump (1 mL) was positioned slightly off centered the middle of the substrate and 3 mm above it. After the end of the spin-coating program, the perovskite precursor solution (160 µL) was quickly deployed, and the program started, with 200 µL CB as antisolvent dripping (200 µL s^{-1}) either 17 or 22 seconds after the start. The substrate was immediately put on a heating plate at 65 °C for 2 min, followed by 10 min at 100 °C. The annealing step was interrupted for the patterning of the substrate's edges with a cotton swab soaked in 40 µL DMF. For cells with a PEAI passivating layer, 160 µL of the PEAI solution was spin-coated and annealed at 100 °C for 10 min. The PCBM and BCP layers were deposited using 150 µL and 180 µL of the solutions respectively with no annealing required. The substrates were patterned with a cotton swab soaked in 40 µL CB. Lastly, 100 nm of an Ag top contact were thermally evaporated with a shadow mask to yield an active area of around 0.18 cm^2.

2.4.2. Electron transport layer variation

To optimize the PCBM layer, PMMA incorporation into the PCBM solution at varying concentrations (0.1 mg mL^{-1}, 1 mg mL^{-1}, 5 mg mL^{-1}) was tested. The spin-coating program and all subsequent procedures remained consistent with those used for samples without PMMA.

Secondly, an alternative ETL configuration was examined, replacing the BCP layer with a TiO_x layer. The standard cell architecture was retained and TiO_x was deposited via spin-coating using a nanoparticle suspension. Thickness modulation of the TiO_x layer was achieved by diluting the stock solution with IPA at different rations (stock solution:IPA): 1:100, 1:200, 1:300, 1:1000. Following spin-coating the layer underwent immediate annealing at 108 °C outside the glovebox to facilitate oxidation. Additionally, cells were tested using both Ag and Al top contacts.

2.4.3. SiO_x protection for perovskite solar cells

For EQE and PL measurements, the perovskite cells were encapsulated with a SiO_x protection layer to mitigate the damaging effects of ambient air and moisture. Consequently, a 400 nm layer of SiO_x was thermally evaporated ("Silver Eve", Leybold) onto the finished PSC trough a shadow mask leading to a coverage of a 2 x 2 cm square in the center of the substrate. To evaluate the cells storage stability under ambient conditions (40 - 60 %RH, 22 °C), the cells were subjected to a test, where one group of cells was coated with the protective SiO_x layer while another group was left uncoated. Additionally, one group of cells was stored in a nitrogen-filled glove box for reference. The cell performance was assessed after 15, 21, 40, 165, 212, 352, 455, 1168 and 2709 hours. SiO_x protected cells were used for measurements under ambient conditions.

2.4.4. Temperature and solvent and stability

For the temperature stability tests finished PSC were exposed to different temperatures on a heating plate for 10 minutes and the cell performance was evaluated before and after. Temperatures from 50 °C to 140 °C in 10 °C steps were tested.

To test the possible damaging effects of various solvents, fished PSC where used. The solvent stability towards MeOH, EtOH, IPA, BuOH, Tol, CB, CF, DMSO, 1 vol% TritonX-100 and 5 vol% TritonX-100 in IPA. 200 µL of the respective solvent was deposited on top of the cell and the cell was exposed 30 seconds to the solvent before the spin-coating program (1. 1500 rpm, 750 rpm s^{-1}, 2 s; 2. 4000 rpm, 2000 rpm s^{-1}, 20 s) was started. The cell performance was evaluated before and after the solvent treatment.

2.5. Organic solar cells

2.5.1. Enhancing PEDOT Solar 3 performance on P3HT:PCBM solar cells

To optimize the exchange of the PEDOT:PSS suspension in water (Al4083) to a PEDOT suspension in toluene (Solar 3), a model system employing the active layer P3HT:PCBM was utilized. Various film treatments of Solar 3 were investigated to achieve comparable performance to that of Al4083.

Solar 3 was diluted with toluene (Solar 3:Tol = 70:30) and filtered through a 0.45 µm PTFE filter (Fischer Scientific). Al4083 underwent filtration through a 0.45 µm PES syringe filter (Cytiva). For the PCBM:P3HT solution 17 mg mL^{-1} P3HT and 11.9 mg mL^{-1} PCBM were dissolved in CB (P3HT:PCBM = 1:0.7). The solution was stirred at 60 °C for at least 6 hours. Additionally, a 2 mg mL^{-1} PDIN suspension in MeOH was prepared for the ETL of the system, and 2.5 µL glacial acetic acid was added for complete dissolution.

The P3HT:PCBM cells were prepared on small substrates. Immediately following plasma treatment, the PEDOT layer was spin-coated. For each batch of P3HT:PCBM cells, at least one substrate was dedicated to Al4083 as a reference standard. Al4083 was spin-coated at ambient conditions and patterning was done with a cotton swab soaked in deionized H_2O before annealing at 140 °C for 15 minutes. The Solar 3 layer was patterned using a toluene-soaked cotton swab with annealing performed at 100 °C for 10 minutes.

Post-treatment procedures aimed to enhance the HTL properties were carried out using 100 µL of various solutions/solvents, as outlined in Table 4. Two procedures were employed: dynamic application during spinning or a static method with the application of the solvent and 30 seconds of exposure time before spin-coating. The spin-coating program remained consistent across both methods. Substrates with a Al4083 HTL did not undergo post solvent-treatment. All subsequent layers were processed identically for both PEDOT variants.

After post-treatment of the PEDOT layer, the P3HT:PCBM layer was spin-coated and annealed at 110 °C for 5 minutes. The ETL (PDIN) was spin-coated last and did not require annealing. The substrates were patterned with a cotton swab soaked in 40 µL CB. Finally, a 100 nm Ag layer was thermally evaporated as the top contact ("Silver Eve", Leybold).

Table 4. Overview of the solutions/solvents used for post-treatment on the Solar 3 layer to optimize the charge transport properties. Dynamic methods were performed during spinning and in static methods the spin-coating program was started after application of the treatment.

Solution/Solvent	Method
IPA	dynamic
MeOH	dynamic
1 vol% DMSO in IPA	dynamic
5 vol% DMSO in IPA	dynamic
DMSO	dynamic
1. DMSO 2. MeOH	dynamic
n-butanol	static
5 vol% Zonyl in IPA	static
1 vol% TritonX-100 in IPA	static
5 vol% TritonX-100 in IPA	static
1 vol% EMIM-FSI in THF	static
1 vol% EMIM BMPyrr-FSI in THF	static
1 vol% EMIM BF4 in THF	static

2.5.2. PTB7-Th:IEICO-4F solar cell fabrication

The optimized Solar 3 layer was tested with the active layer PTB7-Th:IEICO-4F, which will be used in the TSC. Furthermore, an alternative HTL with thermally evaporated MoO_x as well as a combination of both MoO_x and Solar 3 with post-treatment were tested. For reference, cells employing Al4083 were fabricated as well.

The procedure for fabricating the OSCs utilizing PTB7-Th:IEICO-4F absorber closely resembled that of P3HT:PCBM cells. Details regarding the preparation of Al4083, Solar 3, and PDIN solutions are provided in Section 2.5.1. The PTB7-Th:IEICO-4F solution was prepared by dissolving PTB7-Th (9 mg mL^{-1} D) and IEICO-4F (6 mg mL^{-1} A) in CB (D:A = 1:1.5) and stirring overnight.

The cells were processed with single absorber substrates. Al4083 and Solar 3 were spin-coated according to Table 3 directly after plasma treatment. MoO_x with a thickness of 10 nm was thermally evaporated. Post-treatment of Solar 3 was done with 200 µL 1 vol% TritonX-100 solution in IPA. The PTB7-Th:IEICO-4F and the final PDIN layer was spin-coated according to Table 3 and no annealing was required. Finally, a 100 nm Ag top contact was thermally evaporated.

2.6. Tandem cells

For the tandem devices, the processing of individual layers followed the same protocols as those used for single perovskite and single OSCs, as detailed in Section 2.4. and Section 2.5. The general device architecture is illustrated in Figure 7. Unlike the single cells, where layers were patterned using a cotton swab soaked in solvent, all layers in the tandem were scraped 5 nm from all edges of the substrate with a scalpel after spin-coating the PDIN layer. Specific evaporation masks were employed for the deposition of the Ag RL (Figure 8a), MoO_x (Figure 8b) and the 100 nm Ag top contact (Figure 8c).

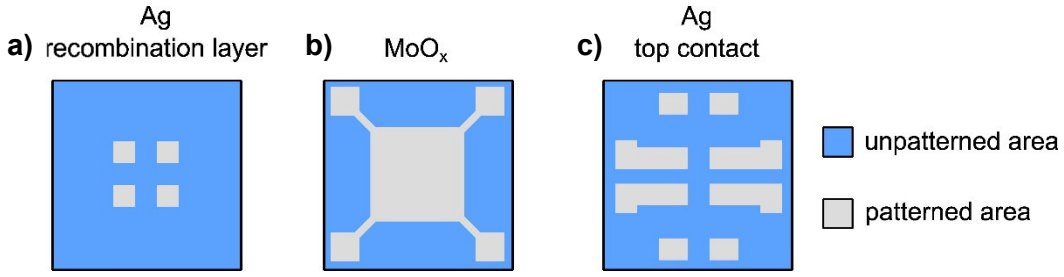

Figure 8. Outline of the evaporation masks used for TSC fabrication with a) mask for the Ag recombination layer b) mask for the MoO_x layer c) mask for the Ag top contact.

2.6.1. Testing MoO_x as a protection layer in the interconnecting layer

To evaluate the effect of a MoO_x protection layer on the perovskite subcell, 5 nm Ag was deposited on PCBM/BCP. Subsequently, either 10 nm of MoO_x or no MoO_x was evaporated onto the Ag layer. The remainder of the organic subcell was processed according to the procedure in Section 2.5. using Solar 3 with 1 vol% TritonX-100 in IPA post-treatment.

2.6.2. Recombination layer thickness optimization

The influence of the Ag RL thickness was tested by evaporating 0, 1, 2, 5 nm Ag onto PCBM/BCP. A 10 nm MoO_x layer was inserted between the RL and the Solar 3 with TritonX-100 post-treatment.

2.6.3. Hole transport layer variation

Different HTLs were tested for the organic sub cell in a tandem device. Three different PEDOT variations and one control group without PEDOT were examined and processed on both 10 nm and 20 nm MoO_x layers. The tested PEDOT variations included:

- PEDOT:PSS suspension in water (Al4083)
- IPA diluted PEDOT:PSS Al4083 (dil. Al4083)
- Solar 3 with TritonX-100 post-treatment (Solar 3)

For the diluted Al4083, a 1:3 ratio (Al4083:IPA) was used IPA was added dropwise to Al4083 while stirring vigorously for 5 minutes to prevent precipitation of PEDOD:PSS. The processing of diluted Al4083 followed the same steps as undiluted Al4083, as described in Section 2.5. , resulting in a film thickness of 20 nm on glass.

2.7. Current density-voltage measurements

Current density-voltage measurements denoted as *J*(V) were conducted employing a LOT-QD solar simulator (LS0821). The devices underwent AM1.5G irradiation, generated by a xenon arc-discharge lamp, which was calibrated using a reference silicon solar cell (Si-01 TC, Mencke & Tegtmeyer). For single absorber cells, both forward and backward scans were executed in a range of -0.5 to 1.5, with a step increment of 0.05 V. For the TSCs the range was -0.5 to 2.5 with a step of 0.1 V. For the dark characteristic of the cells, measurements were conducted in darkness within the voltage range of -1.5 to 1.5 V, employing a step increment of 0.05 V. A source meter (Keithley 2401-LV) was utilized to measure the current density at each voltage.

2.8. External quantum efficiency

For the external quantum efficiency (EQE) measurements, the light of a xenon arc-discharge lamp (Oriel instruments) passed a mechanical chopper with a frequency of 173 Hz, and a wavelength was selected using a grating monochromator (Corner Stone 130 1/8 m). The beam was focused by a lens and directed on the cell. The current output at each wavelength was converted into a voltage and amplified using a potentiostat (1002 T-NC, Jaissle). Both the chopper wheel and the potentiostat were linked to a Lock-in amplifier (Model SR830, Stanford Research Systems) to modulate the signal, significantly enhancing measurement sensitivity. To correct for the spectrum of the xenon arc-discharge lamp, a silicon photodiode (S2281, Hamamatsu) was employed. EQE measurements were performed across a spectral range spanning from 350 to 1000 nm with a wavelength increment of 10 nm. The measured signal was converted into the external quantum efficiency according to Equation 1:

$$\mathrm{EQE}(\lambda)=\frac{S_{\mathrm{Cell}}\times R_{\mathrm{Si}}}{S_{\mathrm{Si}}}\times\frac{\mathrm{h}\times\mathrm{c}}{\lambda\times\mathrm{e}} \tag{1}$$

The signals measured from the solar cell and the silicon reference diode are denoted as S_{cell} and S_{Si}, respectively, while R_{Si} represents the established spectral responsivity of the reference silicon diode. The symbols h, c, λ, and e represent the Planck constant, speed of light, wavelength, and elementary charge, respectively. The short circuit current density (J_{SC}) is calculated by integrating the product of the EQE and the photon flux (Φ) of the AM1.5G solar spectrum over the wavelength, following Equation 2.

$$J_{\mathrm{SC}}=\mathrm{e}\times\int \mathrm{EQE}(\lambda)\times\Phi(\lambda)\,\mathrm{d}\lambda \tag{2}$$

2.9. UV-VIS spectroscopy

UV-Vis spectroscopy was conducted using the double-beam spectrometer Lambda 1050 (Perkin Elmer) to analyze the transmittance and reflectance of perovskite and PTB7-Th:IEICO-4F thin films. Four different perovskite films were investigated on glass/MeO-2PACz substrates: without

additive and post-treatment, 3 mg mL^{-1} MACl additive, 0.25 mg mL^{-1} PEAI post-treatment, and the combination of additive and treatment. PTB7-Th films (6 mg mL^{-1} D + 9 mg mL^{-1} PS in CB), IEICO-4F films (9 mg mL^{-1} A + 6 mg mL^{-1} PS in CB), and PTB7-Th:IEICO-4F films (6 mg mL^{-1} D + 9 mg mL^{-1} A in CB) were processed directly on glass. An InGaAs detector was used, while the light source consisted of both tungsten and deuterium lamps. The wavelength range examined spanned from 350 to 1000 nm. Reflectance measurements were performed with a 45° reflection unit installed, using polished silicon wafers and an Ag mirror as reference materials. The absorptance (A) of the films was derived by employing Equation 3, which involves the transmittance (T) and reflectance (R) values.

$$A = 1 - T - R \tag{3}$$

Additionally, utilizing the thickness measurements of the films obtained with a Dektak Profilometer, Equation 4 enables the calculation of the absorption coefficient.

$$\alpha = \frac{1}{d} \times \ln\left(1+\frac{A}{T}\right) \tag{4}$$

The optical band gap of the material can be determined using the Tauc plot method. Thereby, the product of the absorption coefficient and the photon energy (in eV) squared is plotted against the photon energy. The intercept of an extrapolated linear fit of the curve with the x-axis represents the band gap.

2.10. Photoluminescence and electroluminescence measurements

2.10.1. Photoluminescence measurements of films

The photoluminescence (PL) of the perovskite and organic absorber films was assessed using the following configuration: Laser light at a wavelength of 405 nm (Coherent Obis) with a power output of 2.83 mW served as the excitation source. The emitted light was guided through a glass fiber, subsequently passing through two 420 nm long-pass filters before being directed through a monochromator (Shamrock 303i, Andor Technology). Detection was accomplished using a charge-coupled device sensor (iDus 420, Andor Technology). For the time-dependent measurements, a steady-state PL spectrum was recorded every minute for 9 minutes in total. Four different perovskite films processed on glass/MeO-2PACz were investigated: without additive and post-treatment, 3 mg mL^{-1} MACl additive, 0.25 mg mL^{-1} PEAI post-treatment and the combination of additive and treatment. PTB7-Th films (6 mg mL^{-1} D + 9 mg mL^{-1} PS in CB), IEICO-4F films (9 mg mL^{-1} A + 6 mg mL^{-1} PS in CB) and PTB7-Th:IEICO-4F films (6 mg mL^{-1} D + 9 mg mL^{-1} A in CB) were processed directly on glass.

2.10.2. Time-dependent photoluminescence/electroluminescence and open circuit voltage measurements of cells

A time-dependent PL measurement on a WBG PSC (3 mg mL^{-1} MACL additive, 0.25 mg mL^{-1} PEAI post-treatment) was conducted. Simultaneously, the open circuit voltage of the cell was recorded. Laser light at a wavelength of 488 nm (Coherent Obis, 3 mW) served as the excitation source. The emitted light was guided through a glass fiber, subsequently passing through two 420 nm long-pass filters before being directed through a monochromator (Shamrock 303i, Andor Technology). Detection was accomplished using a charge-coupled device sensor (iDus 420, Andor Technology). The open circuit voltage was measured by a source meter (Keithly 2400). A simultaneous start of the PL and V_{OC} was ensured by a shutter connected to a custom-made program from Rene Zahrhuber BSc. Reference measurements of a pure iodide perovskite with the device architecture ITO/PEDOT:PSS(PH1000)/$Cs_{0.12}MA_{0.88}/PbI_3$/PCBM/TiO_x/Al were also provided by Rene Zahrhuber BSc. Furthermore, electroluminescence (EL) was conducted by applying 2 mA current (Keithley 2400) and measured analogous to the PL.

2.11. Atomic force microscopy

An atomic force microscope (AFM, Bruker Innova) was used to study the surface of perovskite films and a PTB7-Th:IEICO-4F film. The following films were studied: without additive and post-treatment, 3 mg mL^{-1} MACl additive, 0.25 mg mL^{-1} PEAI post-treatment, and the combination of additive and treatment processed on glass MeO-2PACz. The PTB7-Th:IEICO-4F film (6 mg mL^{-1} D + 9 mg mL^{-1} A in CB) was processed directly on glass. An area of 10 x 10 µm was probed in tapping mode with a scan rate of 10 µm s^{-1} and 1024 samples per line.

2.12. Film thickness measurement

All the thickness parameters in this thesis were obtained using a Bruker Dektak XT profilometer.

3. Results and discussion

The objective of this thesis is to develop an efficient ICL for a perovskite organic TSC. First, the perovskite front subcell and the organic rear subcell are individually optimized and characterized. The perovskite cell with the composition $FA_{0.8}Cs_{0.2}Pb(I_{0.5}Br_{0.5})_3$ is optimized by varying the antisolvent dripping time and by testing an additive (MACl) and a post-treatment with PEAI. Completed cells undergo *J*(V) and EQE measurements, and the solvent and temperature stability are evaluated. Optical, PL, and AFM measurements provide insight into the band gap, the surface roughness, the particle size, and phase segregation. Variations of the ETL, including the addition of PMMA to PCBM and replacing BCP with TiO_x, are examined. For the organic rear subcell, a PEDOT-based HTL suspended in toluene is optimized through different post-treatments and tested on a model cell with a P3HT:PCBM active layer. Subsequently, the fabrication of OSCs with a PTB7-Th:IEICO-4F active layer includes detailed analysis through optical, PL, and AFM measurements. Finally, the optimized subcells are integrated into a monolithic tandem device. A RL based on silver with varying thicknesses is evaluated. Additionally, the HTL of the ICL is also varied, and potential errors and flaws of the device are discussed.

3.1. Wide band gap perovskite solar cells

3.1.1. Antisolvent timing

Timing the exact moment to apply the antisolvent during the spin-coating process, known as antisolvent dripping time, is crucial for the device performance. Upon initiating the spin-coating program DMF and NMP in the perovskite precursor evaporate, leading to a state of near supersaturation. At this moment antisolvent dripping is ideal, promoting the formation of a compact and homogeneous film[86,87]. Premature antisolvent dripping results in excessive removal of the precursor solution, while in delayed dripping, heterogeneous nucleation has already started, rendering the antisolvent useless[86,87]. Figure 9 and Table 5 present the results of cells with two distinct antisolvent dripping times after initiating the spin-coating program. Based on prior findings, optimal results with this perovskite recipe were achieved when the antisolvent was dripped 22 seconds after the start of the spin-coating program[24]. However, in this study, only a reduced dripping time of 17 seconds after start achieves comparable results. This adjustment correlates with an increase in V_{OC} by 0.05 V to 1.15 V, a rise in J_{SC} by 0.05 mA cm^{-2}, to 15.3 mA cm^{-2} and a boost in PCE by 1.2 % to 11.5 % compared to a dripping time of 22 seconds. The timing may vary due to several factors, including the preparation and stirring of the precursor solution, conditions within the glove box concerning atmosphere and temperature, and procedural nuances among operators. This variability underscores the sensitivity of antisolvent dripping time, where even minor deviation can exert a significant influence on the device performance.

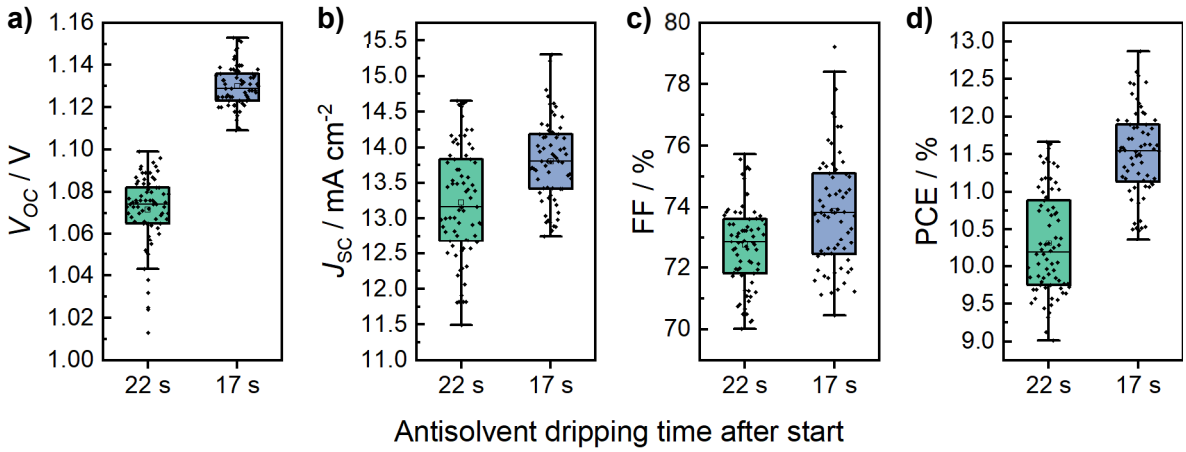

Figure 9. Box plot diagrams with PV parameters extracted from *J*(V) curves of WBG PSCs with two distinct times to apply the antisolvent after start of the spin-coating program **a)** V_{OC}, **b)** J_{SC}, **c)** FF, **d)** PCE.

Table 5. PV parameters extracted from *J*(V) curves of WBG PSCs with two distinct times to apply the antisolvent after start of the spin-coating program.

Dripping time / s	Scan direction	V_{OC} / V	J_{SC} / mA cm^{-2}	FF / %	PCE / %	N
17	rvs	1.10 (1.07 ± 0.02)	14.7 (13.2 ± 0.8)	76 (73 ± 1)	11.7 (10.3 ± 0.7)	74
22	rvs	1.15 (1.13 ± 0.01)	15.3 (13.7 ± 0.7)	79 (74 ± 2)	12.9 (11.5 ± 0.7)	69

3.1.2. Additive engineering

In Figure 10 and Table 6, the effect of additive engineering with MACl and post-treatment with PEAI is depicted. The effects of additives and post-treatments have been previously discussed in Section 1.2.2. The addition of MACl shows a significant enhancement in cell performance, especially in the J_{SC}. Upon adding 3 mg mL^{-1} MACl to the perovskite precursor solution, a notable increase of 0.5 mA cm^{-2} to 14.2 mA cm^{-2} is observed compared to cells without additive. This enhancement can be attributed to preferential vertical crystal growth, resulting in large crystal grains that improve charge transport properties[39,41,45]. Additionally, a slight increase in V_{OC} of 0.02 V is observed possible due to minimized grain boundaries. Cells with 3 mg mL^{-1} MACl perform marginally better than those with 2 mg mL^{-1}, thus, this concentration was selected for further optimization and application in a TSC.

Post-treatment with PEAI results in an increase in V_{OC} attributed to defect passivation at the perovskite surface discussed in Section 1.2.2. Reduced defect density leads to lower non-radiative recombination enhancing the V_{OC} from 1.13 V in untreated cells to 1.19 V with the post-treatment. To confirm that this increase is not solely due to the solvent IPA of the PEAI solution, reference cells treated with pure IPA have been fabricated. Indeed, these cells show similar performance to untreated cells, indicating negligible impact from the solvent. Nevertheless, an increase in J_{SC} from

13.7 mA cm^{-2} without treatment to 13.9 mA cm^{-2} is noted. Drawing from previous research, a comparable enhancement is observed with PEAI treatment, suggesting potential surface morphology modification induced by the solvent[43].

The combination of MACl addition and PEAI post-treatment yields the best results in this study, with an average PCE of 13.9 % (V_{OC} = 1.22 V, J_{SC} = 14.7 mA cm^{-2}, FF = 77 %) compared to 11.5 % (V_{OC} = 1.13 V, J_{SC} = 13.7 mA cm^{-2}, FF = 74) without additive and/or treatment. The champion cell reached an efficiency of 15.1 % with a V_{OC} of 1.22, J_{SC} of 15.8 mA cm^{-2} and an FF of 78 %. Synergistic effects are apparent, as evidenced by a V_{OC} increase of 0.11 V, which cannot be solely explained by the individual enhancements from MACl addition (+0.02 V) and PEAI treatment (+0.06 V). A similar trend is observable with the J_{SC}.

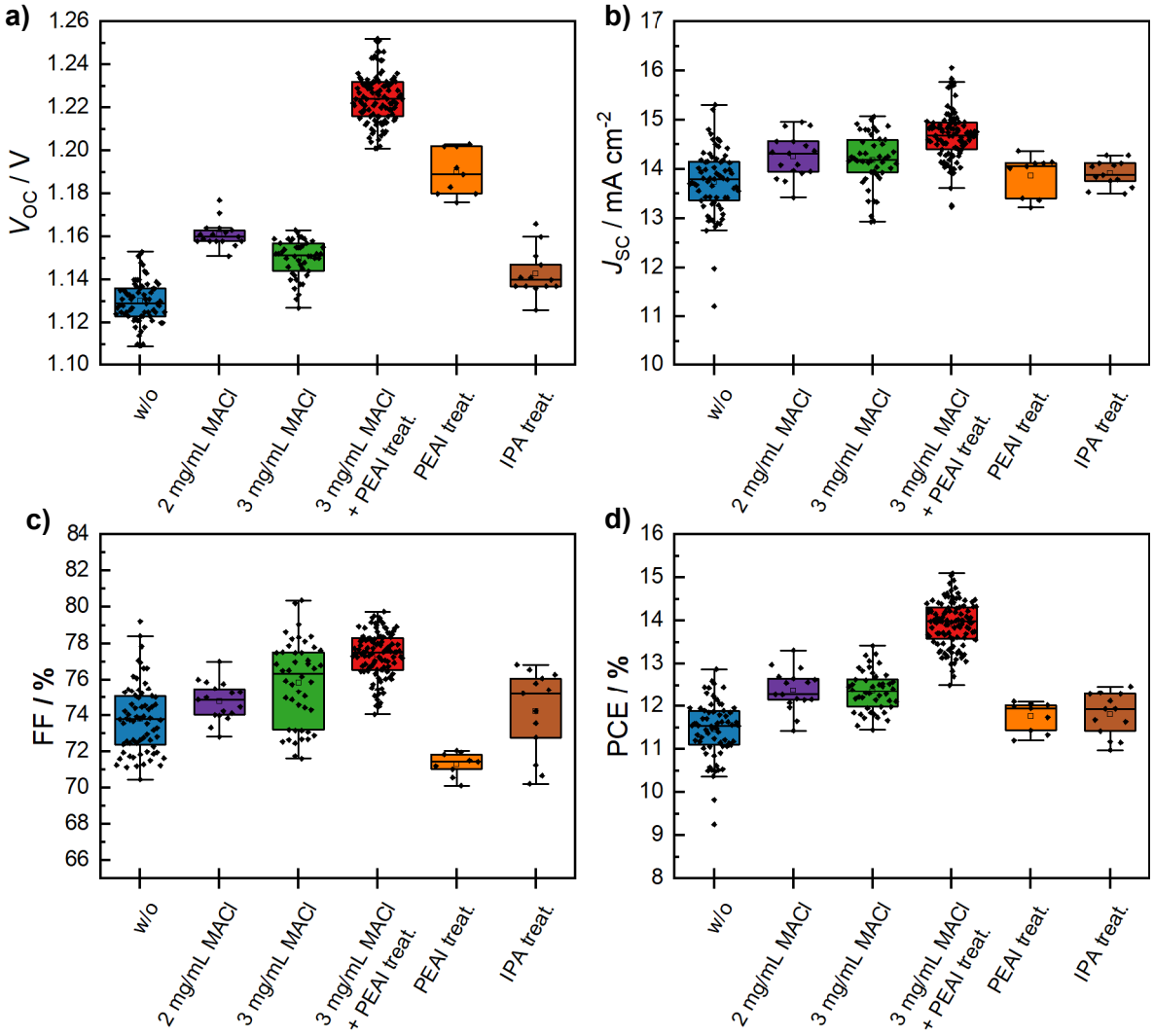

Figure 10. Box plot diagram of the PV parameters extracted from *J*(V) curves of the WBG PSC performance using 2 and 3 mg mL^{-1} MACl as an additive, 0.25 mg mL^{-1} PEAI solution in IPA as post-treatment (IPA treat.), combination of additive (3 mg mL MACL) and 0.25 mg mL^{-1} PEAI post-treatment, IPA post-treatment for reference and cells without additive or treatment (w/o). With the parameters **a)** V_{OC}, **b)** J_{SC}, **c)** FF, **d)** PCE.

Table 6. WBG PSC performance using 2 and 3 mg mL^{-1} MACl as an additive, 0.25 mg mL^{-1} PEAI solution in IPA as post-treatment (treat.), combination of additive (3 mg mL MACL) and 0.25 mg mL^{-1} PEAI post-treatment, IPA post-treatment for reference and cells without additive or treatment (w/o).

Additive/ treatment	Scan direction	V_{OC} / V	J_{SC} / mA cm^{-2}	FF / %	PCE / %	N
w/o	fwd	1.16 (1.13 ± 0.01)	15.2 (13.7 ± 0.6)	79 (74 ± 2)	12.6 (11.3 ± 0.6)	70
	rvs	1.15 (1.13 ± 0.01)	15.3 (13.7 ± 0.7)	79 (74 ± 2)	12.9 (11.5 ± 0.7)	69
2 mg mL^{-1} MACl	fwd	1.19 (1.14 ± 0.01)	14.9 (14.2 ± 0.4)	77 (75 ± 2)	13.1 (12.2 ± 0.5)	18
	rvs	1.18 (1.16 ± 0.01)	15.0 (14.3 ± 0.4)	77 (75 ± 1)	13.3 (12.4 ± 0.5)	17
3 mg mL^{-1} MACl	fwd	1.17 (1.14 ± 0.01)	15.0 (14.1 ± 0.5)	80 (76 ± 2)	13.2 (12.2 ± 0.5)	46
	rvs	1.16 (1.15 ± 0.01)	15.1 (14.2 ± 0.5)	80 (76 ± 2)	13.4 (12.4 ± 0.5)	46
3 mg mL^{-1}MACl + PEAI treatment	fwd	1.25 (1.22 ± 0.01)	16.0 (14.7 ± 0.5)	80 (78 ± 1)	15.0 (13.9 ± 0.6)	110
	rvs	1.25 (1.22 ± 0.01)	16.1 (14.7 ± 0.5)	80 (77 ± 1)	15.1 (13.9 ± 0.5)	110
PEAI treatment	fwd	1.20 (1.17 ± 0.02)	14.3 (13.9 ± 0.5)	72 (71 ± 1)	11.8 (11.5 ± 0.2)	9
	rvs	1.20 (1.19 ± 0.01)	14.4 (13.9 ± 0.4)	72 (71 ± 1)	12.1 (11.8 ± 0.3)	9
IPA treatment	fwd	1.13 (1.12 ± 0.01)	14.3 (13.9 ± 0.3)	77 (74 ± 2)	12.2 (11.5 ± 0.5)	13
	rvs	1.17 (1.14 ± 0.01)	14.3 (13.9 ± 0.3)	77 (74 ± 2)	12.5 (11.8 ± 0.5)	13

Figure 11a displays representative *J*(V) curves of the WBG PSCs with the different additives and/or treatments at 100 mW cm^{-2} illumination. The plot illustrates the increase in V_{OC} by PEAI, the increase in J_{SC} due to MACl, and the best-performing cell with both additive and treatment. Additionally, some degree of hysteresis is observed, which is a typical effect in PSCs, characterized by the deviation of *J*(V) curves between the forward (negative to positive potential) and reverse (positive to negative potential) scan directions. The underlying causes of hysteresis are complex and not yet fully understood but are likely due to a combination of mechanisms such as polarization[88], ion migration[89,90], and carrier accumulation at the interfaces[91]. Despite the presence of hysteresis in all cells, the degree is minimal, indicating the generally high quality of the perovskite film and the interlayers.

Figure 11b depicts the semilogarithmic *J*(V) curves measured in darkness, from which the dark leakage current density (J_{leak}) at ~-0.5 V can be extracted. This undesired current, which flows in the opposite direction to the photocurrent, reduces the J_{SC} [92]. Dark leakage current also serves as an indicator of non-radiative recombination and interface-induced recombination, reflecting the

quality of the interfaces and the perovskite film[43,92]. The leakage current (at -0.5 V) is low for all cells, but slightly higher for the w/o ($7.3 \cdot 10^{-4}$ mA cm^{-2}) and the MACl cells ($6.2 \cdot 10^{-4}$ mA cm^{-2}), compared to PEAI cells ($2.5 \cdot 10^{-4}$ mA cm^{-2}) and MACl + PEAI cells ($1.8 \cdot 10^{-4}$ mA cm^{-2}), demonstrating the effectiveness of the treatments.

Figure 11c presents the EQE measurement of the WBG PSCs. All cells exhibit similar EQE shapes with high efficiency at short wavelengths (350 to 520 nm) ranging from 70 to 83 %. A local minimum efficiency below 68 % occurs at 570 nm. Beyond 680 nm, the EQE drops to zero as the band gap is reached. The efficiency of the MACl addition and PEAI-treated cells is uniformly higher across the entire wavelength region, supporting the hypothesis that these additives enhance film quality and reduce non-radiative recombination, enabling more charge carriers to be collected at the electrodes. J_{SC} values derived through the EQE measurement (13.9 mA cm^{-2} for MACl + PEAI) are slightly lower than those obtained from J(V) measurements (14.4 mA cm^{-2}). This difference is likely due to variations in the light spectrum of the solar simulator and measurement errors in determining the device area using a caliper gauge.

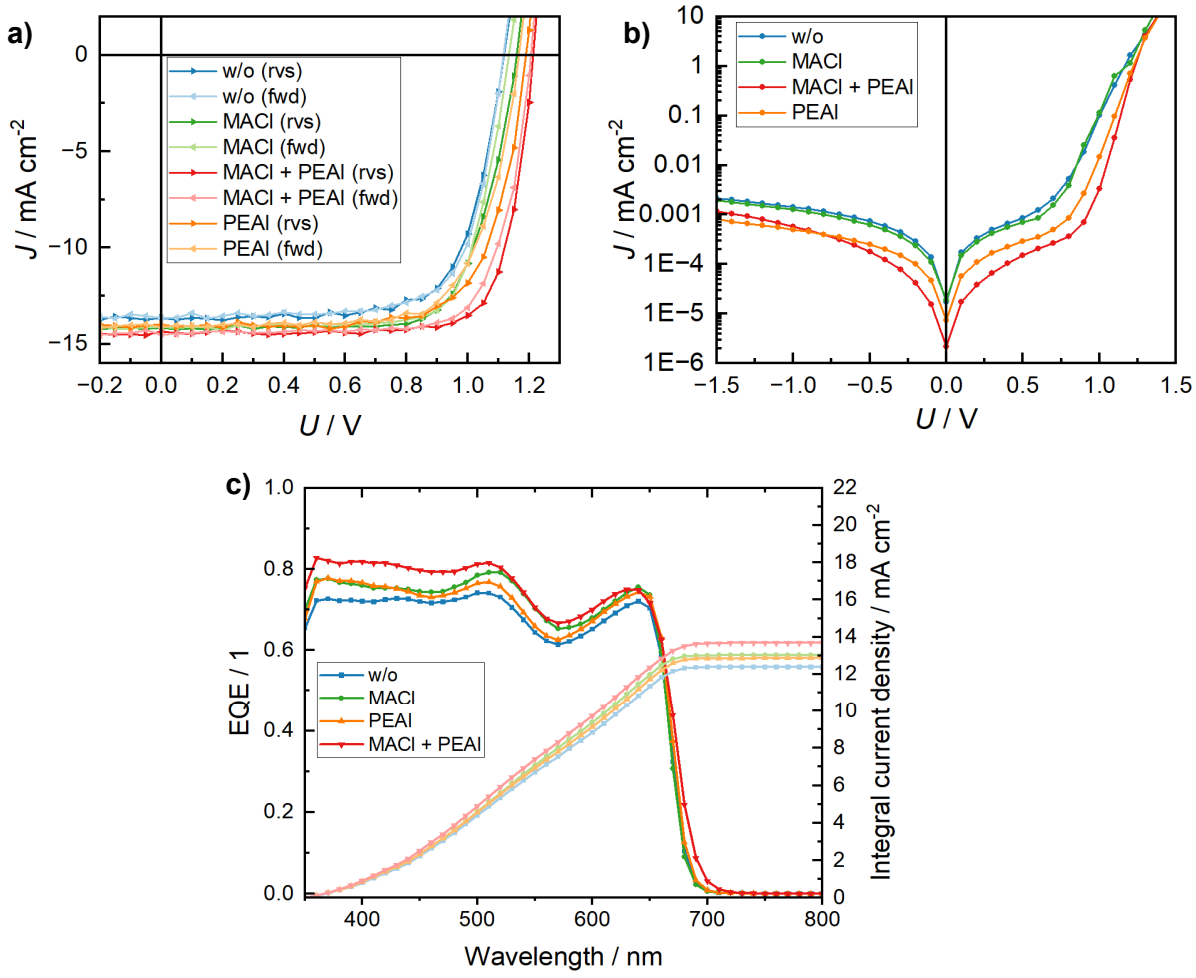

Figure 11. Optoelectrical measurements of WBG PSC without any additive/treatment (w/o), with 3 mg mL^{-1} MACl additive (MACl), with 0.25 mg mL^{-1} PEAI in IPA post-treatment (PEAI) and a combination of MACl additive and PEAI post-treatment (MACl + PEAI) with **a)** semilogarithmic dark J(V) curves **b)** illuminated J(V) curves (100 mW cm^{-2}) and **c)** external quantum efficiency measurements with light colors representing integrated current density.

3.1.3. Atomic force microscopy

Figure 12 presents the tapping amplitude AFM images of WBG perovskite films on glass/MeO-2PACz. In the image without additive and/or treatment (Figure 12a), the grains are the smallest, with an average diameter (D_a) of 0.32 µm and exhibit a diamond shape. The effect of MACl additive on the crystallization dynamic is evident since the grain size is larger (D_a = 0.54 µm), more rounded, and has less distinct boundaries. The PEAI post-treatment (Figure 12c) results in a similar grain size to the untreated film (D_a = 0.34 µm), with the grains retaining their diamond shape. When both the MACl additive and the PEAI post-treatment are applied (Figure 12d), the film morphology combines the characteristics, with larger grains (D_a = 0.39 µm) but is still diamond shaped. The observed grain sizes for perovskite films with the same composition are about 3 to 5 times larger than those reported in literature (D_a = 0.105 µm)[77]. This discrepancy could be attributed to the different HTL on which the perovskite films are processed.

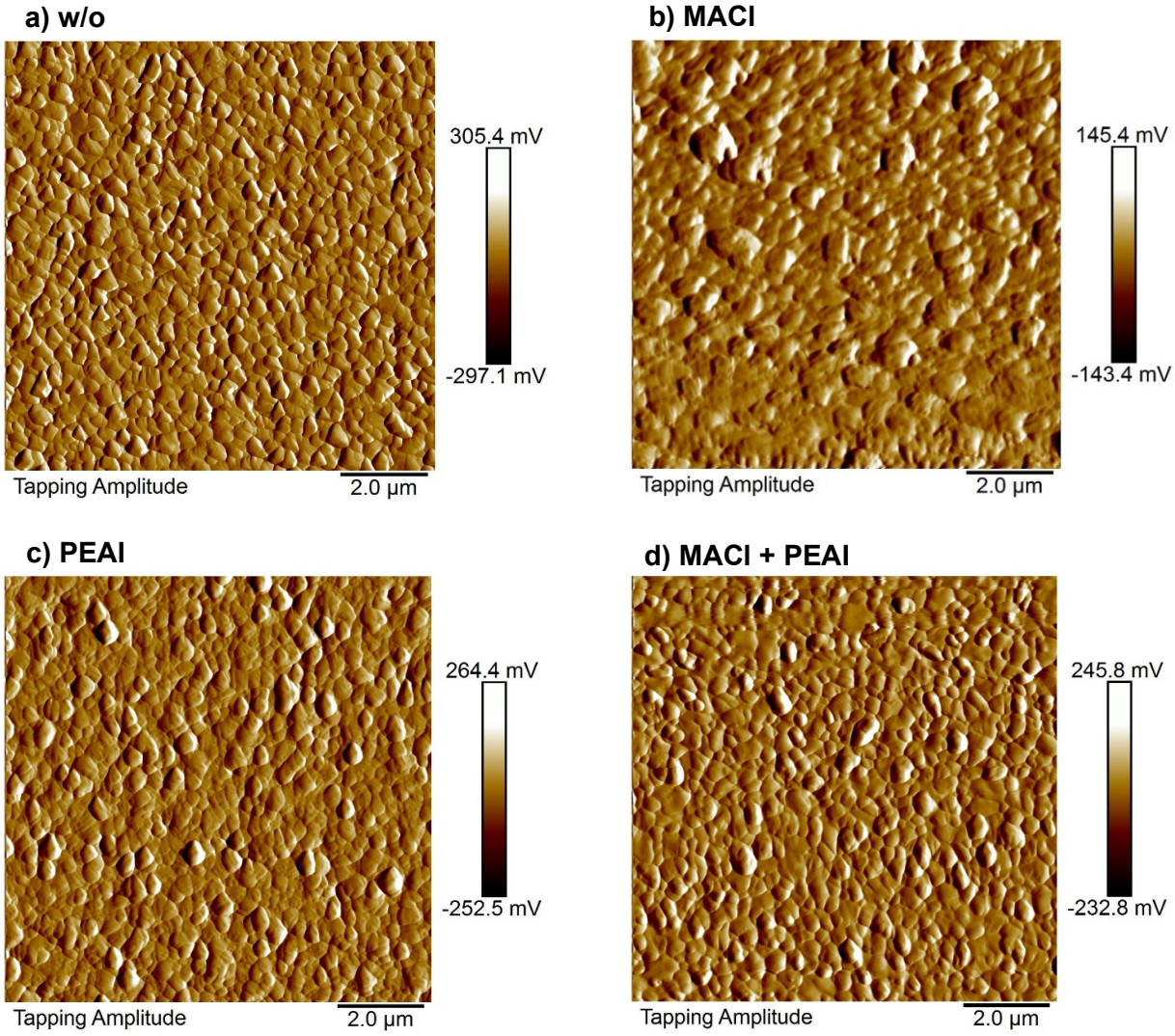

Figure 12. Tapping amplitude atomic force spectroscopy images of WBG perovskite films on glass/MeO-2PACz with **a)** without additive/treatment (w/o) **b)** 3 mg mL^{-1} MACl additive (MACl) **c)** 0.25 mg mL^{-1} PEAI post-treatment (PEAI) **d)** 3 mg mL^{-1} MACl additive and 0.25 mg mL^{-1} PEAI post-treatment (MACl + PEAI).

In Figure 13, the height profiles of the films are shown.The root mean square roughness (R_q) (Table 7) is similar across all films, ranging from 10.9 - 13.0 nm. Although PEAI is expected to be deposited at the grain boundaries, thereby reducing roughness, this study does not confirm that effect[42]. The PEAI-treated film exhibits the highest R_q of 13.0 nm and a peak-to-valley roughness (R_z) of 140 nm, indicating high surface spikes. Wang et al. reported R_q values around 16 nm for similar compositions[77]. High roughness can be beneficial for light management by reducing parasitic absorption and enhancing interface charge transport, due to the increased interface area[93]. However, it also raises the defect density potentially reducing V_{OC}. In the context of TSCs, where various layers are processed atop of the front subcell, excessive roughness can pose problems. If the ETL cannot cover the surface spikes of the perovskite layer adequately, it may compromise the quality and performance of subsequent layers. Thus smooth surfaces are crucial for maximizing device performance in TSCs.

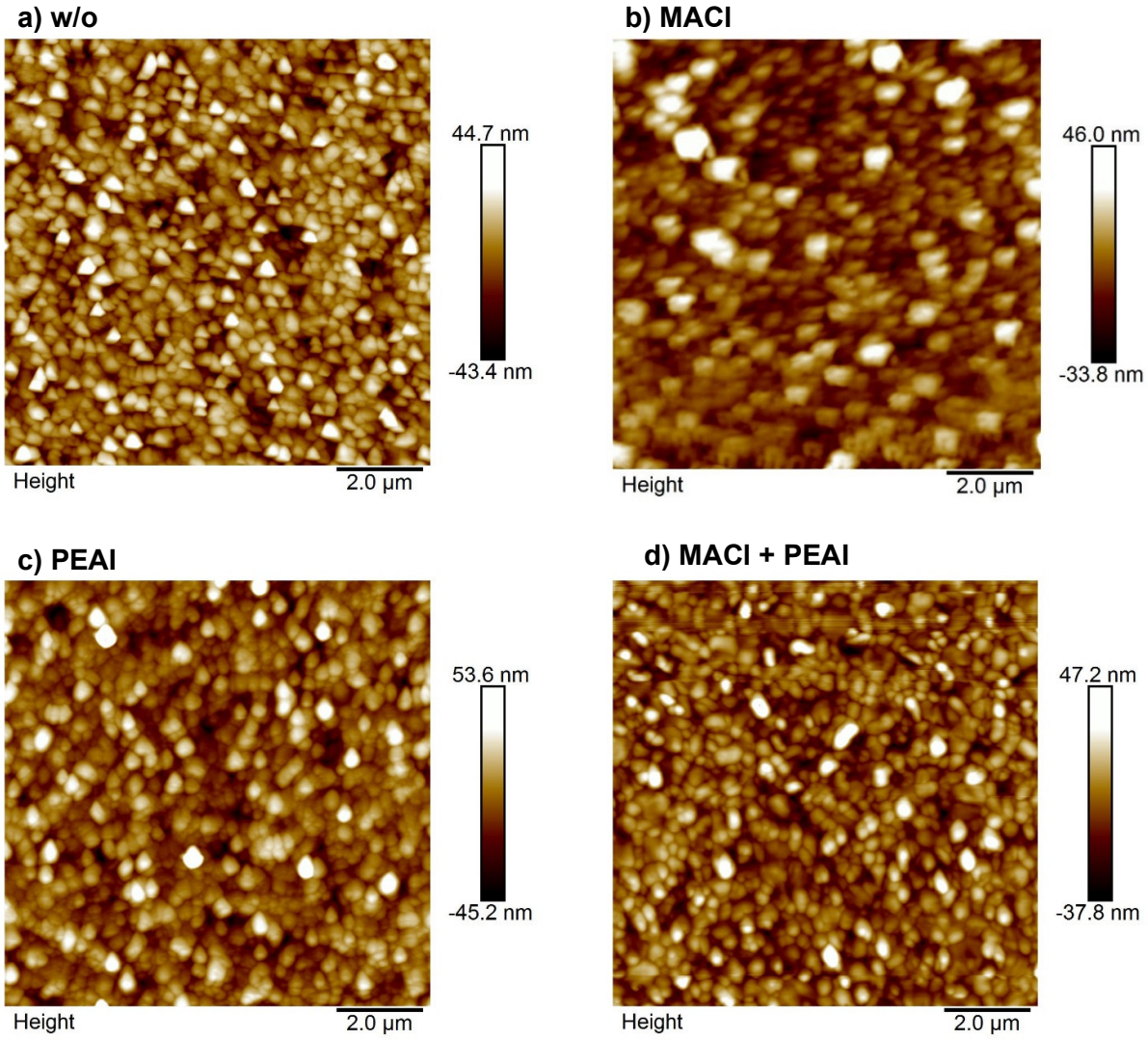

Figure 13. Height profile atomic force spectroscopy images of WBG perovskite films on glass/MeO-2PACz with **a)** without additive/ treatment (w/o) **b)** 3 mg mL^{-1} MACl additive (MACl) **c)** 0.25 mg mL^{-1} PEAI post-treatment (PEAI) **d)** 3 mg mL^{-1} MACl additive and 0.25 mg mL^{-1} PEAI post-treatment (MACl + PEAI).

Table 7. Surface roughness parameters were calculated from AFM images with average roughness (R_a), root mean square roughness (R_q) and peak-to-valley height (R_z).

Additive/treament	R_a / nm	R_q / nm	R_z / nm
w/o	9.4	12.0	104
MACl	8.2	10.9	98
PEAI	9.9	13.0	140
MACl + PEAI	8.4	11.0	100

3.1.4. Optical measurements

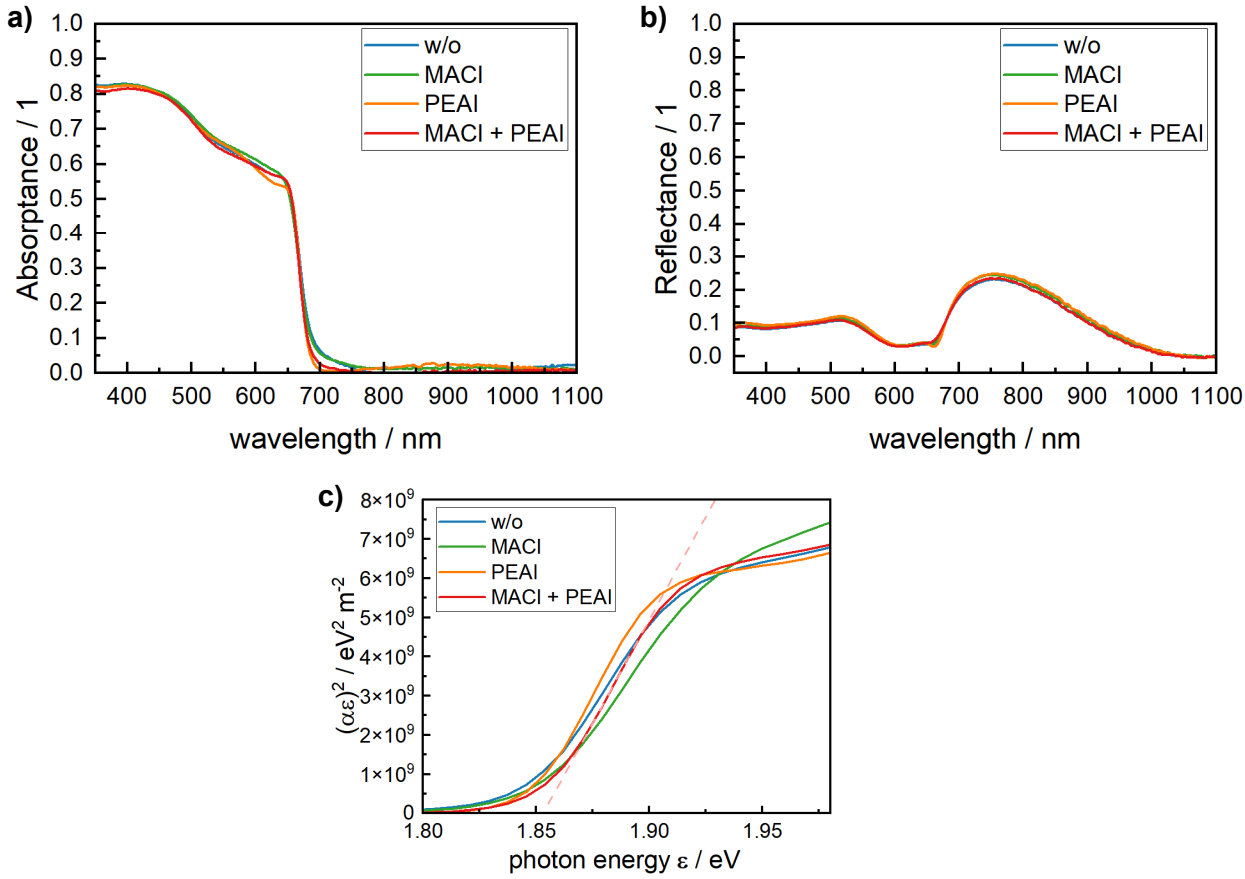

Figure 14. Optical measurements of WBG perovskite films processed on glass/MeO-2PACz with 3 mg mL^{-1} MACl additive (MACl), 0.25 mg mL^{-1} PEAI in IPA post-treatment (PEAI), a combination of both (MACl + PEAI) and without treatment/additive (w/o) with **a)** absorptance **b)** reflectance and **c)** Tauc plot.

Figure 14a and b show the absorptance and reflectance spectra of the WBG perovskite films in the range of 350 - 1100 nm. The highest absorption, approximately 82 %, occurs at 400 nm. The addition of MACl, the PEAI treatment, and their combination cause minimal changes in the absorption behavior. This is expected, as these treatments primarily alter film morphology and passivate defects without affecting the band gap. The exact determination of the band gap is provided by the Tauc method. This involves plotting the absorption coefficient times the photon energy squared against the photon energy. A linear fit is applied to the resulting curve just before the band gap and extrapolated. The intersection of this linear fit with the x-axis represents the

band gap. Table 8 summarizes the band gap of all fabricated and measured perovskite films, showing values at 1.84 - 1.85 eV. This confirms that the additive and PEAI treatment do not influence the band gap but rather enhance charge transport properties and defect passivation, reducing non-radiative recombination.

Table 8. Band gap of perovskite films processed on glass/MeO-2PACz with 3 mg mL^{-1} MACl additive (MACl), 0.25 mg mL^{-1} PEAI in IPA post-treatment (PEAI), a combination of both (MACl + PEAI) and without treatment/additive (w/o).

Film	Band gap / eV
w/o	1.84
MACl	1.85
PEAI	1.84
MACl + PEAI	1.84

3.1.5. Photoluminescence measurements

Steady-state photoluminescence is a useful method for qualitatively analyze the defect density within the perovskite. A low number of defect states significantly reduces the probability of non-radiative recombination of charge carriers, thereby enhancing the probability of radiative recombination, thus increase the PL intensity[81,94]. The steady-state PL spectra shown in Figure 15 indicate that PL emission at 670 nm is enhanced by approximately 2.7 times through PEAI surface passivation, effectively reducing defects at the surface. While the addition of MACl increases the grain size, leading to fewer grain boundaries and defects[95], it does not impact PL intensity. It remains nearly the same as without the additive. This observation aligns with data from *J*(V) curves, which suggest that MACl addition primarily increases the J_{SC} but does not significantly influence the V_{OC}. The combination of MACl additive and PEAI treatment has a greater impact on PL intensity than PEAI alone, confirming the synergistic effect of the two methods.

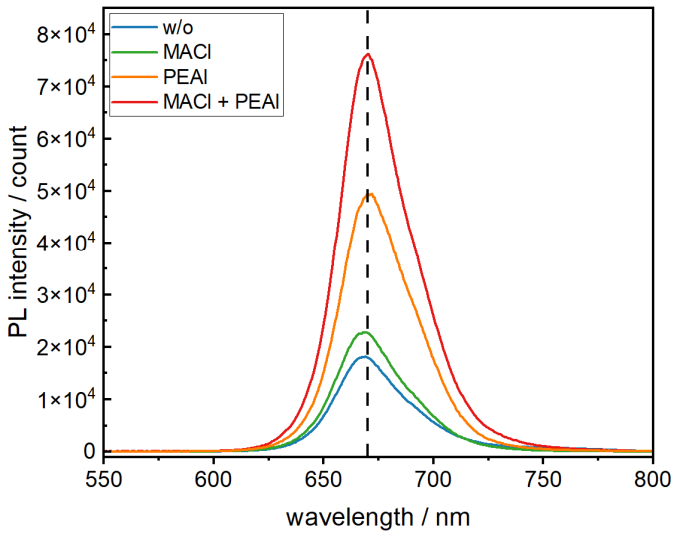

Figure 15. Steady-state PL measurements of WBG perovskite films on glass/MeO-2PACz excited with a 405 nm laser light with a power of 2.35 mW, 1 s exposure time and 100 µm slit width.

In Figure 16., the development of the PL signal over 9 minutes can be seen. In all films phase segregation is observable and a second PL peak at around 775 nm is distinct after at least 3 minutes. After 9 minutes the intensity of this second peak matched or exceeded the intensity of the original peak at 670 nm. This is a clear indication that an iodine-rich phase forms with a narrow band gap. The relative intensity of the second peak is greatly enhanced by the PEAI post-treatment. This enhancement may be attributed to the reduction in trap state density, which increases the PL intensity of both the mixed halide phase as well as the segregated iodine-rich perovskite phase. In previous studies, the HTL MeO-2PACz significantly slowed down light-induced halide segregation, with a second PL peak appearing only after 30 minutes of illumination[15]. This differs from the results shown in this study, where a second peak emerged much earlier.

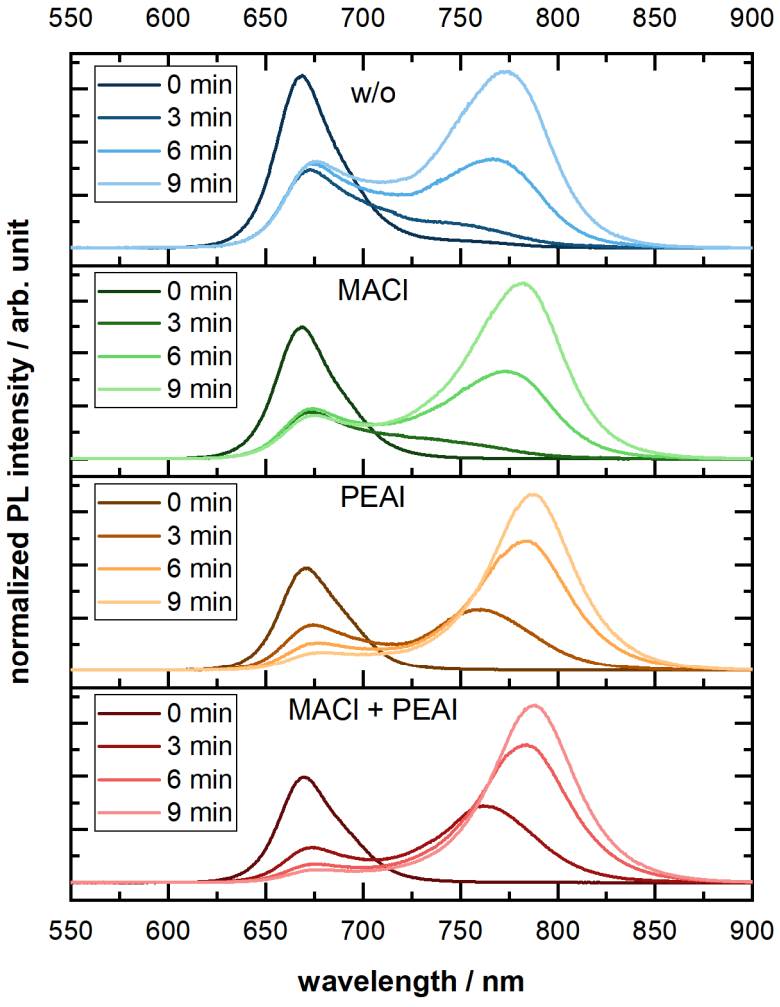

Figure 16. Time-dependent development of steady-state PL signals of WBG perovskite films on glass/MeO-2PACz excited with a 405 nm laser light with a power of 2.35 mW, 1 s exposure time, and 100 µm slit width.

Simultaneous measurement of PL and the V_{OC} provides deeper insights into the impact of phase segregation on the device. Figure 17a presents the results of such an experiment, noting that the initial peak shifted from 670 nm in the films to 675 nm in the finished cell, probably due to the

additional layers. The graph can be divided into two sections: during the first 90 seconds, the initial PL peak doubles in intensity, with no noticeable phase segregation. Meanwhile, the V_{OC} follows an exponential decrease from 1.26 V to 1.21 V (reduction by 50 mV). From 90 seconds to 15 minutes, both the 675 nm PL peak and V_{OC} decrease linearly (down to 1.19 V). The PL peak (775 nm) of a phase-segregated I-rich phase emerges and increases linearly, at the same time. The initial V_{OC} reduction in the first 90 seconds is unlikely due to light-induced phase segregation, as there is minimal PL emission at 775 nm. Equivalent measurements on pure iodide $Cs_{0.12}Ma_{0.88}PbI_3$ show a similar trend of the V_{OC} (Figure 17d). After an initial sudden increase of the V_{OC} to 1.10 V, it decreases exponentially in 5 minutes to 1.01 V (reduction by 90 mV), in parallel with an exponential decrease of the PL emission. In a pure iodine perovskite this V_{OC} decrease cannot be attributed to light-induced phase segregation.

This initial decrease in V_{OC} coupled with an increase in PL intensity is unusual. Studies typically report an increase in V_{OC} accompanied by an increase in PL intensity[96,97]. This parallel increase in V_{OC} and PL intensity can be attributed to halide ion redistribution, which reduces trap densities and decreases non-radiative recombination, thereby improving both PL and V_{OC}[96]. Another study suggests that light can also induce trap states, explaining the V_{OC} reduction but not the PL intensity increase of the peak at 675 nm[98]. One possible explanation for this phenomenon is that light induces a redistribution of ions in the bulk, thereby increasing the PL intensity[99]. At the same time, new defect states are introduced at grain boundaries or interfaces leading to a reduction in V_{OC}. Essentially, while the bulk properties improve (leading to higher PL), the interface properties might degrade (reducing the V_{OC}). The observed 22 mV decrease in V_{OC} from 90 seconds to 15 minutes, however, is likely caused by light-induced phase segregation. The linear increase of the PL emission peaks (at 675 and 775 nm) and the linear decrease in V_{OC} support this interpretation.

The experiment was repeated with the same cell after storing it in darkness for 3 days (Figure 17b). The resulting graph is nearly identical, with no indication of the PL emission of an I-rich perovskite phase at the start. This demonstrates the reversibility of the phase segregation[32]. Additionally, the electroluminescence (EL) of another cell (Figure 17c) shows similar trends. However, the process appears to be slower, which is also reported in reference[29]. This confirms that phase segregation is induced by excited charge carriers, whether generated by light or injected electrically.

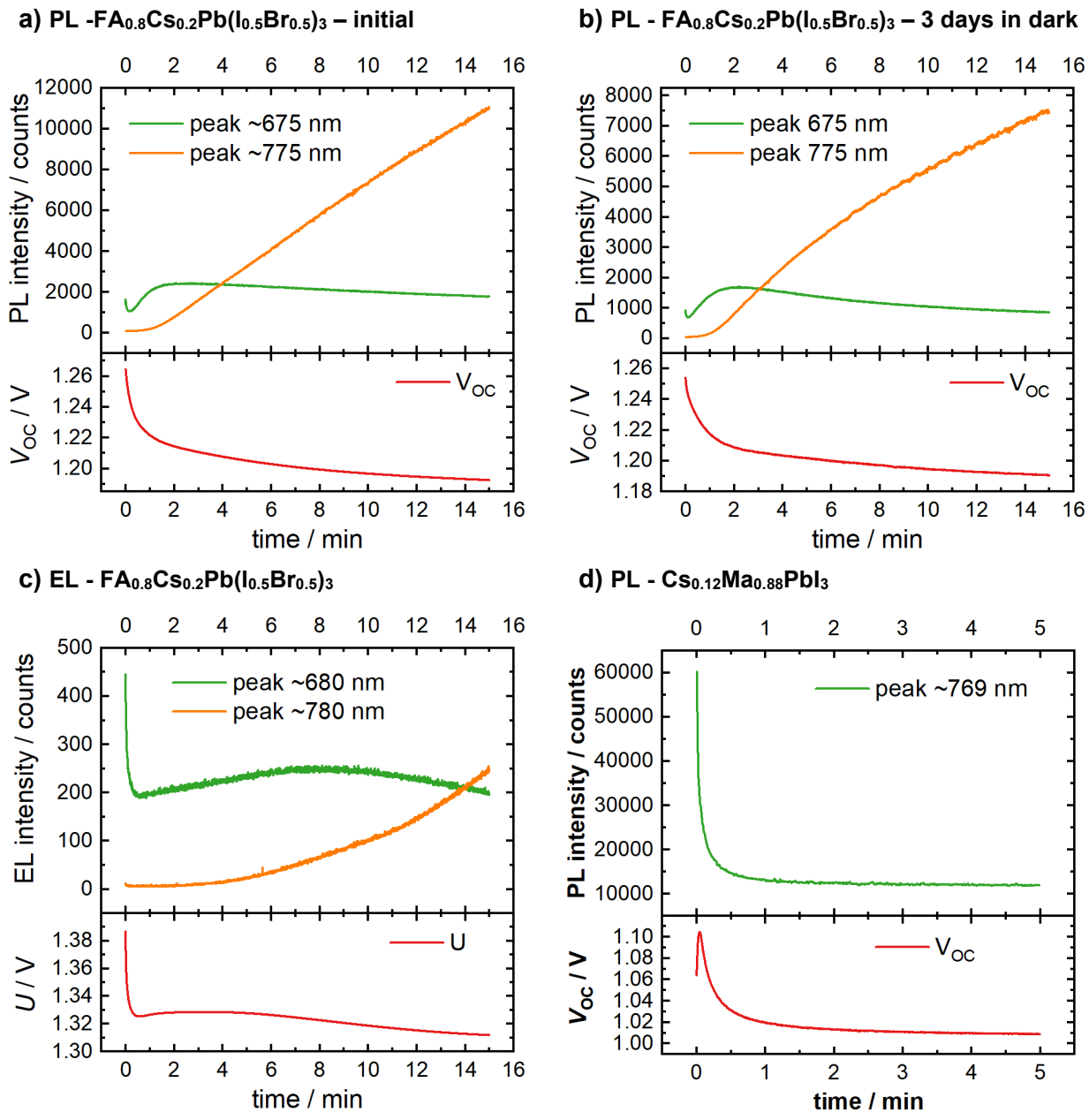

Figure 17. Time-dependent development of the luminescence peaks of PSC with simultaneous measurement of the V_{OC} **a)** PL measurement of the WBG PSC in this study with 3 mg mL^{-1} MACl additive and 0.25 mg mL^{-1} PEAI in IPA post-treatment (488 nm, 3.2 mW, 100 µm, 0.27 s) **b)** PL measurement of the same cell after 3 days rest in darkness (488 nm, 3.1 mW, 100 um, 0.27 s) **c)** EL of the WBG PSC (2 mA, 800 µm, 0.27 s) **d)** reference PL measurements of pure iodine PSC (488 nm, 1 mW, 100 µm, 0.27 s).

3.1.6. SiO_x protection layer

For the protection of the PSCs for measurements, a 400 nm thick SiO_x layer was evaporated onto the finished cell. This protective coating should shield the cells from damage caused by humidity and oxygen during measurements under ambient conditions[100]. As shown in Figure 18, protected cells retain 84 % of their initial PCE after 2500 hours when stored under ambient conditions (40 – 60 % relative humidity, 22 °C). In contrast, unprotected cells drop below 80 % of their initial PCE after only 165 hours. Thus, measurements such as EQE, PL, and even extended measurements

like maximum power point tracking can be performed under ambient conditions without adversely affecting the device's performance.

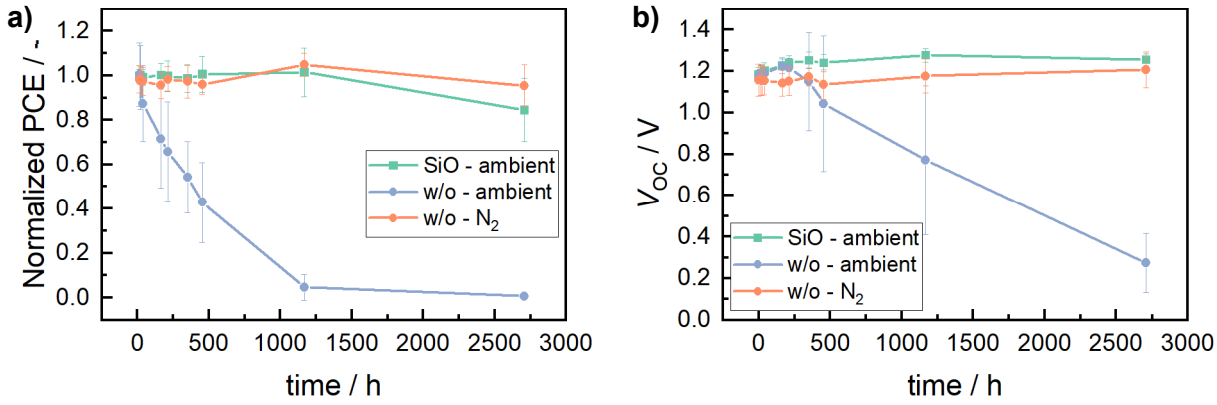

Figure 18. Storage stability at ambient conditions (40 – 60 %RH, 22 °C) of WBG PSC without additive or treatment with one group protected with a 400 nm thick SiO_x layer and another group unprotected (w/o). Some cells were stored in a nitrogen filled glovebox for reverence (N_2) with **a)** normalized to the initial PCE and **b)** V_{OC} development.

3.1.7. Temperature and solvent stability

Understanding the temperature stability of the perovskite subcell is crucial for processing the top layers of the TSC. Figure 19a illustrates the temperature stability of the perovskite cell. The cell remains stable up to 100 °C with the PCE decrease below 80 % at 110 °C and falling below 20 % of the initial PCE value at 120 °C. Although the cells, on average are barely damaged at 100 °C, the high standard deviation indicates that some cells undergo transformations that reduce efficiency. The MeO-2PACz and the perovskite layer are very stable at 100 °C, so any transformation is likely induced in the PCBM and/or BCP layer or is due to increased diffusion between the layers. The J_{SC} and FF show a similar behavior and decrease below 50 % and 76 % of the initial value at 120 °C, respectively. Interestingly, the absolute value of the V_{OC} (Figure 19b) increases up to 100 °C. Previous studies have shown that heat treatment (85 °C for 10 min) can passivate defects and improve performance[101]. This could explain the observed increase in V_{OC} after the temperature treatment.

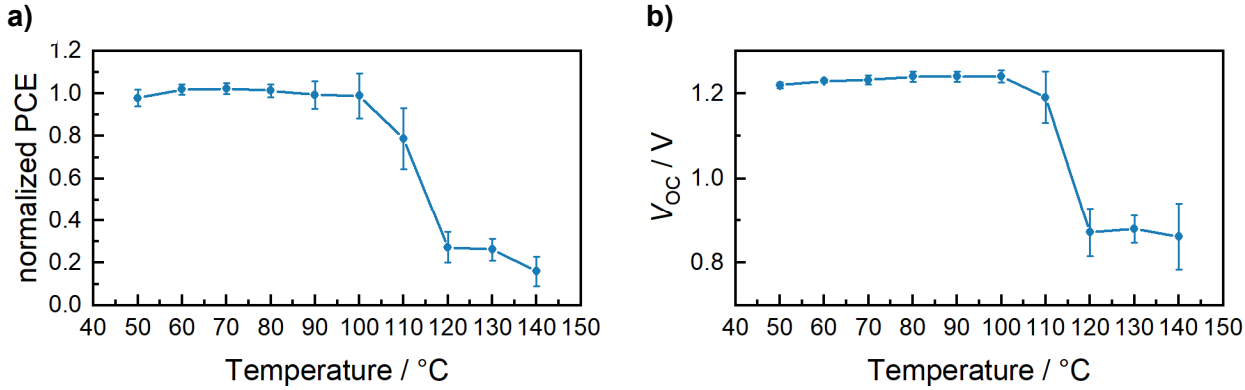

Figure 19. Temperature stability of WBG PSC (MACl + PEAI) with PV parameters extracted from *J*(V) measurements with **a)** normalized PCE relative to the initial PCE and **b)** V_{OC} development

Solvent stability is another crucial factor influencing TSC fabrication. Figure 20 presents the results of various solvent exposures of finished WBG PSC. Although, the 100 nm thick Ag top electrode provides some protection, this experiment still offers valuable insights into which solvents are critical to avoid and which may be used safely. DMSO significantly degrades cell performance, reducing PCE below 10 %. DMSO, a dipolar solvent often used in perovskite precursor solutions, can dissolve the perovskite layer and also the BCP and PCBM layers, apparently. In contrast, the highly polar MeOH causes only a slight reduction in PCE to 90 %. Alcohols with longer chain lengths, such as ethanol, isopropanol, and n-butanol, have no significant effect on performance. The solution of TritonX-100 in IPA, used for treating the HTL of the organic subcell, has minimal impact, with no performance change at 1 vol% and a slight drop at 5 vol%.

Apolar solvents like toluene, CB, and CF are known to dissolve PCBM, which is critical as many donor-acceptor mixtures are dissolved in these solvents. This is reflected in the reduced PCE values after exposure to toluene (80 %, relative to pristine cell), CB (66 %), and CF (47 %). To protect the PCBM and BCP layers from apolar solvents, a 10 nm thick MoO_x layer was tested. MoO_x represents a permeation barrier[102,103] and successfully prevents PCBM dissolution, as shown in Figure 21. Additionally, MoO_x can serve as an effective HTL for OSCs[67,104], essentially providing protection while still allowing holes to be transported to the recombination layer of a perovskite organic TSC.

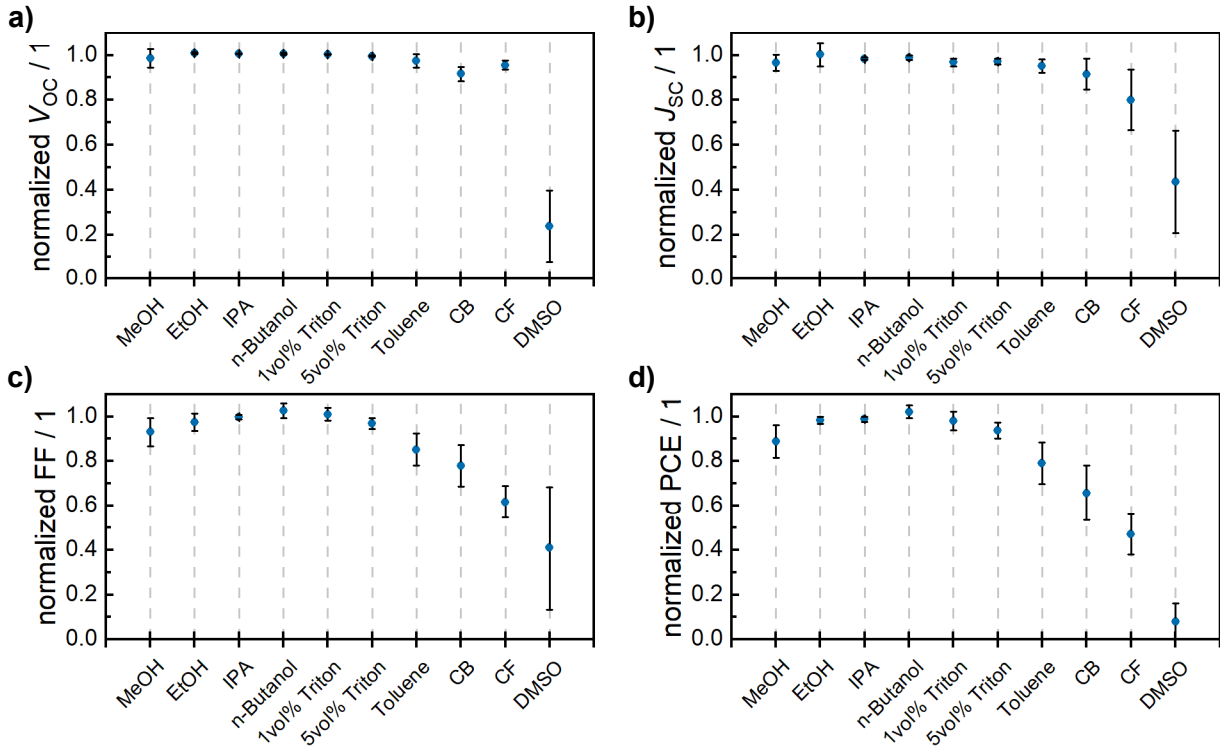

Figure 20. Solvent stability of the WBG PSC (MACl + PEAI) towards an exposure to 200 µL of the respective solvent for 30 s with normalized values relative to the value before the exposure. Values obtained by *J*(V) measurements. With **a)** normalized V_{OC} **b)** normalized J_{SC} **c)** normalized FF **d)** normalized PCE.

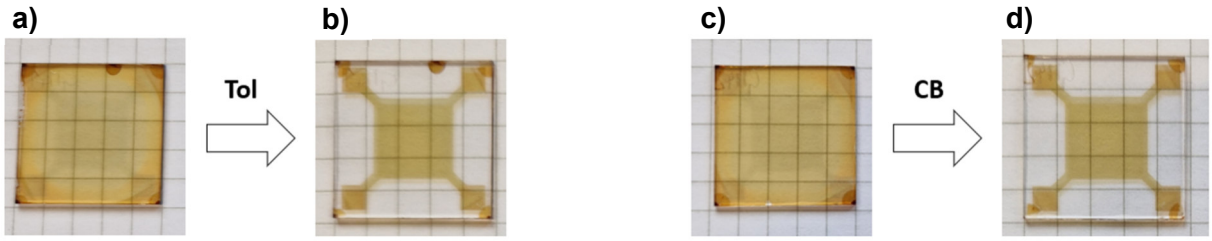

Figure 21. Effect of a toluene and CB exposure on a PCBM layer protected by 10 nm MoO_x **a)** before toluene exposure **b)** after toluene exposure **c)** before CB exposure **d)** after CB exposure.

3.1.8. Electron transport layer variation

Figure 22 illustrates the effects of adding PMMA to the PCBM solution. The addition of PMMA is expected to decrease aggregation of PCBM to enhance film quality and reduce defects, which should increase both V_{OC} and J_{SC}[105]. In TSCs, this improved film quality can help cover peaks from the underlying perovskite layer, facilitating better processing of the top cell. Microscope images (Figure 23) reveal a decrease in particle density with the addition of 1 mg mL^{-1} PMMA. However, this study found no significant effect on performance, the mean V_{OC} and J_{SC} remain unchanged with PMMA concentrations of 0.1 and 1 mg mL^{-1}. In addition, PMMA seems to increase variability as indicated by the wider range in the box plots for 1 mg mL^{-1}. Therefore, PMMA is not included in the final TSC design.

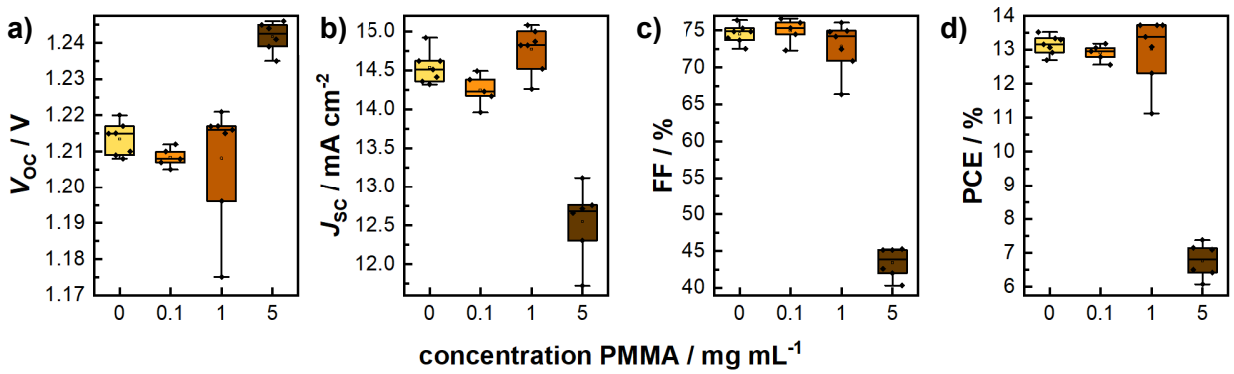

Figure 22. Box plot diagrams with PV performance extracted from *J*(V) measurements testing the iInfluence of addition of PMMA to PCBM on the performance of WBG PSC (MACl + PEAI) with **a)** V_{OC} **b)** J_{SC} **c)** FF and **d)** PCE.

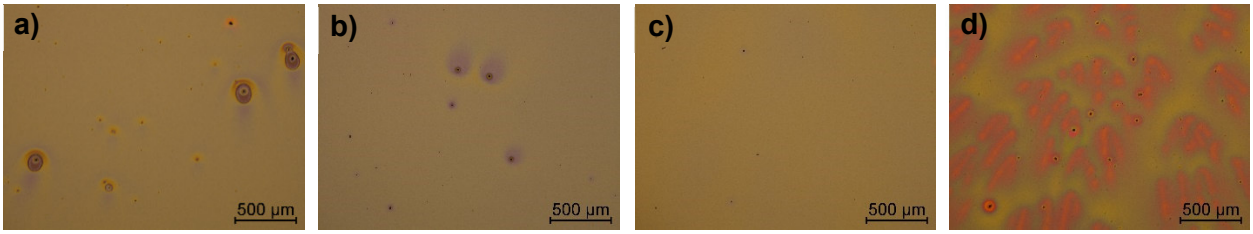

Figure 23. Microscope images of PCBM films with addition of PMMA with **a)** 0 mg mL^{-1} **b)** 0.1 mg mL^{-1} **c)** 1 mg mL^{-1} and **d)** 5 mg mL^{-1}

TiO_x can serve as a buffer layer between PCBM and the top electrode instead of BCP. A buffer layer is necessary to address the energy level mismatch between the LUMO of PCBM and the

metal electrode, which leads to inefficient charge extraction[82,106,107]. Common buffer layers like LiF, MgO, ZnO, BCP, or TiO_x are employed to align the energy levels and mitigate this barrier[82,106,107]. TiO_x is a promising alternative to BCP due to it higher thermal stability and it may also protect the perovskite layer from solvents used in subsequent TSC stacking[108,109].

Figure 24a – d compares the performance of devices with TiO_x and BCP buffer layers. Higher dilution of the TiO_x stock solution was intended to reduce the layer thickness, but accurately determining the TiO_x layer thickness was challenging, since its below 10 nm. TiO_x cells notably underperform in terms of FF and J_{SC} compared to the BCP cells. With a dilution of 1:1000, the J_{SC} was reduced to 9.5 mA cm^{-2}, compared to 7 mA cm^{-2} with a 1:100 dilution. The overall cell performance remains poor with FF not exceeding 30 %. The J(V) curves (Figure 25) show a pronounced S-shape for TiO_x cells. This S-shape is typically indicative of a charge transport barrier at the interfaces[110]. Despite testing various dilutions, the TiO_x layer might be too thin. A too-thin TiO_x layer can result in direct contact between PCBM and the metal electrode, causing degradation and creating a charge transport barrier[82]. Fabricating a device without the BCP and the TiO_x layer could help determine if this is the issue. Changing the top contact to Al did also not eliminate the S-shape, further confirming the issue with a charge transport barrier.

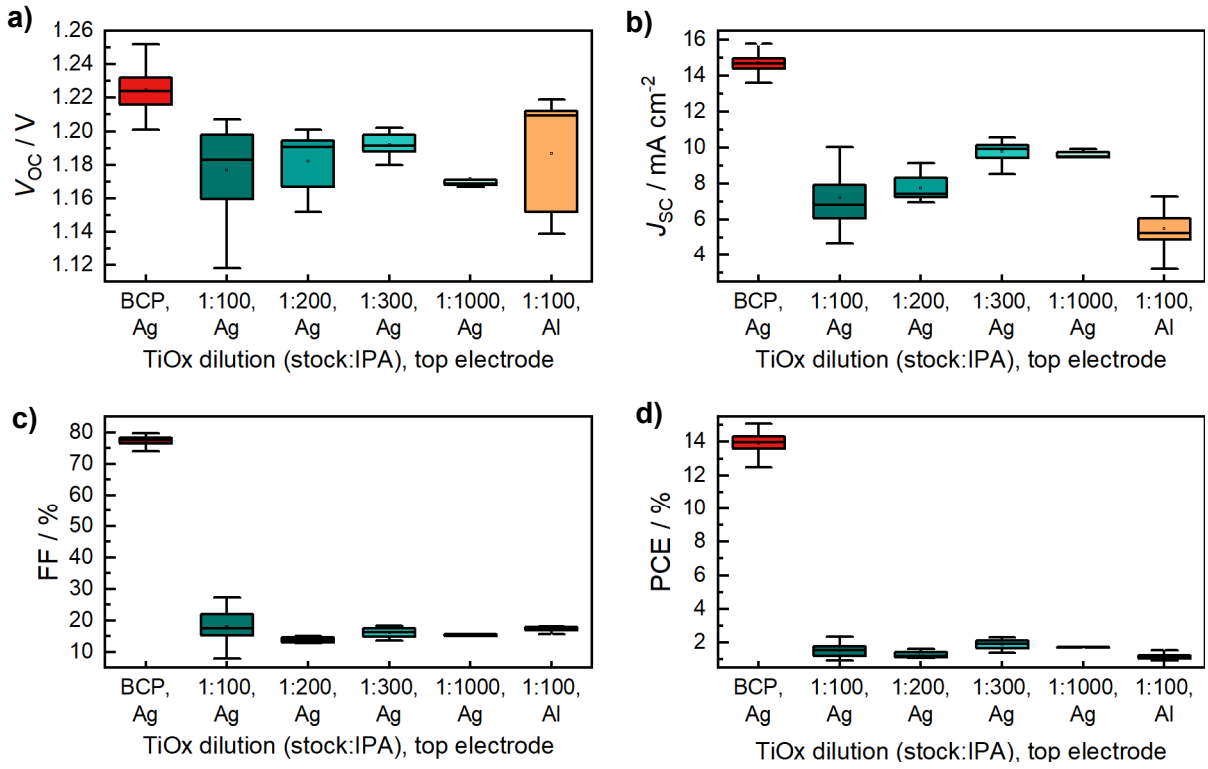

Figure 24. Box plot diagrams with PV performance extracted from J(V) curves testing the performance of WBG PSC (MACl + PEAI) due to a replacement of BCP with TiO_x and the exchange of Ag with Al as the top contact with **a)** V_{OC} **b)** J_{SC} **c)** FF **d)** PCE and **e)** J(V) curves.

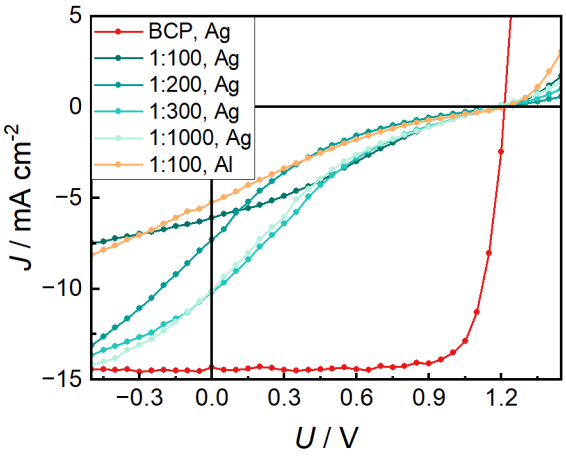

Figure 25. *J*(V) curves of WBG PSC (MACl + PEAI) with different buffer layers (BCP and TiO_x) and the exchange of Ag with Al as the top contact. Different dilutions of the TiO_x stock solution were tested (TiO_x stock:IPA = 1:x).

3.2. Organic solar cells

3.2.1. Enhancing PEDOT Solar 3 performance on P3HT:PCBM solar cells

PEDOT:PSS formulations are frequently used in OSCs as the HTL[62,111,112]. However, they are usually a suspension in water, which is detrimental to the perovskite subcell[113,114]. Therefore, Solar 3, the PEDOT formulation in toluene was tested as an alternative. To conserve materials, the optimization of the Solar 3 layer was conducted using the model active layer P3HT:PCBM, while maintaining the rest of the device architecture. The results of this optimization are presented in Figure 26. Initially, Solar 3 performs significantly worse (V_{OC} = 0.2 V, J_{SC} = 5.9 mA cm^{-2}, FF = 25 %, PCE = 0.25 %) than the PEDOT:PSS reference Al4083 (V_{OC} = 0.51 V, J_{SC} = 7.5 mA cm^{-2}, FF = 52 %, PCE = 2.0 %), rendering it unsuitable for TSC applications. Due to the limited studies, employing Solar 3, optimization methods for PEDOT:PSS suspensions in water are adapted. Attempts to dope the solution resulted in unstable suspensions with visible particles that could not be filtered, leading to defective films. Thus, post-treatment of the annealed Solar 3 film is proposed.

A post-treatment aims to enhance PEDOT conductivity through various mechanisms, including morphology changes, and removal of excess of PSS, reorientation of PEDOT chains for better connection and screening effect of polar groups inserted between PEDOT, and the counter-ionomer[114–120]. Additionally, altering the surface work function of Solar 3 might be necessary due to the different counter-ionomer.

Ionic liquid post-treatments have been shown to enhance PEDOT:PSS conductivity by altering the molecular ordering of PEDOT and PSS due to ionic interactions[116,117,119]. Despite the use of ionic liquids such as EMIM-FSI, BMPyrr-FSI and EMIM-BF_4, the effect is minor, with devices achieving only half the PCE of the reference cells and a V_{OC} between 0.3 to 0.4 V.

DMSO post-treatment should significantly increase the PEDOT:PSS conductivity, potentially up to 930 S cm^{-1}, by inducing morphological changes, producing elongated PEDOT grains[117]. This treatment improves the performance of Solar 3 to a PCE above 1.5 %, even with a reduced DMSO concentration of 5 vol%. The best J_{SC} is achieved with a combination of DMSO and MeOH treatment. While MeOH alone yields a PCE of 1.5 %, the combination reaches 1.7 % with a J_{SC} of 7.5 mA cm^{-2}, identical to reference cells. However, as discussed in Section 3.1.7. , MeOH and DMSO damage the PCS and are unsuitable for post-treatment.

Studies report, that post-treatments with alcohols (MeOH, IPA, n-BuOH) leads to a conductivity enhancement of PEDOT:PSS, with values of 1015, 468 and 286 S cm^{-1}, respectively [115]. Although IPA post-treatment has a minimal effect (PCE = 0.6 %), MeOH (PCE = 1.5 %) and n-BuOH (PCE = 1.6 %) treatments are viable options to enhance the charge transport properties of Solar 3.

Surfactants like TritonX-100 and Zonyl FS-300 significantly enhance PEDOT:PSS conductivity when added to aqueous solutions[118,120]. Post-treating the Solar 3 layer with a 5 vol% TritonX-100 solution in IPA results in P3HT:PCBM cells with the highest V_{OC} among all treatment options (0.5 V), comparable to the reference cells. The PCE is around 1.7 %, close to reference cells (2.0 %). Reducing TritonX-100 concentration to 1 vol% maintained good results without harming the perovskite (see Section 3.1.7.). In this study, the treatment with a 1 vol% TritonX-100 treatment provided the best compromise between solvent compatibility with the perovskite and Solar 3 enhancement.

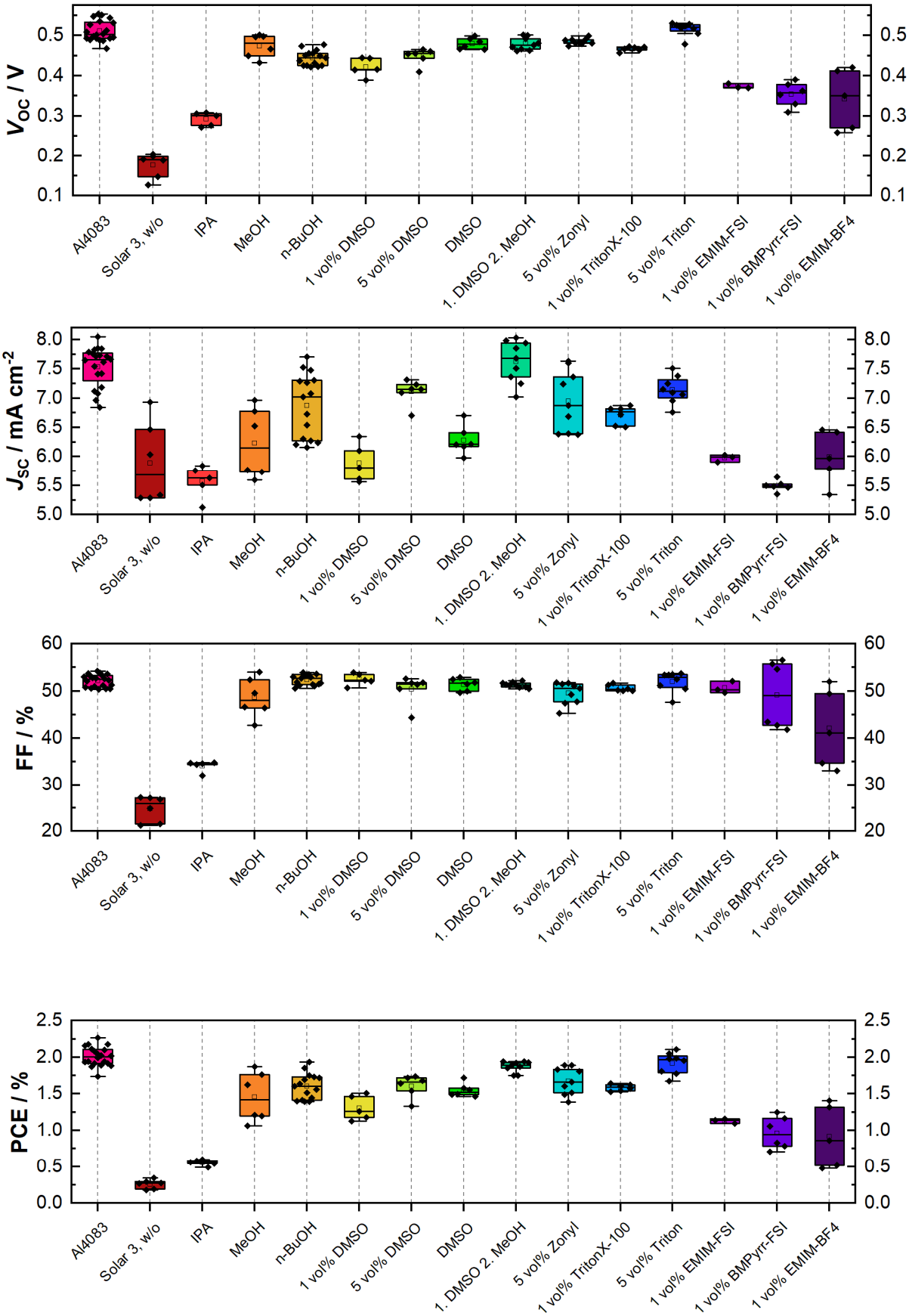

Figure 26. Box plot diagrams with PV parameters extracted from *J*(V) curves of P3HT:PCBM OSCs with different post-treatment of the Solar 3 layer with various solvents/solutions on the performance of P3HT:PCBM OSCs DMSO, Zonyl and TritonX-100 were diluted with IPA ionic liquids with THF with **a)** V_{OC} **b)** J_{SC} **c)** FF and **d)** PCE.

3.2.2. PTB7-Th:IEICO-4F solar cells

Figure 27 and Table 9 PV parameters extracted from *J*(V) curves of PTB7-Th:IEICO-4F OSCs processed on different HTLs are reported. Al4083 is used again as a reference HTL. Similar to the results observed with P3HT:PCBM OSCs, the untreated Solar 3 exhibited poor performance (V_{OC} = 0.69 V, J_{SC} = 15.3 mA cm^{-2}, FF = 49 %, PCE = 5.5 %) compared to the reference cells (V_{OC} = 0.75 V, J_{SC} = 19.3 mA cm^{-2}, FF = 63 %, PCE = 9.1 %). Post-treatment with 1 vol% TritonX-100 significantly improved the PCE by 2.3 % primarily due to an increase in FF by 13 % (V_{OC} = 0.72 V, J_{SC} =16.5 mA cm^{-2}, FF = 62 PCE = 7.4 %). Despite these improvements, both reference and Solar 3 + Triton cells show lower FF and J_{SC} compared to values reported in literature. For instance, Hu et al. reported a PCE of 11.3 % (V_{OC} = 0.71 V, J_{SC} = 22.9 mA cm^{-2}, FF = 67 %) with the same device architecture but with an Al top contact instead of Ag[62]. Similarly, Wang et al. achieved a J_{SC} of 25.1 mA cm^{-2} (V_{OC} = 0.72 V, FF = 61 %, PCE = 11.1 %) using 1,8-iodooctane as a solvent additive, PFN-Br as ETL and Al top contact[64]. The reduced J_{SC} in this study is mostly attributed to a thinner active layer thickness (80 nm) compared to the ~100 nm thickness reported in previous studies[62,64]. A thin active layer can result in incomplete light absorption, and reduction of J_{SC}. Conversely, in a too thick active layer the charge carriers may recombine before reaching the electrodes[121].

Replacing Solar 3 with MoO_x as the HTL led to even lower performance (V_{OC} = 0.60 V, J_{SC} = 14.5 mA cm^{-2}, FF = 50 %, PCE = 4.4 %). However, adding a TritonX-100 treated Solar 3 layer on top improved the PCE to 6.2 %. Despite this improvement, the performance remains below reported literature values, where a PCE of 11.0 % was achieved. It should be noted that a different stack configuration (n-i-p) was used[67]. In the p-i-n configuration used in this study MoO_x, is directly evaporated onto ITO, potentially resulting in a poor contact.

Besides optimizing the active layer thickness, solvent additives are a viable option to enhance OSC performance. Solvent additives induce morphology changes in the bulk heterojunction, leading to enhanced phase separation of donor and acceptor materials, thereby improving performance[122]. Although not tested in this thesis, several additives such as 1,8-iodooctane[123], 1-chloronaphthalene[63] or diphenyl ether[124], offer promising ways to improve performance. For example, the addition of 4 % 1-chloronaphthalene to the PTB7-Th:IEICO-4F blend solution yielded an impressive J_{SC} of 27.3 mA cm^{-2} [63].

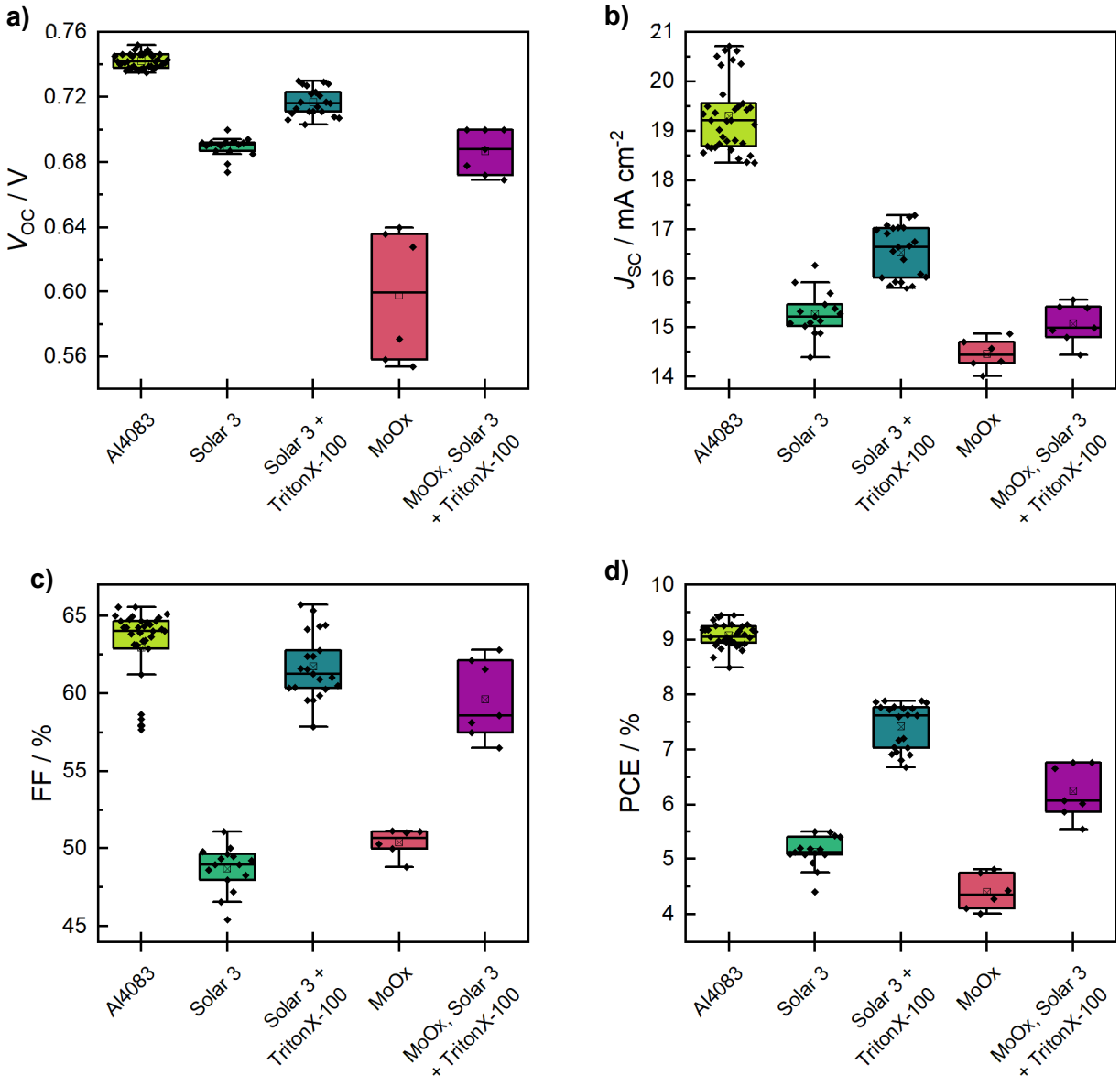

Figure 27. Box plot diagrams with PV parameters extracted from *J*(V) curves of PTB7-Th:IEICO-4F OSC applying different HTLs with **a)** V_{OC} **b)** J_{SC} **c)** FF and **d)** PCE.

Table 9. PV parameters extracted from *J*(V) curves of PTB7-Th:IEICO-4F OSC applying different HTLs and treatments.

HTL + treatment	V_{OC} / V	J_{SC} / mA cm^{-2}	FF / %	PCE / %	N
Al4083	0.75 (0.74 ± 0.01)	20.7 (19.3 ± 0.7)	66 (63 ± 3)	9.5 (9.1 ± 0.2)	35
Solar 3	0.70 (0.69 ± 0.01)	16.3 (15.3 ± 0.5)	51 (49 ± 1)	5.5 (5.1 ± 0.3)	15
Solar 3 + TritonX-100	0.73 (0.72 ± 0.01)	17.3 (16.5 ± 0.5)	66 (62 ± 2)	7.9 (7.4 ± 0.4)	21
MoO_x, Solar 3 + TritonX-100	0.70 (0.69 ± 0.01)	15.6 (15.1 ± 0.4)	63 (60 ± 3)	6.8 (6.2 ± 0.5)	7
MoO_x	0.64 (0.60 ± 0.04)	14.9 (14.5 ± 0.3)	51 (50 ± 1)	4.8 (4.4 ± 0.3)	6

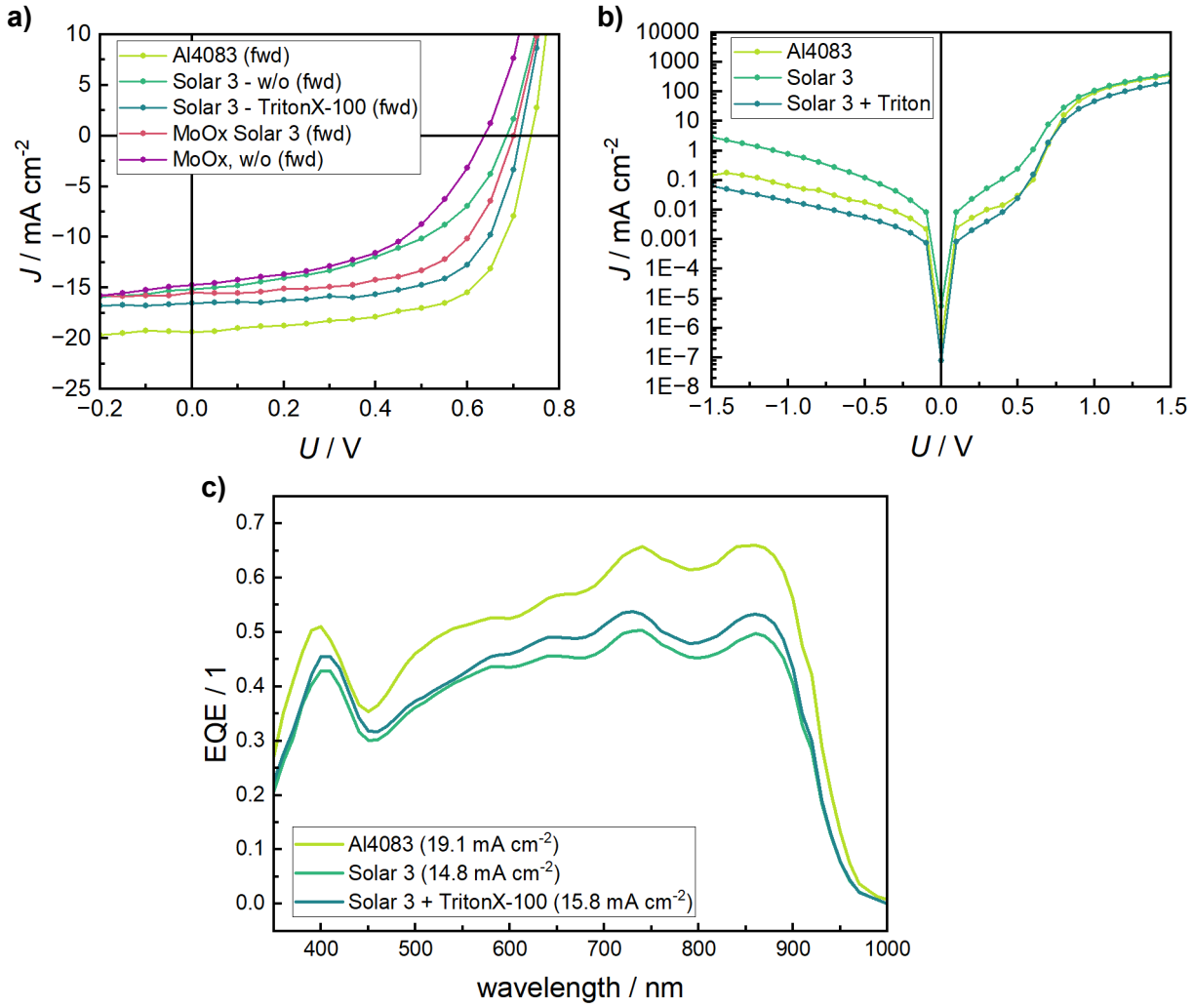

Figure 28. Optoelectrical measurements of PTB7-Th:IEICO-4F OSCs having different HTLs with **a)** illuminated *J*(V) curves (100 mW cm^{-2}) **b)** dark *J*(V) curves and **c)** EQE spectra.

The *J*(V) plots recorded under illumination (Figure 28a) of PTB7-Th:IEICO-4F cells show the increase in FF for cells treated with TritonX-100 on the Solar 3 layer, resulting in a more rectangular curve and higher efficiency. Both Solar 3 without treatment and Al4083 cells exhibit relatively low parallel resistance, indicated by the significant increase in current density at low voltage. This low parallel resistance suggests leakage paths, primarily caused by defects. TritonX-100 treatment is able to increase the parallel resistance. The dark curves (Figure 28b) reveal a low leakage current (at -0.5 V) for Solar 3 + Triton cells (5.4 $\cdot 10^{-3}$ mA cm^{-2}) and higher for Al4083 (18 $\cdot 10^{-3}$ mA cm^{-2}) and Solar 3 w/o (123 $\cdot 10^{-3}$ mA cm^{-2}).

The EQE spectra of the reference cell with Al4083, Solar 3, and Solar 3 + TritonX-100 treatment (Figure 28c) demonstrate efficient current delivery between 350 and 950 nm. High EQE values are especially observed between 700 and 920 nm, crucial since this light is not absorbed by the perovskite subcell. The calculated J_{SC} for the three HTL variations is consistent with the values extracted from the *J*(V) curves.

3.2.3. Absorption and reflection

The absorptance and reflectance spectra of PTB7-Th, IEICO-4F, and the donor-acceptor blend are shown in Figure 29a - b. PTB7-Th exhibits two absorption peaks at 640 and 705 nm, while IEICO-4F extends its absorption into the NIR region up to 950 nm. This extended absorption is the key benefit of NIR-non-fullerene acceptors. It allows OSCs to absorb a broader part of the solar spectrum, thus making OSC ideal as the rear subcell in TSC. The high absorption between 600 and 900 nm aligns well with the WBG perovskite absorption edge at 670 nm (Figure 14a in Section 3.1.4.). However, the PTB7-Th:IEICO-4F blend has a relatively high reflectance between 800 and 950 nm, leading to significant losses. Additionally, the perovskite also shows high reflectance between 670 and 950 nm. Nevertheless, these losses will be partially mitigated by back reflection into the organic subcell.

The Tauc plots of the donor and the acceptor are shown in Figure 29c, with the resulting band gaps listed in Table 10. PTB7-Th has a band gap of 1.65 eV, while IEICO-4F has a band gap of 1.34 eV. The lower band gap of the acceptor facilitates efficient exciton dissociation[54]. Consequently, the band gap of the donor-acceptor blend is determined by the lowest band gap component, which is IEICO-4F at 1.34 eV. These measured band gaps are consistent with values reported in the literature for PTB7-Th (1.61 eV)[65] and IEICO-4F (1.25 eV)[60].

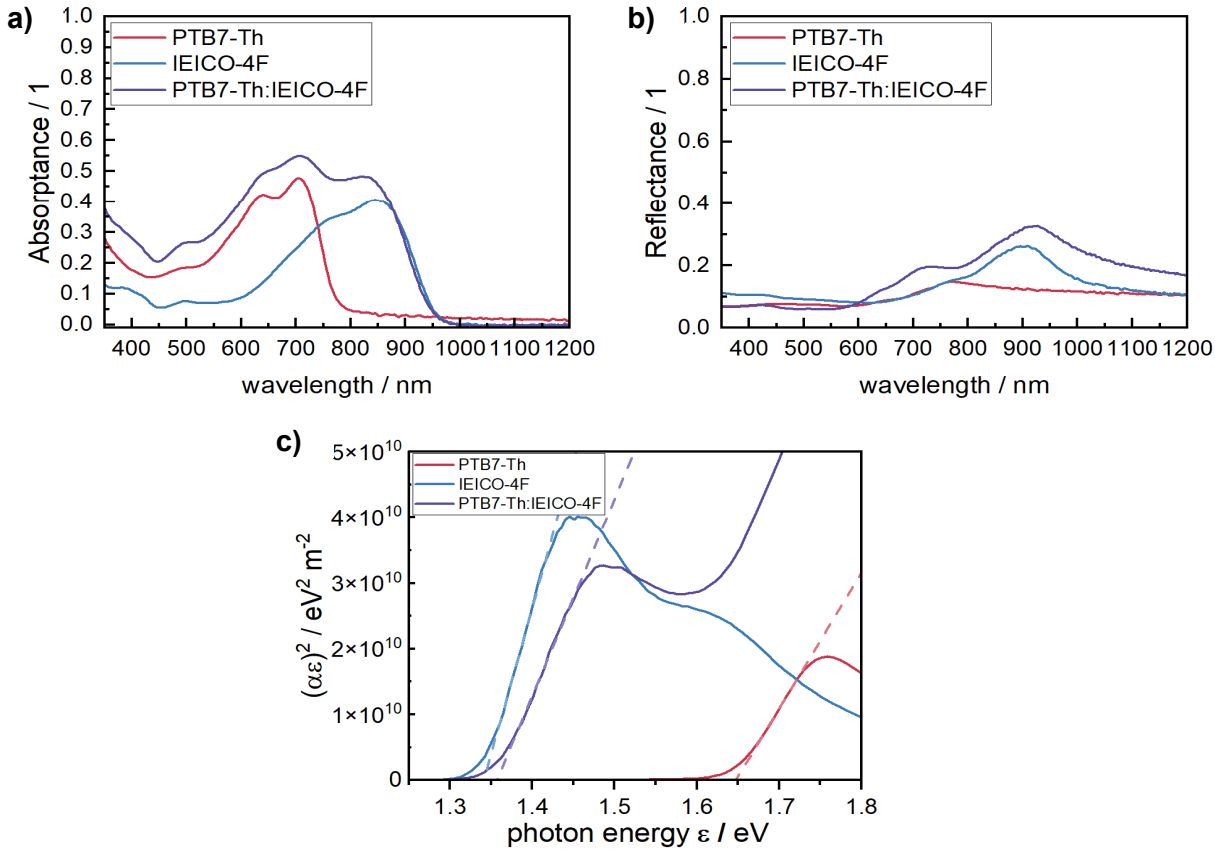

Figure 29. UV-Vis measurements of PTB7-Th (6 mg mL^{-1} D + 9 mg mL^{-1} PS in CB), IEICO-4F (9 mg mL^{-1} A+ 6 mg mL^{-1} PS in CB) and PTB7-Th:IEICO-4F (6 mg mL^{-1} D + 9 mg mL^{-1} A in CB) films on glass with **a)** absorptance **b)** reflectance **c)** Tauc plot.

Table 10. Band gaps of PTB7-Th, IEICO-4F and PTB7-Th:IEICO-4F blends determined by the Tauc method.

Film	Band gap / eV
PTB7-Th	1.65
IEICO-4F	1.34
PTB7-Th:IEICO-4F	1.36

3.2.4. Photoluminescense

Figure 30 presents the PL spectra of PTB7-Th, IEICO-4F, and their blend. PTB7-Th exhibits a strong PL peak at 759 nm, while IEICO-4F shows a peak at 930 nm. In the blend, no significant PL signal is observed, indicating quenching of the excited state[125]. This quenching confirms efficient exciton dissociation in the blend. The rapid charge transfer to the acceptor and vice versa prevents the exciton from returning to the ground state via photon emission[125]. Consequently, the exciton diffusion length exceeds the mean path from the donor to the acceptor within the interconnecting network of the bulk heterojunction.

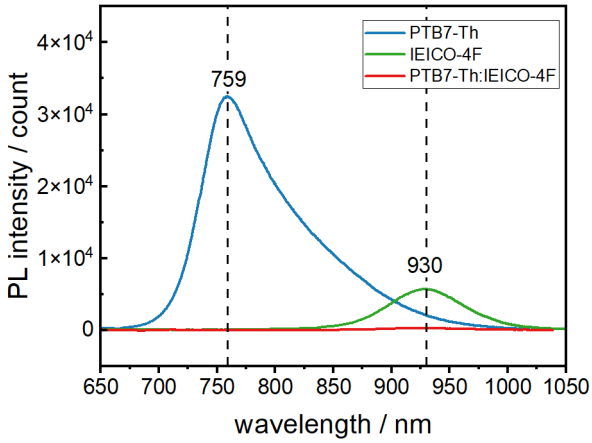

Figure 30. PL spectra of PTB7-Th (6 mg mL^{-1} D + 9 mg mL^{-1} PS in CB), IEICO-4F (9 mg mL^{-1} A + 6 mg mL^{-1} PS in CB) and PTB7-Th:IEICO-4F (6 mg mL^{-1} D + 9 mg mL^{-1} A in CB) films on glass

3.2.5. Atomic force microscopy

The AFM images of the PTB7-Th:IEICO-4F film are shown in Figure 31. The films exhibit minimal roughness, indicating that the spin-coating procedure is well-optimized for producing high-quality PTB7-Th:IEICO-4F films. The films were fabricated directly on a cleaned glass slide, resulting in very low surface roughness. However, this changes significantly when the layer is deposited on top of the perovskite subcell, as the surface will have a higher roughness, even with an ICL in between.

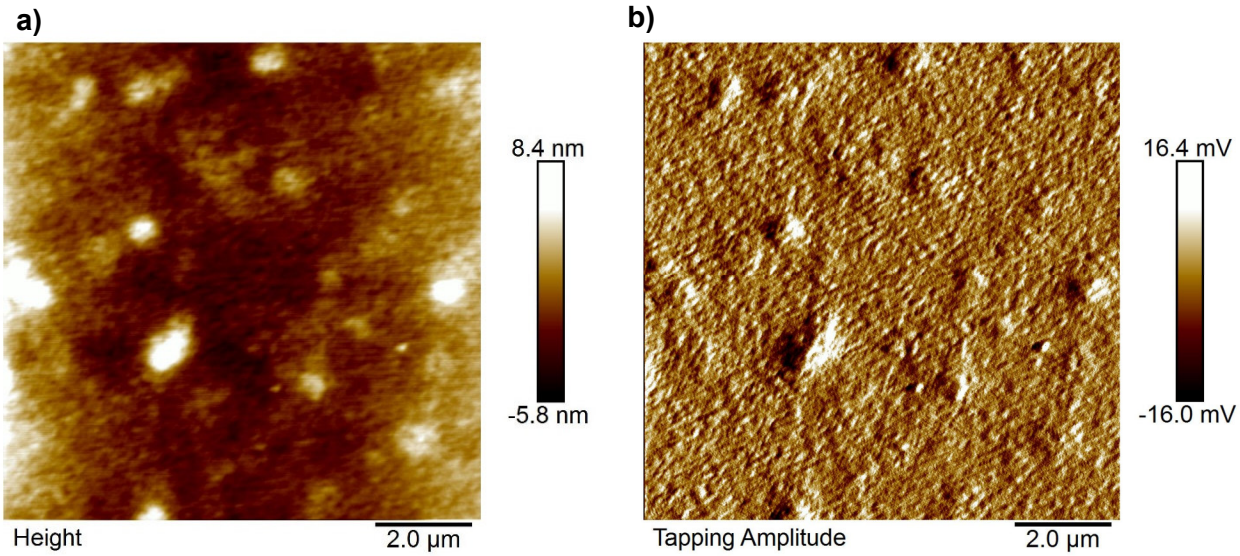

Figure 31. Atomic force spectroscopy images of a PTB7-Th:IEICO-4F (6 mg mL^{-1} D + 9 mg mL^{-1} A in CB) film with **a)** height profile **b)** tapping amplitude

3.3. Tandem solar cell

3.3.1. Testing MoO_x as a protection layer in the interconnecting layer

First, two different ICLs were tested in the TSC. In Figure 32a, the *J*(V) curve shows an ICL with the architecture PCBM/BCP/Ag (5 nm)/Solar 3. In contrast, Figure 32b depicts the *J*(V) curve with an additional 10 nm MoO_x layer inserted between Ag and Solar 3, showing clear differences between the two configurations. In the configuration where Solar 3 is processed directly on top of the PCBM/BCP/Ag stack, the *J*(V) curve exhibits strange electrical behavior with large positive currents in the forward direction and a low breakdown voltage (-0.3 V). This may be caused by a dissolution of the PCBM/BCP/Ag layers by the apolar toluene in the Solar 3 suspension. This could result in direct contact between Solar 3 and the perovskite layer, which is likely not forming an ohmic contact.

As already discussed in Section 3.1.7. a thin MoO_x layer (10 nm) effectively prevents dissolution of underlying layers, improving the ICL to achieve a V_{OC} of 1.68 V. In an ideal scenario, the sum of the V_{OC} s from the single PSC and OSC would be 1.92 V, indicating a loss of 0.24 V in the TSC. While the ICL properties are improved, an ohmic contact is not established, as the *J*(V) curve exhibits a significant S-shape. This suggests the formation of a potential barrier that acts as a counter diode, leading to charge transport issues at some interlayer. This contributes to a poor FF and some degree of voltage loss, which will be further discussed in Section 3.3.2.

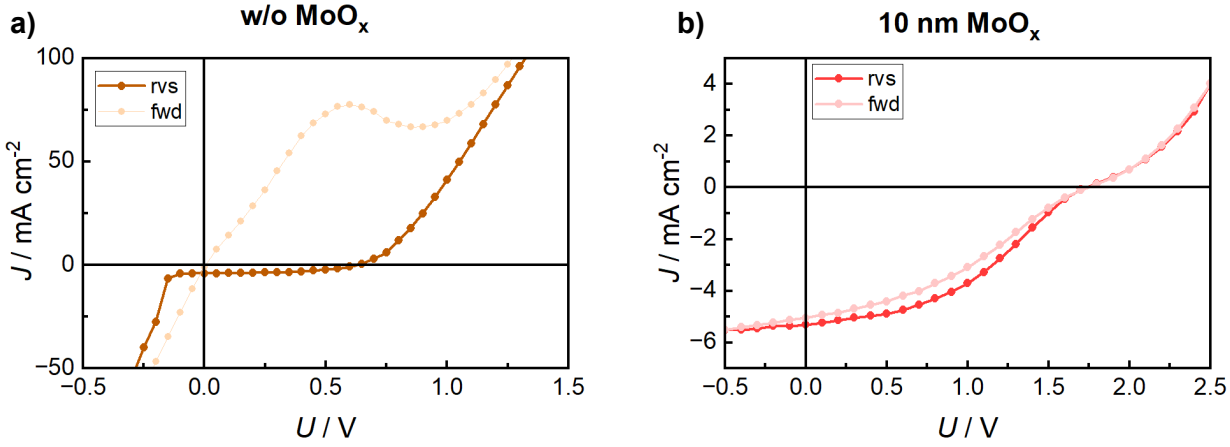

Figure 32. *J*(V) curves of perovskite organic TSC with **a)** no MoO_x inserted between the RL and Solar 3 **b)** 10 nm MoO_x inserted between the RL and Solar 3.

3.3.1. Recombination layer thickness optimization

In Figure 33 and Table 11 the PV parameters of TSC with Ag RLs of varying thicknesses (0, 1, 2 and 5 nm) are presented. The thickness of the RL critically influences the performance, which is particularly evident in the J_{SC} of the devices. Without an Ag layer, the cells exhibit inefficient recombination, resulting in the J_{SC} dropping below 2 mA cm^{-2}. This inefficiency leads to electron and hole accumulation at the interface between the subcells, resulting in increased recombination losses and the formation of a potential barrier, which further reduces the device's efficiency.

The best performance in this array is observed with a 1 nm thick Ag layer, achieving a J_{SC} of 8.7 mA cm^{-2}. Increasing the thickness beyond this point results in decreased performance. The insertion of an Ag layer unavoidably introduces optical losses due to reflection and absorption. This reduces the current, generated by the organic rear subcell and consequently lowers the overall current of the TSC. As the thickness of the Ag layer increases, these optical losses become more pronounced[15]. Therefore, precise control of the RL layer thickness is essential to maximize the efficiency of TSC.

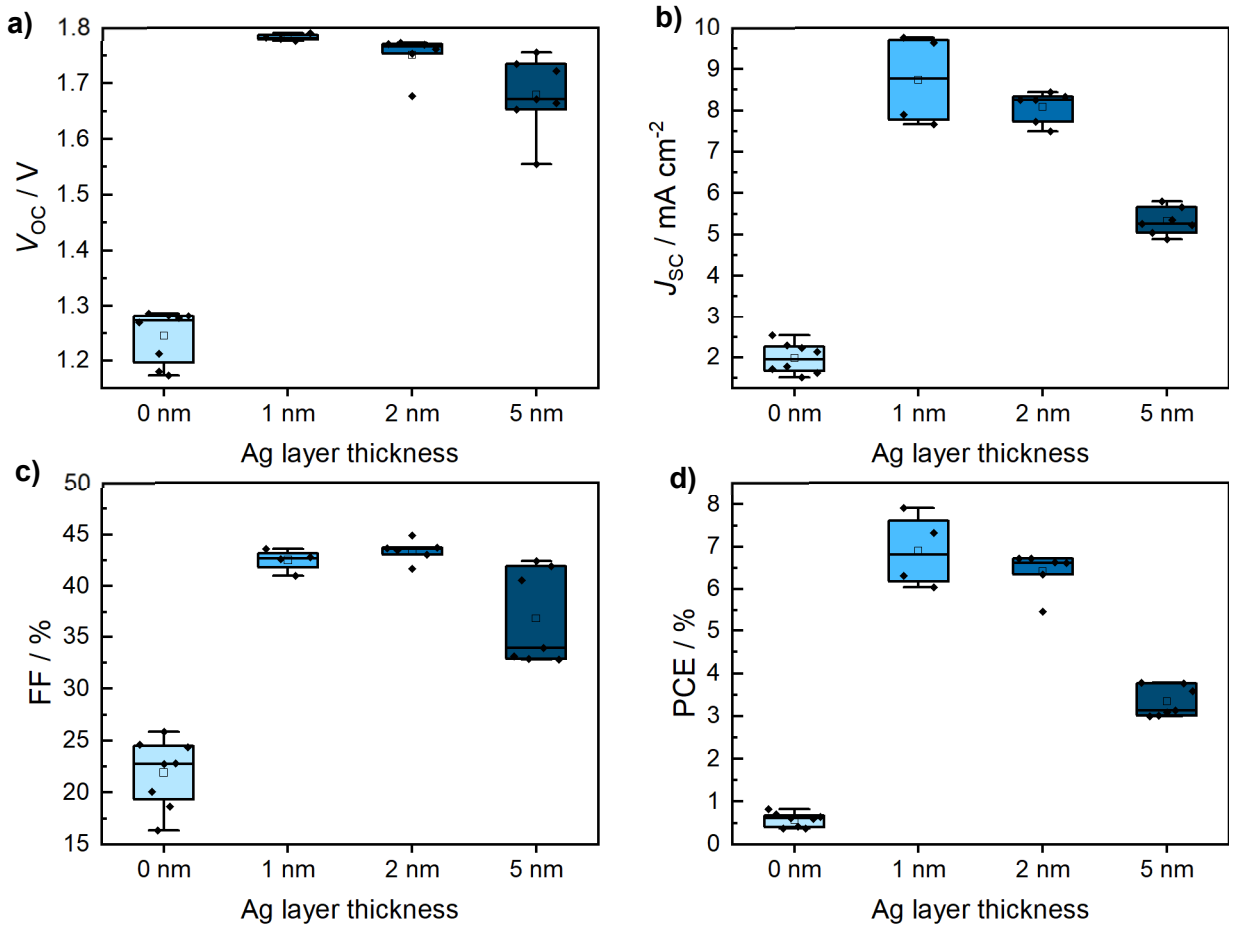

Figure 33. Box plot diagrams with PV parameters extracted from *J*(V) curves of TSC with different RL thickness with **a)** V_{OC} **b)** J_{SC} **c)** FF and **d)** PCE.

Table 11. PV parameters extracted from *J*(V) curves of TSC with different RL.

Ag RL thickness / nm	V_{OC} / V	J_{SC} / mA cm^{-2}	FF / %	PCE / %	N
0	1.29 (1.25 ± 0.05)	2.5 (2 ± 0.4)	26 (22 ± 3)	0.8 (0.6 ± 0.2)	8
1	1.79 (1.78 ± 0.01)	9.8 (8.7 ± 1.1)	44 (43 ± 1)	7.9 (6.9 ± 0.9)	4
2	1.77 (1.75 ± 0.04)	8.5 (8.1 ± 0.4)	45 (43 ± 1)	6.7 (6.4 ± 0.5)	6
5	1.76 (1.68 ± 0.07)	5.8 (5.3 ± 0.3)	42 (37 ± 5)	3.8 (3.3 ± 0.4)	7

3.3.2. HTL variation

In Figure 34 and Table 12, the PV parameters of TSC with various HTL in the ICL are shown. Two different MoO_x thicknesses (10 and 20 nm) were tested beneath three different PEDOT variations and one control group without PEDOT (w/o): PEDOT:PSS suspension in water (Al4083), IPA dilution of Al4083 (dil. Al4083) and Solar 3 with TritonX-100 post-treatment. The performance of cells with Al4083 is generally poor (PCE <1 %), but it slightly increases with MoO_x layer thickness. This demonstrates the detrimental effect of water on the perovskite layer, which leads to a

degradation of its properties[113,114]. Diluting Al4083 with IPA improves compatibility with the perovskite subcell, as evidenced by increased PCE. However, a 20 nm thick MoO_x blocking layer is necessary to achieve comparable results to Solar 3 cells. This suggests that the thicker MoO_x layer provides additional protection from water, thereby enhancing the performance of cells using a PEDOT suspension in water. Cells with Solar 3 and cells without PEDOT generally exhibit decreased performance with thicker MoO_x layers. This is attributed to the limited charge carrier mobility of MoO_x, which leads to charge transport issues, charge accumulation, and non-radiative recombination[126].

The best cells in this study are those without any PEDOT on top of a 10 nm MoO_x layer, achieving a PCE of 10.4 %, a V_{OC} of 1.86V, a J_{SC} of 9.9 mA cm^{-2}, and a FF of 55 %. The voltage loss is 0.06V compared to the individual subcell, which is rather low. The performance improvement compared to Solar 3 cells on top of a 10 nm MoO_x layer (V_{OC} = 1.78 V, J_{SC} = 8.7 mA cm^{-2}, FF = 43 %, PCE = 6.9 %) is primarily due to the absence of an S-shape in the J(V) curve (Figure 35). This S-shape indicates charge transport problems at an interface, likely the MoO_x/PEDOT interface, since it is not observed without the PEDOT layer. The energy levels of MoO_x and PEDOT (Solar 3 or Al4083) may not be aligned properly, which causes an energy barrier and thus the ICL acting as a counter diode. However, in single OSC with the MoO_x/Solar 3 interface (Figure 28, Section 3.2.2.), these issues are not observed. This could be due to incomplete coverage of MoO_x on the ITO leading to direct contact of PEDOT to ITO bypassing MoO_x.

Another potential cause of the S-shape is solvent penetration (toluene or water from PEDOT suspensions) through the MoO_x layer, which may lead to degradation and partial or complete dissolution of the PCBM and BCP layers. Hailegnaw et al. found that direct contact between PCBM and Ag creates and energy barrier, causing subsequent charge transport issues at the PCBM/Ag interface[82]. These effects might be mitigated when the PTB7-Th:IEICO-4F layer is spin-coated directly on MoO_x.

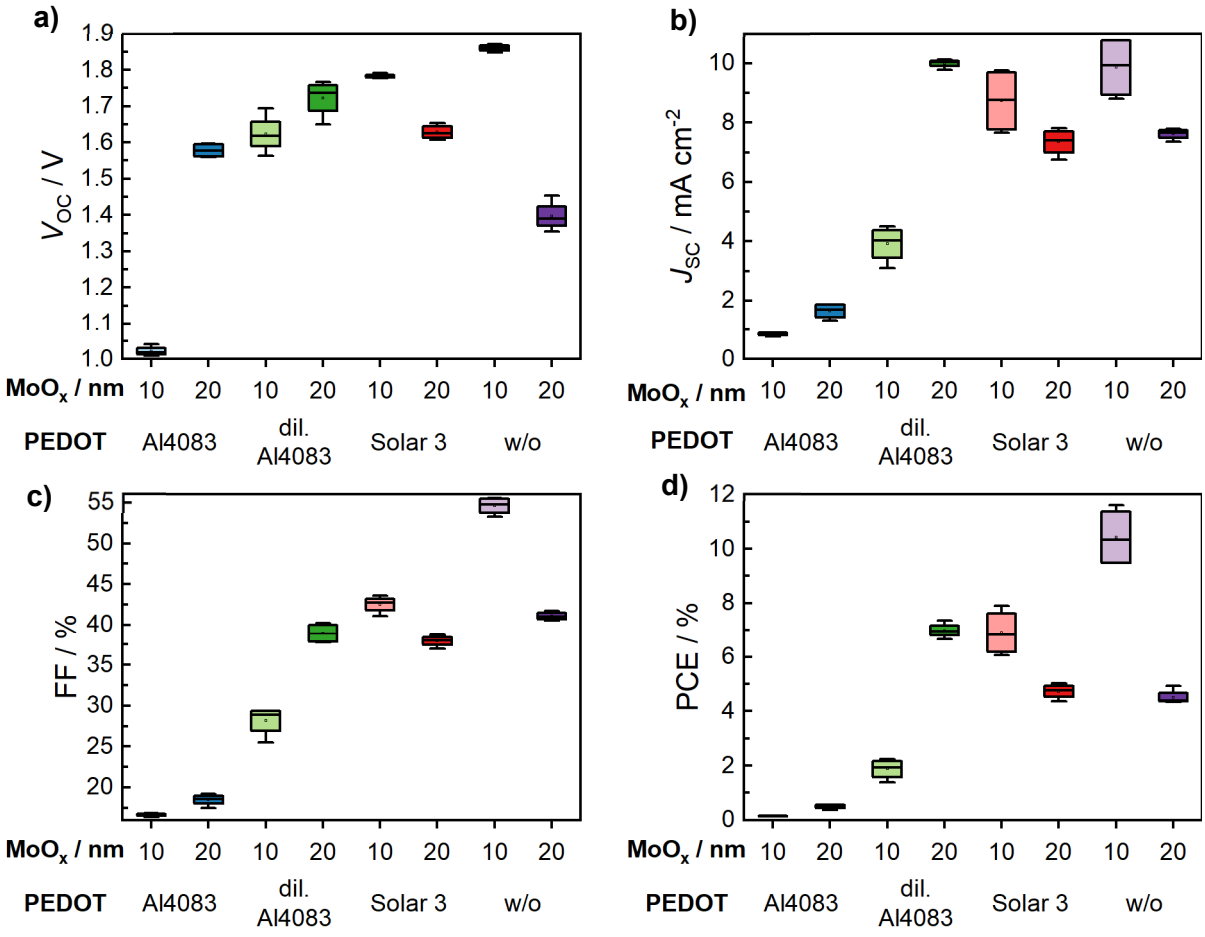

Figure 34. Box plot diagrams with PV parameters extracted from *J*(V) curves of perovskite organic TSC with three PEDOT variations and one without PEDOT (w/o) processed on top of cells with 10 and 20 nm MoO_x with **a)** V_{OC} **b)** J_{SC} **c)** FF and **d)** PCE.

Table 12. PV parameters extracted from *J*(V) curves of perovskite organic TSC with three PEDOT variations and one without PEDOT (w/o) processed on top of cells with 10 and 20 nm MoO_x.(N = 4)

PEDOT variant	MoO_x layer thickness / nm	V_{OC} / V	J_{SC} / mA cm^{-2}	FF / %	PCE / %
Al4083	10	1.04 (1.02 ± 0.01)	0.9 (0.8 ± 0.1)	17 (17 ± 0)	0.2 (0.2 ± 0)
	20	1.60 (1.58 ± 0.02)	1.9 (1.6 ± 0.3)	19 (18 ± 1)	0.6 (0.5 ± 0.1)
dil. Al4083	10	1.70 (1.62 ± 0.05)	4.5 (3.9 ± 0.6)	29 (28 ± 2)	2.2 (1.9 ± 0.4)
	20	1.77 (1.72 ± 0.05)	10.1 (10.0 ± 0.1)	40 (39 ± 1)	7.4 (7.0 ± 0.3)
Solar 3 + Triton	10	1.79 (1.78 ± 0.01)	9.8 (8.7 ± 1.1)	44 (43 ± 1)	7.9 (6.9 ± 0.9)
	20	1.65 (1.63 ± 0.02)	7.8 (7.4 ± 0.5)	39 (38 ± 1)	5.0 (4.7 ± 0.3)
w/o	10	1.87 (1.86 ± 0.01)	10.8 (9.9 ± 1.1)	56 (55 ± 1)	11.6 (10.4 ± 1.1)
	20	1.45 (1.40 ± 0.05)	7.8 (7.6 ± 0.2)	42 (41 ± 1)	4.9 (4.6 ± 0.3)

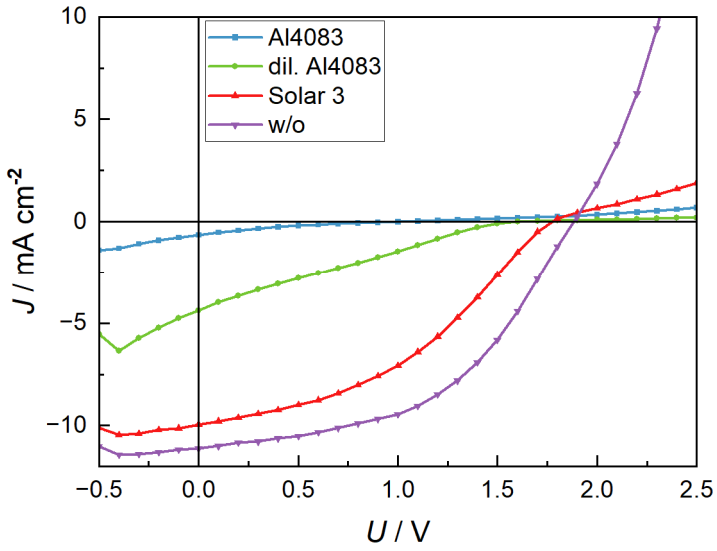

Figure 35. *J*(V) curves of perovskite organic TSC with three PEDOT variations and one without PEDOT (w/o) processed on top of cells with 10 nm MoO_x.

Despite, significant improvements in TSC performance, the record efficiency (11.6 %) remains notably lower than that of single WBG PSC (15.1 %). Three potential reasons for this disparity have been identified.

First, there is a current mismatch between the subcells. While the perovskite front cell delivers a J_{SC} of at least 13.9 mA cm^{-2} (as measured by EQE), the organic subcell may not be capable of matching this current, since the single cells are not fully optimized. In such cases, electrons from the perovskite accumulate at the interface between the HTL and the RL, or even migrate back to the HTL of the front subcell, ultimately recombining with holes. This mismatch reduces the overall J_{SC}. Additionally, the high optical losses through the RL may exacerbate these shortcomings.

Second, the perovskite subcell may sustain damage during processing of the ICL and rear subcell. Risks include solvent penetration through the ICL, potentially degrading the ETL of the perovskite subcell. Furthermore, high temperatures or mechanical stress associated with the evaporation process could cause physical damage or structural changes in the perovskite subcell. This would compromise its functionality and reducing device performance. Mechanical stress during processing could also impact the perovskite subcell, and further decrease device performance.

Third, the surface morphology of the ICL may not be ideal for processing the OSC. As described in Section 3.1.3. , the peak-to-valley height of the perovskite film is 100 nm. The PCBM and BCP layer have a combined thickness of 115 nm, theoretically sufficient to cover all the peaks of the perovskite. However, microscope images taken after processing the PEDOT variants (Figure 36) reveal round defects in both the PEDOT variants and the configuration without PEDOT. These defects may result from peaks of the perovskite layer protruding through all the layers. This could create shunt paths that decrease the parallel resistance and subsequently the FF. Furthermore,

the increased roughness of the ICL influences the morphology and quality of the organic subcell, which further influences the performance.

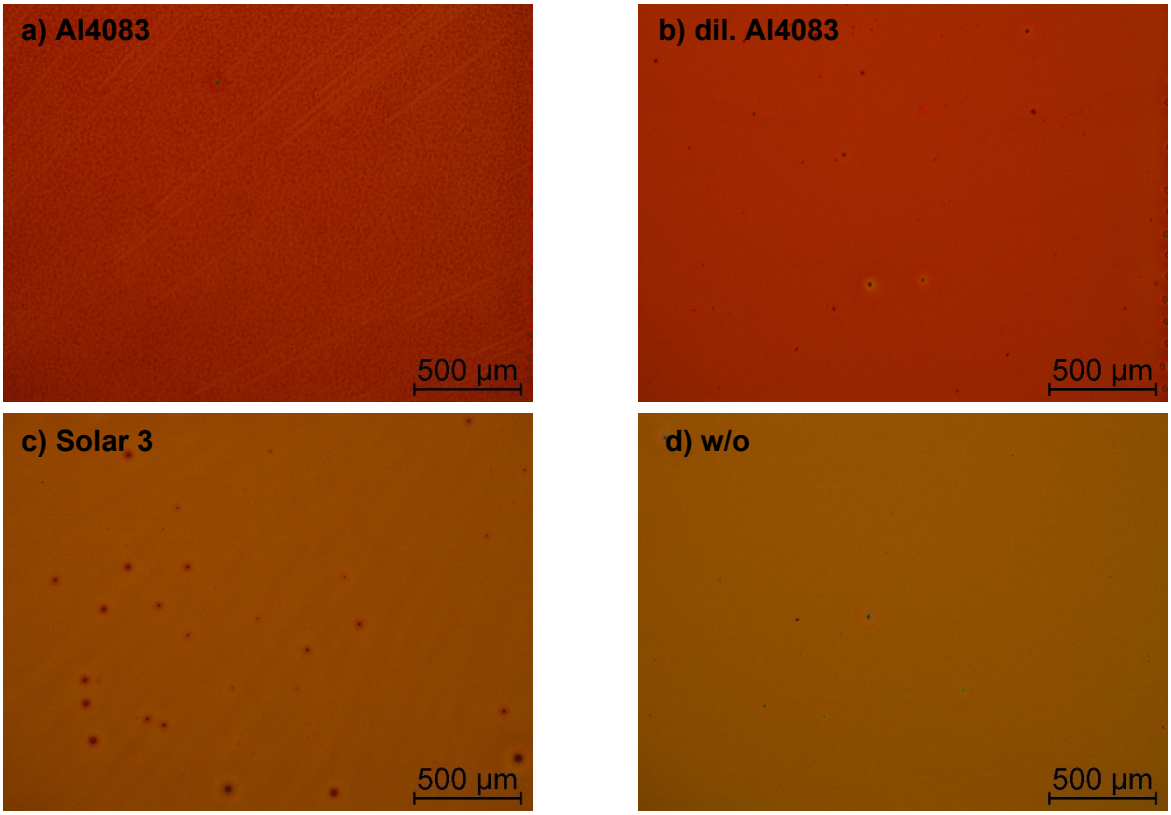

Figure 36. Microscope images of the ICL of processed on top of a WBG PSC with a PEDOT variation deposited at last with **a)** PEDOT Al4083 **b)** with IPA diluted Al4083 (1:3, dil. Al4083) **c)** PEDOT Solar 3 **d)** without PEDOT (w/o).

4. Conclusion and Outlook

To construct efficient perovskite organic tandem solar cells several conditions have to be fulfilled. The individual subcells need optimization with minimal V_{OC} loss. Furthermore, the interconnecting layer must be well-designed, and the band gaps of the HTL and ETL well aligned. The recombination layer between them should provide high transparency and allow efficient carrier recombination. In this study, a wide band gap perovskite subcell with a device structure ITO/MeO-2PACz/$FA_{0.8}Cs_{0.2}Pb(I_{0.5}Br_{0.5})_3$/PCBM/BCP was tested. Cells achieved a high average performance (V_{OC} = 1.22 V, J_{SC} = 14.7 mA cm^{-2}, FF = 77 %, PCE = 13.9 %), with a low V_{OC} deficit (0.62 V) and high EQE of 82 to 67 % in the range of 350 to 650 nm by adding MACl and post-treating with PEAI. Perovskite films of this type show a high grain size (D_a = 0.39 µm), low average roughness (R_a = 8.4 nm) with a high absorptance of 56 - 82 % between 350 and 680 nm. Furthermore, the films show an increased steady-state PL signal, indicating reduced non-radiative recombination. Time-dependent measurement of the V_{OC} and the PL signal of perovskite solar cells reveal the formation of a second red shifted PL peak at 775 nm attributed light-induced phase segregation and the formation of an iodide-rich perovskite phase. This effect caused a V_{OC} reduction of 22 mV over 15 minutes, which was reversible after storage in darkness. To enable measurement of perovskite solar cells outside the glovebox, a protective SiO_x layer was deposited, which significantly increased the storage stability of the cells under ambient conditions (>80 % of initial PCE after 2500 h). Furthermore, the temperature and solvent stability of unprotected perovskite cells were tested to assess the constraints of top processing the organic subcell. The cells remained stable up to 100 °C and were resistant to exposure to various alcohols, but were damaged by the apolar solvents toluene, CB, CF, and by DMSO.

To ensure compatibility of the organic subcell, the water-free PEDOT variant, Solar 3, was used as the HTL. Solar 3 required optimization, which was performed with a model OSC based on P3HT:PCBM. Thereby, a post-treatment with a 1 vol% TritonX-100 solution in IPA significantly enhanced the performance of the cells. The results were transferred to the PTB7-Th:IEICO-4F OSCs, used in the tandem cells. Cells with the optimized Solar 3 achieved moderate performance (V_{OC} = 0.72 V, J_{SC} = 16.5 mA cm^{-2}, FF = 62 PCE = 7.4 %). Nevertheless, a high absorptance (up to 55 %) and EQE of around 50 % have been achieved in the NIR, which is complementary to the perovskite subcell absorption.

Perovskite organic TSC with discussed subcells were fabricated with different ICLs. A ICL based on PCBM/BCP/Ag/Solar 3 proved to only work, if a MoO_x layer is inserted between the Ag and Solar 3. MoO_x effectively prevented the dissolution of PCBM by toluene in the Solar 3 suspension, preserving the interconnecting layer. Thickness variation of the Ag recombination layer revealed an optimum at 1 nm. The J_{SC} of cells with no RL, as well as a 5 nm Ag RL, decreases, which is probably caused by inefficient recombination and optical losses. Nevertheless, an ohmic contact

is not formed, since cells exhibit a pronounced S-shape in the *J*(V) curve, indicating charge transport issues at an interface. Omitting the Solar 3 layer and processing the active layer directly on MoO_x resolved this issue. A misalignment of the energy levels of Solar 3 and MoO_x, which is creating an energy barrier, might be the reason for this. Champion devices with this ICL (PCBM/BCP/AG/MoO_x) achieved a high V_{OC} of 1.87 V with low voltage loss (0.05 V) compared to the sum of the single cells, but an efficiency of only 11.6 %. The moderate device performance may be attributed to several factors, including photocurrent mismatch of the subcells, damaging of the perovskite subcell during subsequent layer processing and suboptimal surface morphology of the interconnecting layer.

Appendix

Table 13. Resistance measurement of laser patterned ITO substrates with different laser power and speed.

Laser speed / %	Laser power / %			
	1	2	4	10
2	13.4 kΩ	13.1 kΩ	23.7 kΩ	9 320 kΩ
8	3.33 kΩ	500 kΩ	2 580 kΩ	69 200 kΩ
14	0.200 kΩ	0.269 kΩ	10.8 kΩ	110 000 kΩ
20	0.149 kΩ	0.414 kΩ	O.L.	O.L.

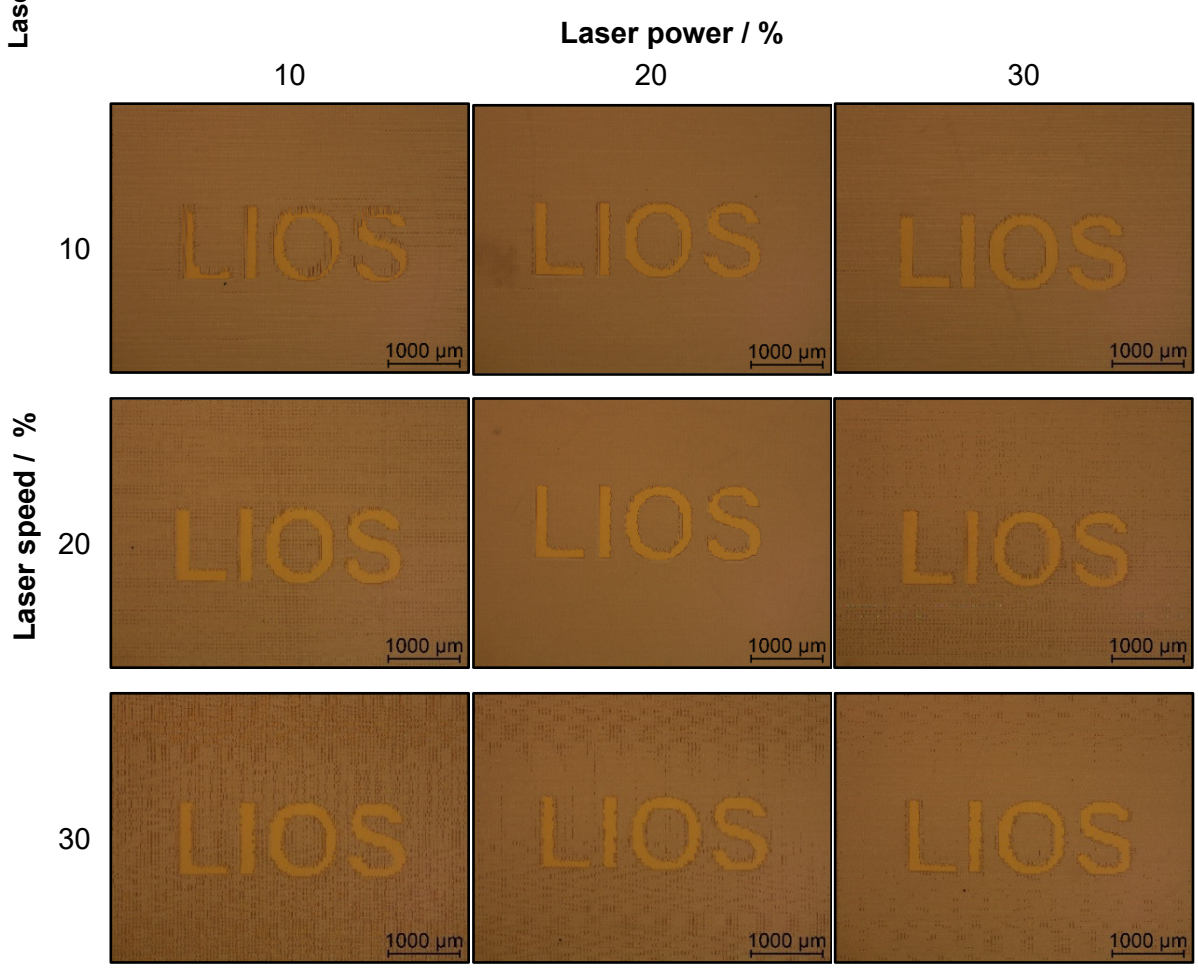

Figure 37. Microscope images of laser patterned ITO with different laser power and speed.

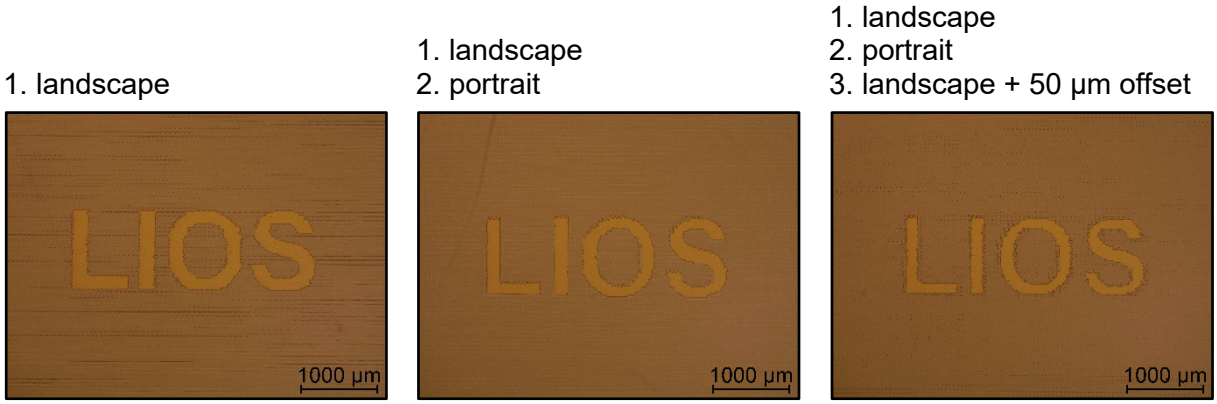

Figure 38. Microscope images of laser patterned ITO substrates (laser power = 20 %, laser speed = 20 %) with successive steps with different laser directions and an offset.

Table 14. PV parameters extracted from J(V) measurements of P3HT:PCBM cells with different post-treatments of Solar 3.

Treatment	V_{OC} / V	J_{SC} / mA cm^{-2}	FF / %	PCE / %	N
Al4083	0.55 (0.51 ± 0.03)	8 (7.5 ± 0.3)	54 (52 ± 1)	2.3 (2.0 ± 0.1)	20
w/o	0.2 (0.18 ± 0.03)	6.9 (5.9 ± 0.7)	27 (25 ± 3)	0.3 (0.3 ± 0.1)	6
IPA	0.31 (0.29 ± 0.02)	5.8 (5.6 ± 0.3)	35 (34 ± 1)	0.6 (0.6 ± 0.1)	5
MeOH	0.5 (0.47 ± 0.03)	7 (6.2 ± 0.6)	54 (49 ± 4)	1.9 (1.5 ± 0.3)	6
Butanole	0.48 (0.44 ± 0.02)	7.7 (6.9 ± 0.6)	54 (52 ± 1)	1.9 (1.6 ± 0.2)	15
1 vol% DMSO	0.45 (0.42 ± 0.02)	6.3 (5.9 ± 0.3)	54 (53 ± 1)	1.5 (1.3 ± 0.2)	5
5 vol% DMSO	0.47 (0.45 ± 0.02)	7.3 (7.1 ± 0.2)	53 (50 ± 3)	1.7 (1.6 ± 0.2)	6
DMSO	0.5 (0.48 ± 0.01)	6.7 (6.3 ± 0.2)	53 (51 ± 1)	1.7 (1.5 ± 0.1)	6
1. DMSO 2. MeOH	0.5 (0.48 ± 0.02)	8 (7.6 ± 0.4)	52 (51 ± 1)	1.9 (1.9 ± 0.1)	9
5 vol% Zonyl	0.5 (0.48 ± 0.01)	7.6 (7.0 ± 0.5)	52 (50 ± 2)	1.9 (1.7 ± 0.2)	9
1 vol% TritonX-100	0.47 (0.47 ± 0.01)	6.9 (6.7 ± 0.2)	52 (51 ± 1)	1.6 (1.6 ± 0.1)	6
5 vol% TritonX-100	0.53 (0.52 ± 0.02)	7.5 (7.1 ± 0.2)	54 (52 ± 2)	2.1 (1.9 ± 0 .1)	8
1 vol% EMIM-FSI	0.38 (0.37 ± 0.01)	6 (6.0 ± 0.1)	52 (51 ± 1)	1.2 (1.1 ± 0)	3
1 vol% BMPyrr-FSI	0.39 (0.35 ± 0.03)	5.6 (5.5 ± 0.1)	57 (49 ± 7)	1.2 (1.0 ± 0.2)	6
1 vol% EMIM-BF4	0.42 (0.34 ± 0.08)	6.5 (6.0 ± 0.5)	52 (42 ± 9)	1.4 (0.9 ± 0.4)	5

List of abbreviations

A	Acceptor
AFM	Atomic force spectroscopy
BCP	Bathocuproine
CB	Chlorobenzene
CF	Chloroform
D	Donor
DMF	Dimethylformamide
DMSO	Dimethyl sulfoxide
E_g	Band gap
EL	Electroluminescence
EQE	External quantum efficiency
ETL	Electron transport layer
EtOH	Ethanol
FA	Formamidinium
FF	Fill factor
HOMO	Highest occupied molecule orbital
HTL	Hole transport layer
ICL	Interconnecting layer
IEICO-4F	2,2'-((2Z,2'Z)-(((4,4,9,9-tetrakis(4-hexylphenyl)-4,9-dihydro-sindaceno[1,2-b:5,6-b']dithiophene-2,7-diyl)bis(4-((2-ethylhexyl)oxy)thiophene-5,2-diyl))bis(methanylylidene))bis(5,6-difluoro-3-oxo-2,3-dihydro-1H-indene-2,1-diylidene))dimalononitrile
IPA	2-propanol
ITO	Indium tin oxide
J(V)	Current density voltage curve
J_{SC}	Short-circuit current density
LUMO	Lowest occupied molecule orbital
MA	Methylammonium
MeO-2PACz	(2-(3,6-Dimethoxy-9H-carbazol-9-yl)ethyl)phosphonic acid
NIR	Near-infrared
NMP	*N*-methyl-2-pyrrolidone
OSC	Organic solar cell
P3HT	Poly(3-hexylthiophene-2,5-diyl)
PCBM	[6,6]-Phenyl-C61-butyric acid methyl ester
PCE	Power conversion efficiency
PDIN	N,N'-Bis[3-(dimethylamino)propyl]perylene-3,4,9,10-tetracarboxylic diimide
PEAI	Phenethylammonium iodide
PEDOT:PSS	Poly(3,4-ethylenedioxythiophene):poly(styrenesulfonate)
PL	Photoluminescence
PMMA	Poly(methyl methacrylate)
PS	Polystyrol
PSC	Perovskite solar cell
PTB7-Th	Poly[4,8-bis(5-(2-ethylhexyl)thiophen-2-yl)benzo[1,2-b;4,5-b']dithiophene-2,6-diyl-alt-(4-(2-ethylhexyl)-3-fluorothieno[3,4-b]thiophene-)-2-carboxylate-2-6-diyl]
PV	Photovoltaic
RL	Recombination layer
TCO	Transparent conductive oxide
THF	Tetrahydrofuran
TSC	Tandem solar cell
V_{OC}	Open-circuit voltage
WBG	Wide band gap

List of Figures

List of Tables

References

[1] S. Philipps, *Photovoltaics Report*, Freiburg **2023**.
[2] *Best Research-Cell Efficiencies*, https://www.nrel.gov/pv/cell-efficiency.html.
[3] A. Richter, M. Hermle, S. W. Glunz, *IEEE J. Photovoltaics* **2013**, *3*, 1184.
[4] M. Takla, N. E. Kamfjord, H. Tveit, S. Kjelstrup, *Energy* **2013**, *58*, 138.
[5] P. Kowalczewski, L. C. Andreani, *Solar Energy Materials and Solar Cells* **2015**, *143*, 260.
[6] J. Guo, J. Min, *Advanced Energy Materials* **2019**, *9*.
[7] R. Sun, Q. Wu, J. Guo, T. Wang, Y. Wu, B. Qiu, Z. Luo, W. Yang, Z. Hu, J. Guo, M. Shi, C. Yang, F. Huang, Y. Li, J. Min, *Joule* **2020**, *4*, 407.
[8] N.-G. Park, K. Zhu, *Nat Rev Mater* **2020**, *5*, 333.
[9] Z. Li, T. R. Klein, D. H. Kim, M. Yang, J. J. Berry, M. F. A. M. van Hest, K. Zhu, *Nat Rev Mater* **2018**, *3*.
[10] R. J. Sutton, G. E. Eperon, L. Miranda, E. S. Parrott, B. A. Kamino, J. B. Patel, M. T. Hörantner, M. B. Johnston, A. A. Haghighirad, D. T. Moore, H. J. Snaith, *Advanced Energy Materials* **2016**, *6*.
[11] B. Hailegnaw, S. Demchyshyn, C. Putz, L. E. Lehner, F. Mayr, D. Schiller, R. Pruckner, M. Cobet, D. Ziss, T. M. Krieger, A. Rastelli, N. S. Sariciftci, M. C. Scharber, M. Kaltenbrunner, *Nat Energy* **2024**.
[12] P. Würfel, U. Würfel, *Physics of solar cells: From basic principles to advanced concepts*, Wiley-VCH Verlag GmbH & Co. KGaA, Weinheim **2016**.
[13] L. C. Hirst, N. J. Ekins-Daukes, *Progress in Photovoltaics* **2011**, *19*, 286.
[14] W. Shockley, H. J. Queisser, *Journal of Applied Physics* **1961**, *32*, 510.
[15] K. O. Brinkmann, T. Becker, F. Zimmermann, C. Kreusel, T. Gahlmann, M. Theisen, T. Haeger, S. Olthof, C. Tückmantel, M. Günster, T. Maschwitz, F. Göbelsmann, C. Koch, D. Hertel, P. Caprioglio, F. Peña-Camargo, L. Perdigón-Toro, A. Al-Ashouri, L. Merten, A. Hinderhofer, L. Gomell, S. Zhang, F. Schreiber, S. Albrecht, K. Meerholz, D. Neher, M. Stolterfoht, T. Riedl, *Nature* **2022**, *604*, 280.
[16] J. Hai, W. Zhao, S. Luo, H. Yu, H. Chen, Z. Lu, L. Li, Y. Zou, H. Yan, *Dyes and Pigments* **2021**, *188*, 109171.
[17] A. Kojima, K. Teshima, Y. Shirai, T. Miyasaka, *Journal of the American Chemical Society* **2009**, *131*, 6050.
[18] Y. Tong, A. Najar, Le Wang, L. Liu, M. Du, J. Yang, J. Li, K. Wang, S. F. Liu, *Advanced science (Weinheim, Baden-Wurttemberg, Germany)* **2022**, *9*, e2105085.
[19] A. M. A. Leguy, P. Azarhoosh, M. I. Alonso, M. Campoy-Quiles, O. J. Weber, J. Yao, D. Bryant, M. T. Weller, J. Nelson, A. Walsh, M. van Schilfgaarde, P. R. F. Barnes, *Nanoscale* **2016**, *8*, 6317.
[20] B. Conings, J. Drijkoningen, N. Gauquelin, A. Babayigit, J. D'Haen, L. D'Olieslaeger, A. Ethirajan, J. Verbeeck, J. Manca, E. Mosconi, F. de Angelis, H.-G. Boyen, *Advanced Energy Materials* **2015**, *5*.
[21] J. M. Frost, K. T. Butler, F. Brivio, C. H. Hendon, M. van Schilfgaarde, A. Walsh, *Nano letters* **2014**, *14*, 2584.
[22] D. P. McMeekin, G. Sadoughi, W. Rehman, G. E. Eperon, M. Saliba, M. T. Hörantner, A. Haghighirad, N. Sakai, L. Korte, B. Rech, M. B. Johnston, L. M. Herz, H. J. Snaith, *Science (New York, N.Y.)* **2016**, *351*, 151.
[23] Z. Liu, L. Krückemeier, B. Krogmeier, B. Klingebiel, J. A. Márquez, S. Levcenko, S. Öz, S. Mathur, U. Rau, T. Unold, T. Kirchartz, *ACS Energy Lett.* **2019**, *4*, 110.
[24] K. Gugujonović, F. Mayr, B. Hailegnaw, S. Pöllner, R. Zahrhuber, A. Planer, C.-H. Wang, C.-S. Hsu, M. C. Scharber, *Monatsh Chem* **2023**.
[25] W.-J. Yin, T. Shi, Y. Yan, *Applied Physics Letters* **2014**, *104*.
[26] N. Wu, Y. Wu, D. Walter, H. Shen, T. Duong, D. Grant, C. Barugkin, X. Fu, J. Peng, T. White, K. Catchpole, K. Weber, *Energy Tech* **2017**, *5*, 1827.

[27] M. Stolterfoht, P. Caprioglio, C. M. Wolff, J. A. Márquez, J. Nordmann, S. Zhang, D. Rothhardt, U. Hörmann, Y. Amir, A. Redinger, L. Kegelmann, F. Zu, S. Albrecht, N. Koch, T. Kirchartz, M. Saliba, T. Unold, D. Neher, *Energy Environ. Sci.* **2019**, *12*, 2778.
[28] J. Wang, W. Fu, S. Jariwala, I. Sinha, A. K.-Y. Jen, D. S. Ginger, *ACS Energy Lett.* **2019**, *4*, 222.
[29] F. Peña-Camargo, P. Caprioglio, F. Zu, E. Gutierrez-Partida, C. M. Wolff, K. Brinkmann, S. Albrecht, T. Riedl, N. Koch, D. Neher, M. Stolterfoht, *ACS Energy Lett.* **2020**, *5*, 2728.
[30] S. Draguta, O. Sharia, S. J. Yoon, M. C. Brennan, Y. V. Morozov, J. S. Manser, P. V. Kamat, W. F. Schneider, M. Kuno, *Nature communications* **2017**, *8*, 200.
[31] R. G. Balakrishna, S. M. Kobosko, P. V. Kamat, *ACS Energy Lett.* **2018**, *3*, 2267.
[32] E. T. Hoke, D. J. Slotcavage, E. R. Dohner, A. R. Bowring, H. I. Karunadasa, M. D. McGehee, *Chemical science* **2015**, *6*, 613.
[33] A. Solanki, P. Yadav, S.-H. Turren-Cruz, S. S. Lim, M. Saliba, T. C. Sum, *Nano Energy* **2019**, *58*, 604.
[34] X. Zheng, B. Chen, J. Dai, Y. Fang, Y. Bai, Y. Lin, H. Wei, X. C. Zeng, J. Huang, *Nat Energy* **2017**, *2*.
[35] S. D. Stranks, G. E. Eperon, G. Grancini, C. Menelaou, M. J. P. Alcocer, T. Leijtens, L. M. Herz, A. Petrozza, H. J. Snaith, *Science (New York, N.Y.)* **2013**, *342*, 341.
[36] J. Wang, J. Zhang, Y. Zhou, H. Liu, Q. Xue, X. Li, C.-C. Chueh, H.-L. Yip, Z. Zhu, A. K. Y. Jen, *Nature communications* **2020**, *11*, 177.
[37] X. Wu, M. T. Trinh, D. Niesner, H. Zhu, Z. Norman, J. S. Owen, O. Yaffe, B. J. Kudisch, X.-Y. Zhu, *Journal of the American Chemical Society* **2015**, *137*, 2089.
[38] S. Mahesh, J. M. Ball, R. D. J. Oliver, D. P. McMeekin, P. K. Nayak, M. B. Johnston, H. J. Snaith, *Energy Environ. Sci.* **2020**, *13*, 258.
[39] B. Chen, Z. Yu, K. Liu, X. Zheng, Y. Liu, J. Shi, D. Spronk, P. N. Rudd, Z. Holman, J. Huang, *Joule* **2019**, *3*, 177.
[40] S. Wang, Z. Ma, B. Liu, W. Wu, Y. Zhu, R. Ma, C. Wang, *Solar RRL* **2018**, *2*.
[41] X. Shen, B. M. Gallant, P. Holzhey, J. A. Smith, K. A. Elmestekawy, Z. Yuan, P. V. G. M. Rathnayake, S. Bernardi, A. Dasgupta, E. Kasparavicius, T. Malinauskas, P. Caprioglio, O. Shargaieva, Y.-H. Lin, M. M. McCarthy, E. Unger, V. Getautis, A. Widmer-Cooper, L. M. Herz, H. J. Snaith, *Advanced materials (Deerfield Beach, Fla.)* **2023**, *35*, e2211742.
[42] Q. Jiang, Y. Zhao, X. Zhang, X. Yang, Y. Chen, Z. Chu, Q. Ye, X. Li, Z. Yin, J. You, *Nat. Photonics* **2019**, *13*, 460.
[43] C. Chen, Z. Song, C. Xiao, R. A. Awni, C. Yao, N. Shrestha, C. Li, S. S. Bista, Y. Zhang, L. Chen, R. J. Ellingson, C.-S. Jiang, M. Al-Jassim, G. Fang, Y. Yan, *ACS Energy Lett.* **2020**, *5*, 2560.
[44] N. J. Jeon, J. H. Noh, Y. C. Kim, W. S. Yang, S. Ryu, S. I. Seok, *Nature materials* **2014**, *13*, 897.
[45] L. E. Lehner, S. Demchyshyn, K. Frank, A. Minenkov, D. J. Kubicki, H. Sun, B. Hailegnaw, C. Putz, F. Mayr, M. Cobet, G. Hesser, W. Schöfberger, N. S. Sariciftci, M. C. Scharber, B. Nickel, M. Kaltenbrunner, *Advanced materials (Deerfield Beach, Fla.)* **2023**, *35*, e2208061.
[46] F. Zheng, C. Zuo, M. Niu, C. Zhou, S. J. Bradley, C. R. Hall, W. Xu, X. Wen, X. Hao, M. Gao, T. A. Smith, K. P. Ghiggino, *ACS applied materials & interfaces* **2020**, *12*, 25980.
[47] H. Yu, F. Wang, F. Xie, W. Li, J. Chen, N. Zhao, *Adv Funct Materials* **2014**, *24*, 7102.
[48] J.-W. Lee, H.-S. Kim, N.-G. Park, *Accounts of chemical research* **2016**, *49*, 311.
[49] D. Song, S. Narra, M.-Y. Li, J.-S. Lin, E. W.-G. Diau, *ACS Energy Lett.* **2021**, *6*, 4179.
[50] C. K. Chiang, C. R. Fincher, Y. W. Park, A. J. Heeger, H. Shirakawa, E. J. Louis, S. C. Gau, A. G. MacDiarmid, *Phys. Rev. Lett.* **1977**, *39*, 1098.
[51] H. Spanggaard, F. C. Krebs, *Solar Energy Materials and Solar Cells* **2004**, *83*, 125.

[52] H. Shirakawa, E. J. Louis, A. G. MacDiarmid, C. K. Chiang, A. J. Heeger, *J. Chem. Soc., Chem. Commun.* **1977**.
[53] G. Yu, J. Gao, J. C. Hummelen, F. Wudl, A. J. Heeger, *Science (New York, N.Y.)* **1995**, *270*, 1789.
[54] H. Hoppe, N. S. Sariciftci, *J. Mater. Res.* **2004**, *19*, 1924.
[55] M. T. Dang, L. Hirsch, G. Wantz, *Advanced materials (Deerfield Beach, Fla.)* **2011**, *23*, 3597.
[56] W. Ma, C. Yang, X. Gong, K. Lee, A. J. Heeger, *Adv Funct Materials* **2005**, *15*, 1617.
[57] W. Zhao, S. Zhang, J. Hou, *Sci. China Chem.* **2016**, *59*, 1574.
[58] Y. Cui, H. Yao, J. Zhang, T. Zhang, Y. Wang, L. Hong, K. Xian, B. Xu, S. Zhang, J. Peng, Z. Wei, F. Gao, J. Hou, *Nature communications* **2019**, *10*, 2515.
[59] R. Jin, F. Wang, R. Guan, X. Zheng, T. Zhang, *Molecular Physics* **2017**, *115*, 1591.
[60] H. Yao, Y. Cui, R. Yu, B. Gao, H. Zhang, J. Hou, *Angewandte Chemie (International ed. in English)* **2017**, *56*, 3045.
[61] D. Baran, R. S. Ashraf, D. A. Hanifi, M. Abdelsamie, N. Gasparini, J. A. Röhr, S. Holliday, A. Wadsworth, S. Lockett, M. Neophytou, C. J. M. Emmott, J. Nelson, C. J. Brabec, A. Amassian, A. Salleo, T. Kirchartz, J. R. Durrant, I. McCulloch, *Nature materials* **2017**, *16*, 363.
[62] Z. Hu, Z. Wang, F. Zhang, *J. Mater. Chem. A* **2019**, *7*, 7025.
[63] X. Song, N. Gasparini, L. Ye, H. Yao, J. Hou, H. Ade, D. Baran, *ACS Energy Lett.* **2018**, *3*, 669.
[64] J. Wang, S. Xie, D. Zhang, R. Wang, Z. Zheng, H. Zhou, Y. Zhang, *J. Mater. Chem. A* **2018**, *6*, 19934.
[65] Y. Tang, H. Sun, Z. Wu, Y. Zhang, G. Zhang, M. Su, X. Zhou, X. Wu, W. Sun, X. Zhang, B. Liu, W. Chen, Q. Liao, H. Y. Woo, X. Guo, *Advanced science (Weinheim, Baden-Wurttemberg, Germany)* **2019**, *6*, 1901773.
[66] E. Köhnen, M. Jošt, A. B. Morales-Vilches, P. Tockhorn, A. Al-Ashouri, B. Macco, L. Kegelmann, L. Korte, B. Rech, R. Schlatmann, B. Stannowski, S. Albrecht, *Sustainable Energy Fuels* **2019**, *3*, 1995.
[67] H. Aqoma, I. F. Imran, F. T. A. Wibowo, N. V. Krishna, W. Lee, A. K. Sarker, Y. Du Ryu, S.-Y. Jang, *Advanced Energy Materials* **2020**, *10*.
[68] A. R. Bin, M. Yusoff, J. Jang, *Chemical communications (Cambridge, England)* **2016**, *52*, 5824.
[69] C.-C. Chen, S.-H. Bae, W.-H. Chang, Z. Hong, G. Li, Q. Chen, H. Zhou, Y. Yang, *Mater. Horiz.* **2015**, *2*, 203.
[70] X. Chen, Z. Jia, Z. Chen, T. Jiang, L. Bai, F. Tao, J. Chen, X. Chen, T. Liu, X. Xu, C. Yang, W. Shen, W. E. Sha, H. Zhu, Y. Yang, *Joule* **2020**, *4*, 1594.
[71] Z. Li, S. Wu, J. Zhang, K. C. Lee, H. Lei, F. Lin, Z. Wang, Z. Zhu, A. K. Y. Jen, *Advanced Energy Materials* **2020**, *10*.
[72] J. Liu, S. Lu, L. Zhu, X. Li, W. C. H. Choy, *Nanoscale* **2016**, *8*, 3638.
[73] T. Maksudov, M. He, S. Doukas, M. I. Nugraha, B. Adilbekova, H. Faber, L. Luo, R. Zhou, O. M. Bakr, W. Ogieglo, I. Pinnau, G. T. Harrison, D. R. Naphade, Z. Ling, E. Lidorikis, S. Fatayer, M. Heeney, F. H. Isikgor, T. D. Anthopoulos, *Materials Science and Engineering: R: Reports* **2024**, *159*, 100802.
[74] S. Qin, C. Lu, Z. Jia, Y. Wang, S. Li, W. Lai, P. Shi, R. Wang, C. Zhu, J. Du, J. Zhang, L. Meng, Y. Li, *Advanced materials (Deerfield Beach, Fla.)* **2022**, *34*, e2108829.
[75] H. Xu, L. Torres Merino, M. Koc, E. Aydin, S. Zhumagali, M. A. Haque, A. Yazmaciyan, A. Sharma, D. Rosas Villalva, L. Huerta Hernandez, M. de Bastiani, M. Babics, F. H. Isikgor, J. Troughton, S. de Wolf, S. Yerci, D. Baran, *ACS Appl. Energy Mater.* **2022**, *5*, 14035.
[76] Z. Zhang, C. Cueto, Y. Ding, Le Yu, T. P. Russell, T. Emrick, Y. Liu, *ACS applied materials & interfaces* **2022**, *14*, 29896.

[77] X. Wang, D. Zhang, B. Liu, X. Wu, X. Jiang, S. Zhang, Y. Wang, D. Gao, L. Wang, H. Wang, Z. Huang, X. Xie, T. Chen, Z. Xiao, Q. He, S. Xiao, Z. Zhu, S. Yang, *Advanced materials (Deerfield Beach, Fla.)* **2023**, *35*, e2305946.
[78] A. Rajagopal, Z. Yang, S. B. Jo, I. L. Braly, P.-W. Liang, H. W. Hillhouse, A. K.-Y. Jen, *Advanced materials (Deerfield Beach, Fla.)* **2017**, *29*.
[79] C. Ho, J. Kothari, X. Fu, F. So, *Materials Today Energy* **2021**, *21*, 100707.
[80] F. Yang, D.-W. Kang, Y.-S. Kim, *Solar Energy* **2017**, *155*, 552.
[81] V. Sarritzu, N. Sestu, D. Marongiu, X. Chang, S. Masi, A. Rizzo, S. Colella, F. Quochi, M. Saba, A. Mura, G. Bongiovanni, *Scientific reports* **2017**, *7*, 44629.
[82] B. Hailegnaw, G. Adam, H. Heilbrunner, D. H. Apaydin, C. Ulbricht, N. S. Sariciftci, M. C. Scharber, *RSC advances* **2018**, *8*, 24836.
[83] *CRC handbook of chemistry and physics: A ready-reference book of chemical and physical data*, CRC Press, Boca Raton **2014**.
[84] S. Luo, W. A. Daoud, *J. Mater. Chem. A* **2015**, *3*, 8992.
[85] V. Zardetto, B. L. Williams, A. Perrotta, F. Di Giacomo, M. A. Verheijen, R. Andriessen, W. M. M. Kessels, M. Creatore, *Sustainable Energy Fuels* **2017**, *1*, 30.
[86] M. Xiao, F. Huang, W. Huang, Y. Dkhissi, Y. Zhu, J. Etheridge, A. Gray-Weale, U. Bach, Y.-B. Cheng, L. Spiccia, *Angewandte Chemie (International ed. in English)* **2014**, *53*, 9898.
[87] H. Zhang, Q. Niu, X. Tang, H. Wang, W. Huang, R. Xia, W. Zeng, J. Yao, B. Yan, *ACS omega* **2017**, *2*, 7666.
[88] S. Meloni, T. Moehl, W. Tress, M. Franckevičius, M. Saliba, Y. H. Lee, P. Gao, M. K. Nazeeruddin, S. M. Zakeeruddin, U. Rothlisberger, M. Graetzel, *Nature communications* **2016**, *7*, 10334.
[89] P. Calado, A. M. Telford, D. Bryant, X. Li, J. Nelson, B. C. O'Regan, P. R. F. Barnes, *Nature communications* **2016**, *7*, 13831.
[90] Y. Zhong, M. Hufnagel, M. Thelakkat, C. Li, S. Huettner, *Adv Funct Materials* **2020**, *30*.
[91] S. Ravishankar, S. Gharibzadeh, C. Roldán-Carmona, G. Grancini, Y. Lee, M. Ralaiarisoa, A. M. Asiri, N. Koch, J. Bisquert, M. K. Nazeeruddin, *Joule* **2018**, *2*, 788.
[92] K. Tvingstedt, L. Gil-Escrig, C. Momblona, P. Rieder, D. Kiermasch, M. Sessolo, A. Baumann, H. J. Bolink, V. Dyakonov, *ACS Energy Lett.* **2017**, *2*, 424.
[93] H. Abdy, A. Aletayeb, M. Bashirpour, Z. Heydari, M. Kolahdouz, E. Asl-Soleimani, Z. Kolahdouz, G. Zhang, *Optik* **2019**, *191*, 100.
[94] M. Stolterfoht, C. M. Wolff, J. A. Márquez, S. Zhang, C. J. Hages, D. Rothhardt, S. Albrecht, P. L. Burn, P. Meredith, T. Unold, D. Neher, *Nat Energy* **2018**, *3*, 847.
[95] Y. Guo, S. Yuan, D. Zhu, M. Yu, H.-Y. Wang, J. Lin, Y. Wang, Y. Qin, J.-P. Zhang, X.-C. Ai, *Physical chemistry chemical physics PCCP* **2021**, *23*, 6162.
[96] D. W. deQuilettes, W. Zhang, V. M. Burlakov, D. J. Graham, T. Leijtens, A. Osherov, V. Bulović, H. J. Snaith, D. S. Ginger, S. D. Stranks, *Nature communications* **2016**, *7*, 11683.
[97] S. D. Stranks, V. M. Burlakov, T. Leijtens, J. M. Ball, A. Goriely, H. J. Snaith, *Phys. Rev. Applied* **2014**, *2*.
[98] W. Tress, M. Yavari, K. Domanski, P. Yadav, B. Niesen, J. P. Correa Baena, A. Hagfeldt, M. Graetzel, *Energy Environ. Sci.* **2018**, *11*, 151.
[99] W. Nie, J.-C. Blancon, A. J. Neukirch, K. Appavoo, H. Tsai, M. Chhowalla, M. A. Alam, M. Y. Sfeir, C. Katan, J. Even, S. Tretiak, J. J. Crochet, G. Gupta, A. D. Mohite, *Nature communications* **2016**, *7*, 11574.
[100] A. R. Kirmani, D. P. Ostrowski, K. T. VanSant, T. A. Byers, R. C. Bramante, K. N. Heinselman, J. Tong, B. Stevens, W. Nemeth, K. Zhu, I. R. Sellers, B. Rout, J. M. Luther, *Nat Energy* **2023**, *8*, 191.

[101] Q. Meng, Y. Chen, Y. Y. Xiao, J. Sun, X. Zhang, C. B. Han, H. Gao, Y. Zhang, H. Yan, *J Mater Sci: Mater Electron* **2021**, *32*, 12784.
[102] E. M. Sanehira, B. J. Tremolet de Villers, P. Schulz, M. O. Reese, S. Ferrere, K. Zhu, L. Y. Lin, J. J. Berry, J. M. Luther, *ACS Energy Lett.* **2016**, *1*, 38.
[103] D. M. Torres-Herrera, P. M. Moreno-Romero, D. Cabrera-German, H. J. Cortina-Marrero, M. Sotelo-Lerma, H. Hu, *Solar Energy* **2020**, *206*, 136.
[104] Z. Shi, H. Liu, J. Li, F. Wang, Y. Bai, X. Bian, B. Zhang, A. Alsaedi, T. Hayat, Z. Tan, *Solar Energy Materials and Solar Cells* **2018**, *180*, 1.
[105] K. Chen, Q. Hu, T. Liu, L. Zhao, D. Luo, J. Wu, Y. Zhang, W. Zhang, F. Liu, T. P. Russell, R. Zhu, Q. Gong, *Advanced materials (Deerfield Beach, Fla.)* **2016**, *28*, 10718.
[106] W. Chen, G. Zhang, L. Xu, R. Gu, Z. Xu, H. Wang, Z. He, *Materials Today Energy* **2016**, *1-2*, 1.
[107] W. Chen, Y. Zhu, Y. Yu, L. Xu, G. Zhang, Z. He, *Chem. Mater.* **2016**, *28*, 4879.
[108] X. Zheng, T. Jiang, L. Bai, X. Chen, Z. Chen, X. Xu, D. Song, X. Xu, B. Li, Y. M. Yang, *RSC advances* **2020**, *10*, 18400.
[109] X. Deng, G. C. Wilkes, A. Z. Chen, N. S. Prasad, M. C. Gupta, J. J. Choi, *The journal of physical chemistry letters* **2017**, *8*, 3206.
[110] A. Guerrero, J. You, C. Aranda, Y. S. Kang, G. Garcia-Belmonte, H. Zhou, J. Bisquert, Y. Yang, *ACS nano* **2016**, *10*, 218.
[111] X. Ma, Y. Mi, F. Zhang, Q. An, M. Zhang, Z. Hu, X. Liu, J. Zhang, W. Tang, *Advanced Energy Materials* **2018**, *8*.
[112] Z. Hu, J. Wang, Z. Wang, W. Gao, Q. An, M. Zhang, X. Ma, J. Wang, J. Miao, C. Yang, F. Zhang, *Nano Energy* **2019**, *55*, 424.
[113] Z. Zhu, V. G. Hadjiev, Y. Rong, R. Guo, B. Cao, Z. Tang, F. Qin, Y. Li, Y. Wang, F. Hao, S. Venkatesan, W. Li, S. Baldelli, A. M. Guloy, H. Fang, Y. Hu, Y. Yao, Z. Wang, J. Bao, *Chem. Mater.* **2016**, *28*, 7385.
[114] B. Philippe, B.-W. Park, R. Lindblad, J. Oscarsson, S. Ahmadi, E. M. J. Johansson, H. Rensmo, *Chem. Mater.* **2015**, *27*, 1720.
[115] D. Alemu, H.-Y. Wei, K.-C. Ho, C.-W. Chu, *Energy Environ. Sci.* **2012**, *5*, 9662.
[116] L. Huang, X. Cheng, J. Yang, L. Zhang, W. Zhou, S. Xiao, L. Tan, L. Chen, Y. Chen, *ACS applied materials & interfaces* **2016**, *8*, 27018.
[117] J. Luo, D. Billep, T. Waechtler, T. Otto, M. Toader, O. Gordan, E. Sheremet, J. Martin, M. Hietschold, D. R. T. Zahn, T. Gessner, *J. Mater. Chem. A* **2013**, *1*, 7576.
[118] J. Y. Oh, M. Shin, J. B. Lee, J.-H. Ahn, H. K. Baik, U. Jeong, *ACS applied materials & interfaces* **2014**, *6*, 6954.
[119] N. Saxena, B. Pretzl, X. Lamprecht, L. Bießmann, D. Yang, N. Li, C. Bilko, S. Bernstorff, P. Müller-Buschbaum, *ACS applied materials & interfaces* **2019**, *11*, 8060.
[120] T. Tevi, S. W. Saint Birch, S. W. Thomas, A. Takshi, *Synthetic Metals* **2014**, *191*, 59.
[121] Y. Zang, L. Chen, J. Zhou, R. Xu, Z. Liu, *Appl. Phys. A* **2021**, *127*.
[122] J. K. Lee, W. L. Ma, C. J. Brabec, J. Yuen, J. S. Moon, J. Y. Kim, K. Lee, G. C. Bazan, A. J. Heeger, *Journal of the American Chemical Society* **2008**, *130*, 3619.
[123] Y. Cui, C. Yang, H. Yao, J. Zhu, Y. Wang, G. Jia, F. Gao, J. Hou, *Advanced materials (Deerfield Beach, Fla.)* **2017**, *29*.
[124] Y. Zheng, T. Goh, P. Fan, W. Shi, J. Yu, A. D. Taylor, *ACS applied materials & interfaces* **2016**, *8*, 15724.
[125] L. Benatto, M. d. J. Bassi, L. C. W. de Menezes, L. S. Roman, M. Koehler, *J. Mater. Chem. C* **2020**, *8*, 8755.
[126] C. Battaglia, S. M. de Nicolás, S. de Wolf, X. Yin, M. Zheng, C. Ballif, A. Javey, *Applied Physics Letters* **2014**, *104*.